DEPARTAMENTO DE FÍSICA ATÓMICA, MOLECULAR Y NUCLEAR

PRODUCCIÓ DE PARTÍCULES A LA FACTORIA DE PIONS DEL GSI DE DARMSTADT

MIGUEL ARDID RAMÍREZ

UNIVERSITAT DE VALENCIA
Servei de Publicacions
2002

Aquesta Tesi Doctoral va ser presentada a Valencia el día 17 de desembre de 2002 davant un tribunal format per:

- Dr. D. Helmut Bokemeyer
- Dr. D. José Lorenzo Ferrero Calabuig
- Dr. D. Juan A. Garzón Heyot
- Dr. D. Reinhard Simon
- Dr. D. Manuel José Vicente Vacas

Va ser dirigida per:
Prof. Dr. D. José Díaz Medina

Depòsit legal:
I.S.B.N.:84-370-5707-8
Edita: Universitat de València
Servei de Publicacions
C/ Artes Gráficas, 13 bajo
46010 València
Spain
Telèfon: 963864115

Producció de partícules a la factoria de pions del GSI de Darmstadt

Departament de Física Atòmica, Molecular i Nuclear
Institut de Física Corpuscular

VNIVERSITAT DE VALÈNCIA
Estudi general

Tesi doctoral presentada per:
Miguel Ardid Ramírez
Setembre de 2002

Particle Production at the GSI-Darmstadt Pion Beam Facility

Departament de Física Atòmica, Molecular i Nuclear
Institut de Física Corpuscular

VNIVERSITAT DE VALÈNCIA
Estudi general

Tesi doctoral presentada per:
Miguel Ardid Ramírez
Setembre de 2002

A Alicia

Als meus pares i germans

Agraïments

Aquest treball no hauria estat possible sense el meu director de tesi, José Díaz, així que m'és necessari agrair-li el seu esforç i consideració. Especialment vull agrair la seua ajuda en els primers moments, on em donà l'oportunitat de participar en aquest projecte i em guià en els primers passos. També és just agrair la resta del grup de València: Mario, Gustavo, Facundo, Yuri i especialment a Nadia per la seva ajuda en l'anàlisi i discussions sobre els resultats.

Faig extensible l'agraïment a la resta de la col·laboració i als diferents grups de persones que hi han participat per dur endavant aquest projecte i alhora ajudar-me en el meu treball tot el que els ha sigut possible. En aquest sentit, major émfasi mereix el Dr. Reinhard Simon, que ha estat supervisant el meu treball durant les meues estades al GSI i amb el qual he estat conversant llàrgament per tal de millorar el meu treball i la tesi en particular. Sense el seu ajut la tesi no hagués estat la mateixa.

També agraisc la Generalitat Valenciana per la concesió de la beca predoctoral que ha possibilitat la meua dedicació a aquest treball durant quatre anys.

Si important ha estat l'ajut que se m'ha donat des del pla professional, podríem dir que vital ha estat l'aportació que se m'ha donat des del pla personal. A Alicia, que tot i haver patit aquesta tesi només els darrers anys, ha tingut temps per donar-me ànims, suport i forces en els moments més durets. Moltes gràcies, carinyet! També vull agrair els meus pares i germans, extensible a tota la familia, per creure en mi i saber que tinc el seu ajut. Especial menció mereix Salva que ha conviscut amb mi durant bona part del desenvolupament de la tesi, donant-me suport moral i també tangible, tirant-me una maneta o fent el sopar si m'he hagut de quedar treballant fins tard.

I com no? Els amics, aquells que han estat amb mi des d'abans de la tesi i altres que he anat coneixent en aquesta última etapa. Alguns de sovint contacte, i que dure per molts anys, i altres que els camins creuats de la vida ens impossibilita una major comfluència. No vull nomenar noms, perque ja ens coneixem i, a més a més, segur em deixava algu. Així que també gràcies als gondia, als col·legues, la penya d'Oliva i segurament a tu també.

Contents

List of Tables

List of Figures

Introducció

La present tesi compila el meu treball realitzat aquests darrers anys al camp de la física nuclear i de partícules experimental, que ha estat desenvolupat principalment endins la col·laboració del feix secundari de pions del GSI de Darmstadt, Alemanya. El feix secundari de pions del GSI és un projecte que té com a finalitat ampliar el camp d'investigació del GSI, ja que permetrà l'estudi de reaccions induïdes per pions. Aquest tipus de feix, juntament amb els feixos anteriors de protons i nuclis pesants, permeten l'estudi de la matèria nuclear a distintes densitats. Així, es pot obtindre una visió més ampla de la física de la interacció nuclear en el rang d'energia del GeV. Aquests feixos junt amb els sistemes de detectors que es troben al GSI fan que aquest laboratori puga ser considerat únic arreu del món. Aquest projecte ha estat finançat per la Unió Europea i compta amb la col·laboració de cinc institucions: GSI-Darmstadt (Alemanya), Universitat de Giessen (Alemanya), GANIL (França), Universitat de Lund (Suècia) i IFIC (Espanya). Aquesta última, a la qual pertany, és un institut mixte de la Universitat de València i el CSIC. La tasca realitzada a l'IFIC endins d'aquest projecte engloba: la construcció dels hodoscopis (en col·laboració amb la Universitat de Lund), simulacions de les línies del feix de pions, participació en els tests i experiments i finalment l'anàlisi de les dades arreplegades en aquests. Si bé la plataforma d'aquest treball és certament el projecte del feix de pions del GSI, aquesta tesi té una visió diferent. Es tracta de presentar un estudi de dos processos importants del feix secundari de pions: l'emissió de partícules en el blanc de producció i el transport de les partícules produides al llarg de la línia. Aquest estudi presenta en detall diferents aspectes del problema: repàs de les dades experimentals i dels models teòrics de les interaccions que intervenen; disseny , construcció i tests dels detectors; tests de les línies de feixos i experiments en elles; simulacions dels diferents processos i anàlisi i parametrització de les dades.

En aquestes últimes dècades les reaccions nuclears en el rang d'energia d'uns pocs GeV han sigut exhaustívament estudiades. S'han desenvolupat mètodes tant experimentals com teòrics. Tanmateix, nous interrogants van emergint, les respostes als quals no han estat encara trobades. Quins són els canals i mecanismes físics d'una certa reacció nuclear? Com quantificar-los? Què passa si considerem un projectil més massiu, o més energètic o un blanc amb major espessor, etc? Com descriure sistemàticament la llarga varietat de reaccions nuclears a les energies d'interés? Quins mecanismes estan darrere de l'emissió de pions? Quin model és més adequat per a la descripció de la producció de pions? Està clar que aquesta tesi no pot contestar totes aquestes interessants qüestions, però farem un xicotet esforç focalitzant-nos en l'aspecte de les reaccions nuclears de protons i nuclis lleugers amb blancs espessos, posant especial atenció a la producció de partícules a angle zero. Al mateix temps, l'aplicació d'aquests estudis per a l'optimització del feix secundari de pions és la nostra major finalitat. S'ha treballat considerablement en aquest camp prèviament. Per exemple, es feren estudis sistemàtics d'aquest tipus de reaccions a LBL [Pap75, Moe83, Bro84]. La nostra principal contribució en aquesta direcció és l'ús de blancs gruixuts i la seua utilitat en feixos secundaris. Hem de recordar que feixos secundaris de pions han estat desenvolupats abans a LAMPF, TRIUMPF, PSI, KEK, Fermilab, BNL, CERN. En aquest respecte el nostre esforç de desenvolupar el feix de pions al GSI té una bona història de precedents. Per altra banda, aquesta és la primera vegada que s'han extret els feixos de pions a partir de col·lisions nucli-nucli a més de les de protó-nucli. Aquest aspecte marca la novetat i fa que la fàbrica de pions del GSI siga única al món i a la història. Tal com s'ha dit anteriorment, una altra raó per considerar-la única és el seu particular ambient. La combinació del feix de pions amb els altres feixos nuclears i els detectors presents al GSI proporcionen un lloc privilegiat per a l'estudi de la interacció nuclear a energies del SIS.

A continuació descrivim breument les diferents parts de la tesi.

Al capítol 1 reflexionem sobre dos aspectes bàsics per al feix secundari de pions del GSI. El primer és l'estudi de la producció de partícules en col·lisions nuclears a energies intermèdies emprant blancs gruixuts. Donat que el feix de pions és generat en aquest tipus de col·lisions nuclears, quan més coneguem d'elles, més podrem millorar la qualitat del feix secundari de pions. El segon aspecte és el programa de recerca del feix secundari desenvolupat. Aquest és la motivació per a la construcció del feix de pions i defineix els requisits per al feix de pions, els quals a la vegada imfluèncien el seu disseny. A la primera part es resumeix el coneixement actual de la producció de partícules en col·lisions nucli-nucli a energies d'uns pocs AGeV, emfatitzant que la producció de pions juga un paper important. Així mateix, exposem les seues principals propietats tenint en compte les distribucions angulars i energètiques. El feix secundari de pions està dissenyat per acceptar pions d'alta energia emessos a angle zero.

Per això també s'examina les seccions eficaces invariants per a la producció de pions en aquesta direcció. El disseny per a acceptància a angle zero és convenient front a dissenys a altres angles ja que les condicions cinemàtiques de la col·lisió nucli-nucli afavoreixen la emissió de pions cap endavant donat que una part considerable de pions poden tindre velocitats pròximes a la velocitat del projectil. Per altra banda, els pions produïts en aquest disseny han de recórrer grans distàncies en el blanc de producció i hi ha una major probabilitat que siguen absorbits. Posteriorment, discutim l'ús de blancs gruixuts als quals l'absorció i la producció de partícules secundàries poden ser significatives. Després, descrivim el possible origen dels electrons d'alta energia que s'observen al feix secundari. La primera part del capítol 1 compila els resultats disponibles en aquest camp amb la finalitat d'aprofitar aquest coneixement per millorar el funcionament del feix secundari. Tractem d'extraure els aspectes principals de l'emissió de partícules que s'han de considerar per entendre la composició del feix secundari, el qual és una mescla de fragments nuclears, protons, pions, electrons i productes de desintegració. La nostra intenció final és construir models que expliquen les dades experimentals i ens ajuden a seleccionar la combinació projectil-blanc més adhient per obtindre no tan sols el major rendiment possible sinó també el feix secundari de pions amb major puresa.

La segona part d'aquest primer capítol està més relacionada amb la motivació, especialment a aquella que ha dut al plantejament i a la construcció del feix secundari de pions. Tal i com ja hem comentat, el principal objectiu d'aquesta factoria de pions és la d'ampliar el programa de física hadrònica del GSI a les reaccions induïdes per pions. En particular, l'interés mostrat per la comunitat científica en dos problemes oberts i on aquesta nova ferramenta podria aportar un poc de llum: l'estructura elemental dels hadrons i l'estudi de les propietats hadròniques endins el medi nuclear, on es tenen coneixements parcials, però més i millors evidències són necessàries. Aquests dos problemes foren el principal motiu per al desenvolupament del feix de pions. De tota manera, aquest feix no va nàixer sols amb la intenció d'encarar aquests dos problemes, sinó amb la idea de donar suport a un més ampli programa físic. Així doncs, aquest feix està obert a noves aplicacions i on grups científics amb diferents i diversos interessos poden demanar ser usuaris per a les seues investigacions. Per exemple, el feix secondari ha sigut requerit per fer espectroscopia gamma dels hipernuclis i també tests a detectors per a altres experiments del GSI.

Al segon capítol descrivim el sistema experimental de la línia del feix de pions del GSI i els seus elements. Primer ens fixem en els blancs de producció.

Aquests són de diferents longituds, entre un i dotze centímetres, i la seua composició és de beril·li, carbonur de bor o titani. Aquesta diversitat de blancs ha estat pensada per desenvolupar un estudi de la producció, així com per optimitzar el feix secundari. Després comentem els elements magnètics de la línia (dipols i quadrupols) que s'encarreguen de transportar les partícules secundàries per la línia des del blanc de producció fins a les sales experimentals. El $B\rho$ màxim de la línia és de 10 Tm, és a dir, es poden transportar partícules amb moment fins a 3 GeV/c si són acceptades per la línia del feix. Per últim en aquest capítol veiem els detectors emprats per a l'estudi, control i cal·libració del feix secundari en les dues línies emprades. En la primera d'elles, la línia HADES, s'utilitzaren tres hodoscopis situats al llarg d'ella. Cada hodoscopi es composa de 10 mòduls de plàstic centellejadors i ens proporciona informació sobre el temps i la posició de les partícules que el travessen. La informació sobre el temps s'utilitza per discriminar les partícules pel mètode del temps de vol; mentre que la informació sobre la posició serveix per determinar el moment amb una incertesa menor del 0.5% utilitzant una correlació entre ambdues magnituds. A més a més, en aquesta línia també es van emprar dos detectors pròxims a la posició del blanc d'HADES. El primer és un gran centellejador que ens informava del nombre total de partícules que aplegaven a aquest punt; mentre que el segon és una xarxa de fibres centellejadores que ens permetia conèixer el perfil del feix a prop del focus.

En quant a la segona línia utilitzada als nostres experiments, la línia C, el seu sistema de detectors fou totalment diferent. No s'emprà cap hodoscopi, en compte d'ells es va utilitzar una sèrie de 5 centellejadors al llarg de la línia que tenien com a missió el diagnòstic del feix i la disciminació de les partícules pel temps de vol. Per aquests experiments la discriminació d'electrons de pions era un objectiu clar i per aquest fi s'emprà la combinació d'un detector de Cherenkov amb un calorímetre electromagnètic de vidre de plom. Finalment, per conèixer el perfil del feix prop del blanc de la línia C s'empraren dues cambres d'ionització i dos detectors de silici.

Al capítol 3 presentem els resultats dels experiments realitzats a les dues línies de pions fins al moment. Primer ens ocupem del test a la línia HADES emprant com a feix primari protons i ^{12}C. En ell, es mesurà l'eficiència dels hodoscopis, la seua resolució temporal i la conseqüent capacitat per discriminar els diferents tipus de partícules. En eixe sentit presentem un estudi de l'empitjorament de la resolució en el temps de vol observat a l'augmentar la intensitat del feix als hodoscopis. També es va investigar la resolució en moment que s'assolix amb el sistema d'hodoscopis. Per últim, però no menys important, ens fixem en la composició i les intensitats del feix secundari en funció del tipus de feix primari, blanc, polaritat i moment central de la línia de feix seleccionat.

A continuació presentem els experiments a la línia C. Aquests complementen els resultats anteriors obtinguts a la línia HADES. A la línia C es fa ús de la combinació del detector de Cherenkov amb el calorímetre electromagnètic per a l'identificació dels electrons. En aquests experiments s'empraren feixos primaris de protons, carboni i nitrògen junt a un gran nombre de blancs que cobrien un ampli rang d'espessors. D'aquesta manera podem fer un estudi exhaustiu de les dependències de la producció de pions i electrons amb el feix primari, el tipus de blanc i el moment central de la línia. Observem també que les intensitats de pions a la línia C són menors a les de la línia HADES degut a una menor acceptància i una major probabilitat de desintegració en vol dels pions. Al mateix temps l'estudi de les intensitat del feix secundari s'enrequeix amb la consideració de les pèrdues d'intensitat degudes als detectors presents a la línia, o siga degudes a la presència de material a la línia del feix.

Al capítol 4 s'incideix en la necessitat de les simulacions per complementar les dades experimentals i aconseguir un major coneixement del processos relevants en la producció i transport del feix secundari de pions. Les simulacions realitzades s'han fet emprant GEANT3 ja que aquest presenta l'avantatge de poder simular els principals processos de l'emissió del feix de pions, a més de descriure tot el procés de producció i absorció de partícules al blanc de producció i també el transport al llarg de la línia de les partícules produïdes. Això és molt convenient en el nostre cas degut a que es treballa en blancs gruixuts i on els efectes secundaris poden ser molt importants. Els primers resultats de simulacions que es presenten són els relatius a la producció de partícules; es proposen dos mètodes per simular la producció de pions en feixos primaris de ^{12}C. Un d'ells consisteix a generar directament els pions al blanc de producció d'acord a una distribució basada en les dades experimentals. L'altre és simular la producció de pions en les col·lisions nucli-nucli de manera teòrica. Desafortunadament, els paquets hadrònics inclosos a GEANT3 no són capaços de simular les col·lisions nucli-nucli. Per tal d'evitar aquesta limitació, hem utilitzat un model de gas calent per al projectil del feix primari per simular els nucleons endins l'ió de ^{12}C que bombardeja el blanc. Això ens porta a la modificació de l'energia i el moment dels nucleons del projectil per tenir en compte que els nucleons no estan lliures i que el projectil és calfat en la col·lisió. Malgrat les limitacions d'aquests mètodes es veu que els resultats d'ambdos mètodes referents als rendiments de pions són similars dins d'un rang acceptable d'exactitud. Després es tracta l'estudi de diversos blancs de producció per tal d'estudiar la producció de pions i electrons utilitzant el feix primari de protons de 4.7 GeV, recentment disponible. Tot açò ens ajudarà en futures eleccions dels blancs òptims per a la producció de feixos secundaris de pions i electrons.

A continuació discutim les simulacions relatives al transport al llarg de la línia de pions. Per això generem pions i observem l'acceptància de les línies HADES i C, la qual està donada per la geometria dels elements magnètics. Tres processos físics són tinguts en compte: la desintegració en vol, el múltiple scattering de les partícules i la interacció hadrònica. Del primer procés podem veure quina és la fracció de muons que apleguen al blanc de la sala experimental i què són confosos amb pions pel sistema de detectors. Les simulacions del múltiple scattering ens diuen que aquest efecte és molt important, especialment per a partícules amb baix moment.

Finalment es mostren els resultats de les simulacions del procés complet, producció i transport, i es comparen amb les dades experimentals. Els resultats que s'observen són dispars. En alguns casos les dades de les simulacions estan molt ajustades a les dades experimentals; però en altres ambdues dades difereixen entre sí, encara que la comparació entre elles és prou raonable. Només en uns pocs casos els resultats de les simulacions pareixen no tindre cap correspondència amb les dades experimentals i viceversa. Malgrat aquestes diferències observades, considerem que aquestes simulacions realiltzades són molt interessants per tenir un altre punt de vista del funcionament de la línia de pions i aplegar a un major coneixement i comprensió d'ella.

El capítol 5 té com a objectiu la comprensió, per mig de models proposats amb un xicotet nombre de paràmetres, de les intensitats de pions i electrons observades. Aquests models tenen en consideració els models teòrics i empírics vistos al capítol 1, les particularitats del sistema experimental i la informació que ens suggereixen les dades experimentals i els resultats de les simulacions. Per a una correcta interpretació de les intensitats mesurades és necessari una correcta parametrització, tant de la producció en blancs gruixuts, com del transport de partícules secundàries al llarg de la línia. En quant a la intensitat de pions, per entendre-la com a una funció del moment, assumirem que els pions es produeixen segons una distribució de Maxwell-Boltzmann en el centre de masses nucleó-nucleó amb una certa temperatura aparent. Per descriure el transport del feix secundari serà necessari considerar la desintegració en vol dels pions i el múltiple scattering de partícules secundàries, el qual quantificarem a partir de les simulacions. Amb aquest procediment s'assolix una bona representació de la intensitat dels pions en funció del moment de la línia i s'extrau la temperatura aparent considerant el millor ajust entre les dades experimentals i els models teòrics. Per tal d'explicar els resultats dels experiments relatius a la intensitat de pions en funció del gruix del blanc de producció, hem desenvolupat un model tenint en compte la producció i absorció de pions en el blanc. Segons aquest model, la variació del nombre de pions al llarg del blanc de producció està correlacionada amb les seccions eficaces dels processos de producció i absorció. Tanmateix, les interaccions secundàries dificulten el tractament directe del problema de la producció i absorció de pions en blancs gruixuts. Tot i això, s'aconsegueixen models amb un xicotet nombre de paràmetres amb un cert sentit físic.

El cas de la producció d'electrons (o positrons) al feix de pions és un procés secundari, la qual cosa comporta una major complexitat per a la descripció dels rendiments d'aquestes partícules. Per resoldre aquest problema assumim que hi ha una clara conexió amb el cas dels pions: el canal de producció d'electrons quantitativament més important és la creació de parells e^+e^- a partir de fotons provinents de $\pi^0 \to \gamma\gamma$. Així, per a la distribució en moment dels electrons també hi emprem una distribució de Maxwell-Boltzmann amb una temperatura aparent que extraiem a partir de les dades. Lògicament, aquesta temperatura és menor que la dels pions perque l'electró final té menor energia que el pió del qual prové. Per últim, considerem la intensitat d'electrons en funcio del gruix del blanc. Ací, s'ha de sumar a la producció de pions dos processos electromagnètics determinants: la creació de parells e^+e^- dels fotons i el bremsstrahlung dels electrons. La combinació d'aquests processos és complicada i no es coneix una solució analítica del problema. Per tant, resolem les equacions d'una manera aproximada. Com la solució aproximada no inclou tots els aspectes involucrats, tractem de corregir-la introduint un factor fenomenològic que s'encarregue de suplir les carències degudes a les aproximacions utilitzades al model.

Finalment s'exposen les conclusions derivades d'aquest treball i es resumeixen els resultats aconseguits. Per últim, també s'avancen breument alguns dels futurs pasos a seguir per al desenvolupament del feix de pions al GSI.

Introduction

This thesis compiles the work I have been doing in the last years in the field of the experimental nuclear and particle physics, which has been mainly carried out within the secondary pion beam collaboration at GSI, Darmstadt, Germany. The secondary pion beam at GSI is a project which aim is to widen the GSI research program allowing the study of pion induced reactions besides the nucleus-nucleus reactions. This pion beam together with the previously available proton and heavy ion beams of SIS will make possible to investigate nuclear matter at different densities. Thus, a deeper insight into the physics of nuclear interactions at the approximately 1 GeV energy range can be achieved. The beams and the existing set of detectors at GSI, make this facility unique world-wide. This project, which has been supported by the European Community, has been developed in the framework of a collaboration comprising 5 institutions: GSI-Darmstadt (Germany), University of Giessen (Germany), GANIL (France), University of Lund (Sweden) and IFIC (Spain). The last institution, where I have been working, is a mixed research institute of the University of Valencia and CSIC. The task that has been carried out at IFIC for this project includes: the construction of the hodoscopes (in collaboration with the University of Lund), simulations of the pion beam-lines, participation in the performed tests and experiments, and finally, the analysis of the produced data. The base for this thesis is the work done within the GSI pion beam project. However, this thesis has a slightly different focus. Its aim is to present a study of the two processes important for the secondary beam: the particle emission in the production target and the transport of the produced particles along the beam-line. This study presents in details different aspects of the problem: the review of the available experimental data and theoretical models for the interactions involved; design, construction and tests of the beam-line detectors; commissionings of the beam-lines; simulations of the different processes and analysis and parameterization of the data.

In the last few decades nuclear reactions in the energy domain of a few units of GeV have been studied exhaustively. Both, experimental and theoretical methods have been developed during these years. However, new questions emerged, the answers to which are still not yet found. Which are the channels and the physical mechanisms of a certain nuclear reaction? How to quantify them? What happens if we consider a heavier projectile, or a more energetic one, or a thicker target, etc? How to describe systematically the large variety of nuclear reactions at the energy of interest? Which mechanisms are behind emission of pions? Which model is more adequate for the description of pion production? It is clear that this thesis is not able to answer all these interesting questions, but we will make a little effort focusing on the subject of proton and light nuclei reactions with thick targets at about AGeV energies, putting special attention on particle production in the very forward direction. At the same time, the application of these studies for optimization of the secondary pion beam represents our main goal. Considerable work has been done in this field previously. For instance, systematic studies of this kind of reactions were done at LBL [Pap75, Moe83, Bro84], as we show in chapter 1. Our contribution in this direction is the performance of thick targets and their utility in secondary beams. It is worth mentioning that secondary pion beams have been developed before at LAMPF, TRIUMPF, PSI, KEK, Fermilab, BNL, CERN. With this respect our effort to develop the pion beam at GSI has a good history of precedents. On the other hand, this is the first time that pion beams were extracted from nucleus-nucleus collisions besides proton-nucleus collisions. This aspect brings the novice and makes the GSI pion beam facility world and history unique. As it has been already mentioned, another reason to consider the GSI secondary pion beam as unique is its particular environment. The combination of the pion beam with other nuclear beams and the existing set of detectors available at GSI provide a privileged place for nuclear physics studies at SIS energies.

Next, we describe briefly the different parts of the thesis.

In chapter 1, we discuss two topics that are of basic importance for the secondary pion beam at GSI. The first one is the study of particle production in nuclear collisions at intermediate energies using thick targets. Since the pion beam is generated in these nuclear collisions, the more we know about them, the more we can improve the quality of the secondary pion beam. The second aspect is the physics research program for the developed secondary beam. This is the motivation for building the pion beam and it defines some requirements for the pion beam that influence its design. In the first part, present status of particle production in nucleus-nucleus collisions of a few AGeV is summarized. Here, we emphasize that pion production plays an important role and discuss its main properties looking at the pion angular and energetic distributions. The secondary pion beam is designed to accept the fast pions emitted in forward direction. That is why we examine the invariant cross-section for the production of pions in the very forward direction. The design for acceptance in forward direction in comparison with designs for acceptance in other directions is convenient for taking advantage of the kinematical conditions of pion production in nucleus-nucleus collisions, since a considerable fraction of pions can have velocities close to the velocity of the projectile. On the other hand, the produced pions in this design have to travel a long distance in the production target and there is a large probability of pion absorption. Afterwards, we discuss about the usage of thick targets in which the absorption and the secondary particle production processes can be very important. Next, we describe the possible sources for the high energy electrons observed in the secondary beam. The first part of chapter 1 compiles the available results in this field in order to take advantage of the previously accumulated knowledge to improve the performance of the secondary beam facility. We try to extract the main aspects of particle emission that have to be taken into account to understand the composition of the secondary beam, which is a mixture of nuclear fragments, protons, pions, electrons and products of decay in flight. Our final intention is to build models which can explain experimental data and help us to decide which projectile and target combination not only leads to the highest yields but also to the purest secondary pion beam.

In the second part of chapter 1 the reasons to construct the secondary pion beam facility at GSI are explained. As we have already mentioned, the main goal of this facility is to widen the hadronic physics program at GSI with pion induced reactions. Particularly, this facility could provide new data in two open questions of the elementary structure of hadrons and of the possible change of hadronic properties inside nuclear matter. These two important subjects were the main reasons for the building of the pion beam, although the idea of giving support for a wider physics program was kept always in mind. Therefore, the secondary beam is open to new applications. For instance, it has already been proposed to use it for a study of γ-spectroscopy of hyper-nuclei and for testing detectors for some other experiments at GSI.

In chapter 2, we describe the experimental setup of the pion beam-lines at GSI and their related elements. First, we look at the production targets. Their lengths are between 1 and 12 cm and they are composed of beryllium, carbon boride or titanium. This collection of targets has been chosen to study the production of pions and to optimize the secondary beam. Next, the magnetic elements of the beam-line (dipoles and quadrupoles) are considered. They allow to transport secondary particles along the beam-line from the production target to the caves, where the experiments take place. The maximum $B\rho$ of the beam-line is 10 Tm, i. e., particles with momentum up to 3 GeV/c can be transported if they are accepted by the beam-line. The last part of this chapter is related to the detectors that have been used to study, monitor and calibrate the two pion beam-lines where the experiments were performed. In the first one, the HADES beam-line, three hodoscopes along the beam-line were used. Each hodoscope is composed of 10 plastic scintillator modules and gives us time and position information of the particles that are going through it. The time information is used to discriminate the particles by the time of flight method. The position information is used to measure the momentum with a resolution better than 0.5% using a correlation between both magnitudes. Besides, two more detectors were used close to the HADES target position. The first one was a big plastic scintillator which scaled the total number of particles reaching this point. The second detector was a scintillating fiber array which estimated the beam profile near the focus point.

The second beam-line used in our experiments, the C beam-line, was comprised of a completely different system of detectors. No hodoscopes were used here. Instead, a collection of 5 plastic scintillators along the beam-line was used. These detectors monitored the beam and discriminated the particles by the time of flight method. For these experiments the electron discrimination was needed and it was done by a combination of a Cherenkov detector and a lead-glass calorimeter. Finally, two ionization chambers and two silicon detectors were used to obtain the beam profile near the cave C target.

In chapter 3, we describe the results of the experiments performed with the aforementioned two beam-lines. First, the results of the HADES beam-line commissioning with proton and carbon primary beams are discussed. The efficiency, time of flight resolution of the hodoscopes and the subsequent ability to discriminate the different kind of particles are presented. Here, a study of the worsening of the time of flight resolution observed with increasing beam intensity in the hodoscopes is also presented. Next, the momentum resolution given by the system of hodoscopes is investigated. Last, but not least, the composition and intensities of the secondary beam as a function of primary beam, target, polarity and central momentum are shown.

Afterwards, the experiments in the C beam-line are discussed. The results from these experiments complement the previous ones from the HADES beam-line experiments. Here, we describe the use of the combination of the Cherenkov detector plus lead-glass calorimeter for electron identification. In these experiments primary beams of protons, carbon and nitrogen were used together with a large collection of targets, which cover a wide region of target thicknesses. This allowed us to do an exhaustive study of the dependences of pion and electron production with the primary beam, target type and central momentum of the beam-line. We observe that the C beam-line intensities are lower than the HADES ones due to a smaller acceptance and a higher probability for pions to decay in flight. The study of intensities of the secondary beam is completed with the consideration of beam attenuation due to the beam tracking detectors, i. e., due to the presence of material in the beam-line.

In chapter 4 we emphasize the need of simulations to complement the experimental results and reach a better knowledge of the relevant processes of the secondary beam production and transport. The simulations have been done with GEANT3 because it has the advantage of not only simulating the main processes of the pion beam emission but also of describing the full process of particle production and absorption in the production target and the transport of the produced particles along the beam-line. This is very convenient for us because we are working with thick targets and secondary effects can be of great importance. The first results of simulations described are related to particle production. Two methods are proposed to simulate the production of pions in ^{12}C primary beams. The first one is to generate pions directly in the production target following a distribution based on experimental results. The second method is to simulate pion production in the nucleus-nucleus collisions theoretically. Unfortunately, the hadronic packages included in GEANT3 are not able to simulate nucleus-nucleus collisions. In order to avoid this limitation, we have used a hot hadron gas model of the primary beam projectile to simulate the nucleons inside the ^{12}C ion bombarding the target. This leads to a modification of the energy and momentum of the nucleons of the projectile that takes into account that they are not free nucleons and the projectile is heated in the collision. Despite the limitations of these methods, we see that results from both methods in regard to the pion yields are similar within an acceptable accuracy. Next, the investigation of several production targets is done in order to study the pion and electron production using the recently available 4.7 GeV proton primary beam. This will help us in future choice of optimized targets for pion and electron secondary beam production.

Afterwards, we discuss in detail the computer simulations of the transport along the beam-line. In order to do this, we generate the pions and study the acceptance of HADES and C beam-lines, which is given by the geometry of the magnetic elements of the beam-lines. Three physical processes are taken into account: decay in flight, multiple scattering and hadronic interaction. From the first process we can extract the muons that reach the caves which cannot be discriminated from pions by the experimental setup. The simulations of multiple scattering show that this effect is very important, especially for particles with low momentum.

Finally, the results of computer simulations of the full process, production and transport of pions and electrons, are confronted to the experimental data. In some cases the experimental data and simulated values are in agreement, but in some others they differ, although they compare reasonably well. Only in a very few cases, simulated values do not seem to describe at all the experimental data. In spite of these rare discrepancies, we consider the performed computer simulations to be very important for a better understanding of the secondary beam properties.

In chapter 5 we try to understand the pion and electron intensities measured in the experiments within the frames of some models having a small number of parameters. These models take into account the theoretical and empirical models mentioned in chapter 1, the peculiarities of our particular setup and the information obtained from both the experiments and simulations. To obtain a good interpretation of the measured intensities it is necessary to have a right parameterization of the production process in thick targets and of the transport of secondary particles along the beam-line. To understand the pion intensity as a function of the momentum, we assume that the pions are produced according to a Maxwell-Boltzmann distribution in the nucleon-nucleon center of mass with an apparent temperature. To describe the transport of the secondary beam, we need to consider the pion decay in flight and the multiple scattering of secondaries. The last effect is estimated from simulation results. With this procedure, a good description of the pion intensity versus the momentum of the beam-line can be achieved and the apparent temperature can be extracted from the best fit of the theoretical models to the experimental data. To explain the experimental data on pion intensity dependence on target thickness, we develop a model which considers the production and absorption processes. Although secondary interactions make it difficult to treat the problem of pion production and absorption in thick targets, it is possible to develop models with a small number of parameters with some physical meanings.

Production of electrons (or positrons) in the pion beam is a second order process and this brings additional complexity for the prescriptions of the yields of these particles. To solve this problem we assume that a clear connection with the pion case exists: the main channel of electron production is the e^+e^- pair creation from photons coming from $\pi^0 \to \gamma\gamma$. Therefore, we also use a Maxwell-Boltzmann distribution with an apparent temperature for the momentum distribution of electrons. This temperature will be smaller than that of the parent pions because final electrons have a smaller energy than the pions from which they originated. Last, we look at the dependence of secondary electron intensity with the target thickness. Here, in addition to the pion production, we need to consider two essential electromagnetic effects: the e^+e^- conversion of photons and the electron bremsstrahlung. The combination of these processes is very complex and no analytical solution is known. Therefore, we make some approximations in order to solve the equations. Since the approximated solution does not contain all the involved aspects, we try to correct it with the introduction of a phenomenological factor which takes care of the approximations introduced.

Finally, we make some conclusions and summarize the results accomplished in this work. Future steps for further development of the pion beam facility at GSI are, finally, briefly put forward.

Chapter 1

Theory and motivation

There are two aspects that motivate our work at the pion beam at GSI. The first one is related to the study of particle production in proton-nucleus and nucleus-nucleus collisions at intermediate energies with thick targets. In fact, secondary beams may be considered as a direct application of this kind of studies. The second aspect is connected with the physics that is going to be studied with the secondary beams. The opportunity to extend the current heavy ion program at GSI by pion induced elementary reactions was the essential motivation for realizing this facility.

1.1 Particle production in nuclear collisions

Relativistic nucleus-nucleus collisions provide a unique possibility to study nuclear matter at different densities and energies. In particular, the study of meson production in these collisions has provided important insight into the dynamics of such reactions, and consequently into the formation and the properties of compressed and heated hadronic matter. At incident energies of a few AGeV, the excitation of nucleons into baryon resonances which subsequently decay by the emission of mesons is a crucial reaction channel for pion production. As shown in Fig 1.1, the ratio of pions to participant nucleons in a heavy ion reaction is about 10-20% at beam energies of 1-2 AGeV, while at higher energies of 5-10 AGeV, it reaches a value of 70-100%. Systematic studies of meson production have been performed at GANIL, LBL, GSI, Dubna and BNL [Sto86, Sen99].

In this section we will review pion production and the mechanisms which are supposed to be associated. We devote special attention to the production in forward direction with light nuclei and we address the complexity of pion

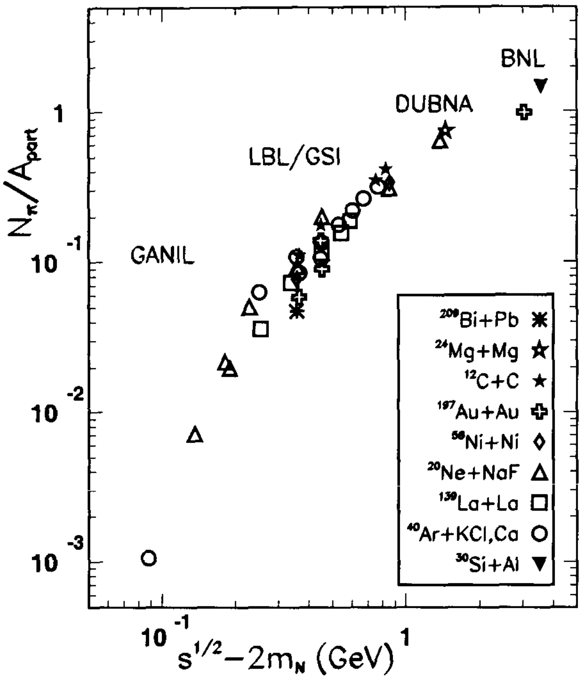

Figure 1.1: Compilation of the pion multiplicity per participating nucleon in symmetric systems as a function of the kinetic energy of two colliding nucleons in the center-of-mass frame. The data are taken from [Mar98, Mar99, Sch94b, Wol98, Sul82, Lau00, Gaz95, Mün95, Mün97, Nag81, Har85, Har87, Ave97].

production using thick targets. Both features play a major role in the production of the pion beams at GSI. In addition, we study the origin of the high energetic secondary electrons (and positrons) associated with the pion yield, which have practical applications for detector studies.

1.1.1 Production of pions

A more general study of the subject is found in [Sto86] and in [Sen99]. In our discussion of pion production we will focus on those aspects that are most direct related to our work.

The threshold energy for pion production in a nucleon-nucleon collision is

$$E_{th} = 2m_\pi \left(1 + \frac{m_\pi}{4m_N}\right). \tag{1.1}$$

However, pions have been observed at energies as low as 25 AMeV [Yah02, Sch97, Bra84], i.e., far below the domain where individual nucleon pair relative energies could suffice, even by help of Fermi motion. We need cooperative modes of several participating nucleons to satisfy energy and momentum conservation.

At energies of a few AGeV, systematic charged-pion production experiments have established the picture that pions are produced mainly in binary nucleon-nucleon collisions via the excitation and the subsequent decay of $\Delta(1232)$ resonances. It is used to think that pion production is basically a 2-nucleon process, based in the assumptions of the cascade model. The effects of the nuclear medium was supposed to merely govern corrections like absorption, off-shell shifts of available NN collision energy, collective flow energies, etc. Afterwards, it was shown that this view is only suitable for peripheral collisions or in reactions of light nuclei, due to the fact that pions interact strongly with nuclear matter, mainly described by the reaction cycle $NN \leftrightarrow N\Delta \leftrightarrow NN\pi$. Therefore, they are expected to leave the reaction zone predominantly in a late stage of the collision, when the system has expanded and cooled down. Taking this pion re-scattering into account, one should expect that the inclusive production cross sections and the particle spectra show a dependence on the mass of the colliding nuclei. For instance, the mean number of pions emitted per participating nucleon tends to drop with the mass of the system. On the other hand, we should not forget other mechanisms that also have its influence, like higher resonances or just non-resonant pion production. In high density fireballs, created in central collisions of heavy nuclei, thermal and chemical equilibrium properties are approached through the sequence of binary collisions such that a new state of nuclear matter results. The pion and delta abundance, and thus the finally observed pion yield, is controlled by locally defined multi-nucleon properties like density, temperature and chemical potential.

Up to now the complex shape of pion spectra and specially their change with incident energy and mass of the colliding nuclei is not fully understood. However, systematic studies have provided an important knowledge of these aspects as we will see below.

1.1.2 Pion spectra

Here we will look at the distributions of pions produced as a function of the angle of emission and the momentum.

The left part of Fig. 1.2 shows the angular distribution for pions in a central and an unbiased selection of Ar + KCl events at 1.8 AGeV [Bro84]. We observe that the latter kind of events exhibits a higher degree of anisotropy. Paremeterizing, we have

$$\frac{d\sigma}{d(cos\theta)} \propto (1 + acos^2\theta), \tag{1.2}$$

where a is known as the asymmetry parameter. The ratio R of the non-isotropic fraction to the total is given by $R = \frac{a}{3+a}$ and results in R(central)=0.15 and R(unbiased)=0.28. On the other hand $R \geq 0.5$ for the direct reaction $NN \rightarrow NN\pi$ at similar energies. Therefore, the anisotropy is smaller for nucleus-nucleus collisions, specially for the central ones.

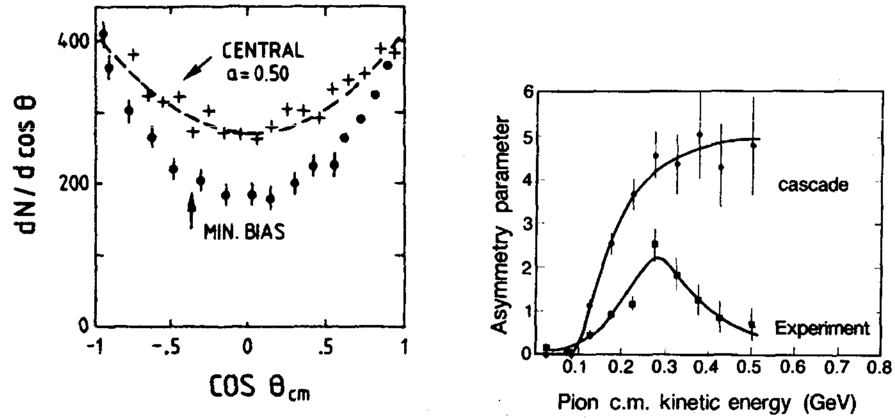

Figure 1.2: Anisotropy of π^- emission in Ar + KCl at 1.8 AGeV. Left: Angular distributions for central and minimum bias data samples fitted by Eq. 1.2. Right: The asymmetry parameter a plotted as a function of pion center of mass kinetic energy, for the data and for the cascade model calculation. The figures are from [Sto86, Bro84].

The right part of Fig. 1.2 shows the dependence of the a parameter on pion center of mass energy for the central events. It starts out at a=0 because the phase space volume sampled for $E_{kin} \rightarrow 0$ reduces to a point which cannot exhibit any anisotropy. We observe a broad peak, a>1, for $200 \leq E_\pi \leq 360$ MeV, with $R \approx 0.5$ at the maximum which is indicative of direct $NN \rightarrow NN\pi$ kinematics. The pion cross section as a function of energy is down to below 20% of its peak value in this interval, i. e., a small fraction of the yield, with $E_\pi^{kin} \approx 2\langle E_\pi^{kin} \rangle$ produces most of the anisotropy. This has also been observed at the lower energy 0.8 AGeV, but then the maximum occurs at a lower energy $E_\pi \approx 150$ MeV.

Theoretical studies in coherent pion production like [Fer94] presents also this kind of asymmetry, which agrees in the idea that direct, i. e., non-thermalized $NN \to NN\Delta \to NN\pi$ reaction is the responsible for this effect. These processes should occur in the surface portions of a nucleus-nucleus reaction where the summed nuclear densities of target and projectile are below ρ_0, the mean free path λ becoming comparable to the total length of transversal. In going from peripheral to central collisions, the fraction of nucleons, undergoing a single scattering, drops down. However, it cannot drop to zero even in an ideal head-on reaction because of the dilute "corona" interaction region forming along the equator perpendicular to the beam axis. In an equal mass collision, the number of the nucleons falling into this region increases like $2A^{\alpha}$ with $1/3 < \alpha < 2/3$. Thus, the fraction of the total $2A$ nucleons likely to undergo only one collision decreases like $2A^{\alpha-1}$.

Another feature of the right part of Fig. 1.2 is that the cross section is more isotropic again for the small fraction of the total yield at $E_{\pi}^{kin} > 2\langle E_{\pi}^{kin}\rangle$. The fireball seems to produce a tail of fast pions, ranging beyond the relatively well localized regions of momentum space where the direct reaction products are concentrated.

For the energy distribution, the invariant cross section is usually expressed in terms of a Maxwell-Boltzmann (M-B) distribution:

$$E\frac{d^3\sigma}{dp^3} = E\frac{d^2\sigma}{p^2 dp d\Omega} = \frac{d^2\sigma}{p dE d\Omega} \propto E \exp\left(-\frac{E}{T}\right), \tag{1.3}$$

where E is the total c.m. energy. This is done in an attempt to extract the temperature T at the point of freeze-out. Nevertheless, R. Stock described [Sto86] that there are some aspects in the pion production that could deviate from a M-B distribution and lose partly this interpretation.

In the left part of Fig. 1.3 the pion energy spectrum at 90° in the c.m. system is shown with a M-B distribution fit using Eq. 1.3 that results in a T_{π} = 69 MeV.

The right part of Fig. 1.3 shows the temperature parameters obtained from a fit of Eq. 1.3 to the invariant cross section at various c.m. angles for the reaction Ar + KCl at 1.8 AGeV. The two curves correspond to the results for an unbiased data sample and for a central trigger sample where a multiplicity of 6 or more negative pions was selected. The former curve falls off steeply while the second decrease more smoothly. We can see again the effect of direct "corona" production of Δ's where the Δ escapes without further re-scattering and subsequently decays into $N\pi$ and, thus, enhancing the forward/backward yield of pions.

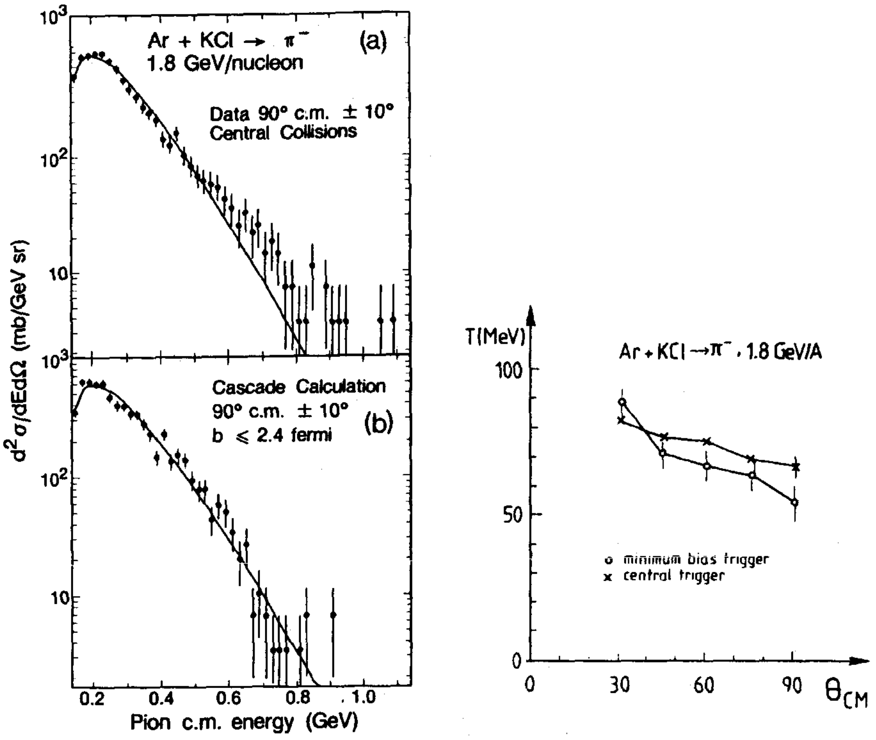

Figure 1.3: Left: (a) Pion energy spectrum at 90^0 in the c.m. system together with a Maxwell-Boltzmann fit using Eq. 1.3 with $T_\pi = 69$ MeV. (b) Calculated pion energy spectrum at same conditions for the Intra-nuclear Cascade model together with a fit with $T_\pi = 73$ MeV. The figure is from [Bro84]. Right: Dependence of the apparent temperature on the c.m. angle for central and minimum bias selection data from the pion production in Ar + KCl at 1.8 AGeV.

It was observed that pion spectra slightly deviate from a single M-B distribution and have been parametrized by a superposition of 2 M-B distributions:

$$d^3\sigma/dp^3 = C_1 exp(-E/T_1) + C_2 exp(-E/T_2). \tag{1.4}$$

Table 1.1 presents a compilation of the inverse slope parameters obtained from fits to the measured spectra of Eq. 1.4 or Eq. 1.3. The values of the inverse slope parameters T_1 and T_2 are correlated and depend on the measured momentum range. Nevertheless, the fit results have some features in common: T_1 has values between 40 and 50 MeV for most of the systems and T_2 increases with both the mass number of the colliding nuclei and the bombarding energy. Any interpretation of the slope parameters in Table 1.1 should take into ac-

A+A	E_{beam} [AGeV]	π	T_1 [MeV]	T_2 [MeV]	Ref.
Au+Au	1.0	π^+	45±3	76±3	[Mün97]
	1.0	π^+	49±2	85±3	[Wag98]
	1.0	π^+	49±4	96±10	[Pel97]
	1.0	π^-	41±3	76±3	[Wag98]
	1.0	π^-	42±3	96±10	[Pel97]
	1.0	π^o	38±4	78±4	[Sch94b]
	1.0	π^o	50±4	86±7	[Ven94]
Ni+Ni	0.8	π^+	40±3	68±3	[Mün97]
	1.0	π^+	45±3	75±3	[Mün97]
	1.0	π^+	47±3	77±3	[Wag96]
	1.06	π^+	49.4±3.7	96.4±5.1	[Pel97b]
	1.06	π^-	42.2±2.7	96.4±5.1	[Pel97b]
	1.45	π^+	54.3±3.3	103.8±4.9	[Pel97b]
	1.8	π^+	50±3	95±3	[Mün97]
	1.8	π^+	36±3	90±3	[Wag96]
	1.8	π^-	40±3	91±3	[Wag96]
	1.93	π^+	56.6±4.4	111.7±9.5	[Pel97b]
Ar+Ca	0.8	π^+, π^-	59±6	-	[Mar98]
	1.0	π^o	65±1	-	[Ven94]
Ar+KCl	1.8	π^-	59	102	[Bro84]
Ne+NaF	1.0	π^+	43±3	63±3	[Mün97]
C+C	0.8	π^o	50±4	-	[Ave97]
	1.0	π^o	54±3	-	[Ave97]
	1.0	π^+, π^-	45±3	62±3	[Foe98]
	1.0	π^-	57±5	-	[Lau00]
	1.0	π^+, π^-	76±5	-	[Lau00]
	2.0	π^o	83±2	-	[Ave97]
	2.0	π^+, π^-	40±3	86±3	[Foe98]

Table 1.1: Pion inverse slope parameters at SIS energies for symmetric systems from a fit of Eq. 1.4 or Eq. 1.3 to the spectra.

count the correlations between the different fit parameters. What would be needed in addition to the values presented in Table 1.1 are the cross correlations between the two slope factors and relative yields of the two components. For a more accurate interpretation, we would also need the angular range of the experiments and the sort of selected events.

The enhancement at low pion momenta (described by the T_1 component) was explained by the contribution of pions from delta resonance decay [Bro84]. In this case the pion transverse momentum is strongly influenced by the Q-value of the decay and does not reflect the "temperature" of the nuclear fireball. This interpretation of the pion spectra was motivated by the fact that the pion production cross section in proton-proton collisions up to about 2 GeV bombarding energy is dominated by the Δ resonance [Ver82, Hub94].

It is still under debate, whether the high-energy component of the pion spectra also reflects resonance decay kinematics or represents the thermal pions. In any case, it has a rather strong dependence on the energy and the mass of the reaction.

1.1.3 Production of pions in forward direction

In this section we focus on the results in experiments of pion production in forward direction at intermediate energies. The experiments, which are described in [Moe83, Pap75], were performed at LBL BEVALAC. They measured the inclusive pion production at forward angles using projectiles from proton to carbon at 1.05 and 2.1 AGeV (for proton up to 4.8 GeV) using several targets (H, Be, C, Cu, Pb). They did a systematic measurement of the invariant cross-section $E\frac{d^2\sigma}{p^2dpd\Omega}$, which Fig. 1.4 is an example, and tried to explain its shape using several scaling variables. One of them was a usual exponential fit to the energy distribution with the results shown in Table 1.2. They also measured the dependence of the pion production cross-section on target mass by fitting the data to the form $E\frac{d^2\sigma}{p^2dpd\Omega} \propto A_T^n$, where A_T is the nucleon number of the target. For 2.1 AGeV alpha projectiles, they observed that $n \approx 0.4$, indicating that collisions leading to the production of pions have an A_T dependence typical of peripheral processes. This exponent is independent of projectile, projectile energy, production angle, or pion momentum except for the lowest pion momenta observed, which corresponds to approximately 90 MeV kinetic energy in c.m., where a slightly higher value of n is found (suggesting less peripheral collisions). This fact was first interpreted in this way: the lower momentum pions were produced in central collisions and the higher in peripheral collisions. However, as we have seen in the previous section, this aspect is not clear and there are evidences of fast pions from central collisions. In any case, it seems clear that they observed an enhancement of low momentum pions, although there is not yet a complete agreement about the explanation of the spectra. Concerning to the dependence on projectile mass, they parametrized the data from the alpha and carbon projectiles as $E\frac{d^2\sigma}{p^2dpd\Omega} \propto A_B^m$, where A_B is the projectile mass number. They observed that the exponent m was greater than 1 (between 1.2 and 1.7) for all the pion energies. This fact suggests that processes involving more than two nucleons contribute to the production of pions.

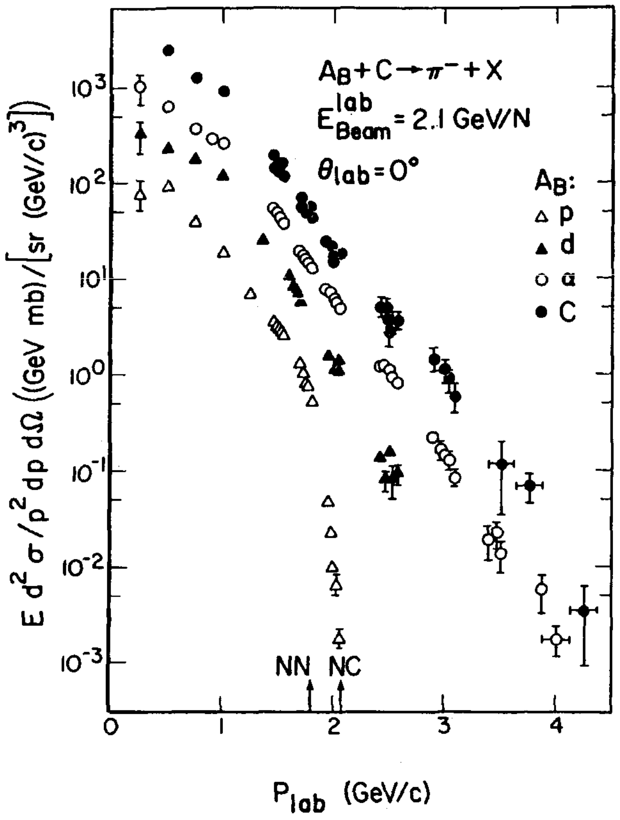

Figure 1.4: Lorentz invariant π^- inclusive cross section versus the laboratory momentum at 0° for 2.1 AGeV protons(△), deuterons(▲), alphas(○), and carbon nuclei(●) interacting with a carbon target. The arrows indicate the kinematic limits for pion production from free nucleons as well as from nucleon-nucleus interaction. The figure is from [Moe83].

The negative pion production in the 1-2 AGeV region at forward angles has also been studied at GSI [Sch94]. Here, heavier projectiles were used: ^{20}Ne

Projectile	E_{beam} [AGeV]	T [MeV]
d	1.05	47±3
	2.1	85±2
α	1.05	63±1
	2.1	103±1
C	1.05	68±2
	2.1	111±2

Table 1.2: Slope parameters T from the fits $Ed^3\sigma/dp^3 \propto exp(-E/T)$ using carbon targets. The data are from [Moe83].

and ^{58}Ni. They measured the invariant cross-section $E\frac{d^2\sigma}{p^2dpd\Omega}$ for pions (and kaons and antiprotons). For pions, they obtained a slope parameter T from the fit $Ed^3\sigma/dp^3 \propto exp(-E/T)$ of 82±4 MeV in $^{20}Ne + NaF$ reactions and 117±5 MeV in $^{58}Ni + Ni$ reactions, both at around 1.9 AGeV.

1.1.4 Theoretical models for the pion production

There is a large number of theoretical models that study relativistic heavy ion collisions. A more detailed discussion and comparison between different models is described in [Ven94]. Anyhow, all of the models can be roughly divided into two classes:

1. Statistical macroscopic models like those based on fluid dynamics [Mis91, Mar91]. They suppose the existence of local equilibrium in stage of the reaction, which is not always valid. However, they have the advantage of their transparency to the relevant physics and of working with macroscopic concepts like Equation Of State (EOS), particle flow, thermalization, freeze-out, entropy, chemical equilibrium, etc.

2. Microscopic dynamical models. They have the advantage of not requiring local thermal and chemical equilibrium. They study the dynamical evolution of the nuclei in the collision. In principle, correlations are preserved among scattered hadrons in the underlying theory. However, the numerical implementation removes these correlation at least partly. Typical examples of these models are the Intra-Nuclear Cascade (INC) [Gud92],

Quantum Molecular Dynamics (QMD) [Sor89] and Boltzmann-Uehling-Uhlenbeck / Vlasov-Uehling-Uhlenbeck (BUU/VUU) [Cas90, Bao91] models. According to these models, the direct pion production ($N + N \to N + N + \pi$) is negligible compared to the indirect production through resonances ($R \rightleftharpoons N + \pi$) in the 1 AGeV energy domain. For these energies, the pion production and scattering is governed by the $\Delta(1232)$-resonance. All the same, other higher resonances like $N^*(1440)$, $N^*(1535)$ and even higher also play a role. These have been included in recent versions of the models like the Coupled-Channel-BUU (CBUU) [Tei97], where more channels and interactions have been implemented, being able to explain some effects that they were not before. For example, the Boltzmann shape of the pion energy spectrum was reproduced with previous cascade models as it is shown in left part of Fig. 1.3, but they were not able to explain the angular dependence of the factor of asymmetry a (see right part of Fig. 1.2). Comparison with Fig. 1.5 shows clearly that that there is now a better understanding [Tci97].

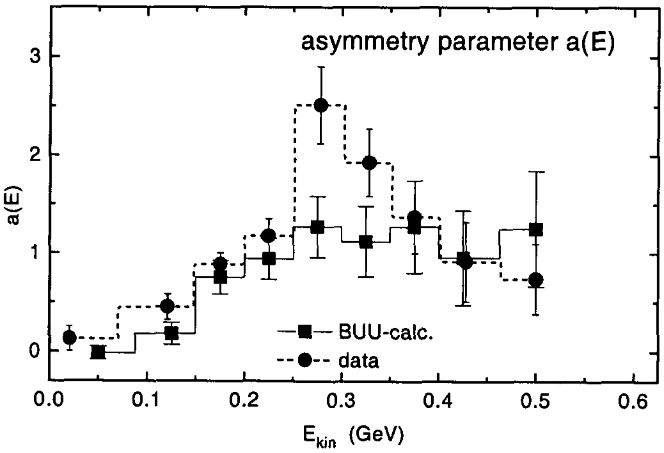

Figure 1.5: The asymmetry parameter a (see section 1.1.2) as a function of the pion kinetic energy for the central event class. The circles represent the data and the squares indicate the results obtained by fitting the CBUU-results in the regime $0 \leq cos\theta \leq 0.9$ by $const(1 + a(E)cos^2\theta)$ for fixed pion kinetic energy. The figure is from [Tei97].

1.1.5 The problem of thick targets

In principle, if we knew exactly the mechanism of pion production in nucleus-nucleus collisions, we would know the most relevant information needed for the study of pion production in a thick target. But still, we would need to take into account many effects in order to have a complete understanding of the whole process: pion absorption, nuclear fragmentation, pion production by secondary nuclear fragments, energy loss and multiple scattering. Pion production by secondary fragments can be very important, specially when we are working with thick targets as it is our case. To face this kind of complex problems, one can try to measure a given effect in the cleanest way and make a model of the process as exact as possible. Often, combination of different available models is needed to obtain reliable conclusions. Then, we should combine the different models for the different processes involved. This is certainly an almost endless task. Fortunately, not all the effects have the same importance and need the same accuracy. Moreover, some of the work is partly already done. For example, some pion production and absorption cross-section measurements have been done [Moe83, Clo74] and there are already good and checked models for some processes like the energy loss.

Finally, we would like to remark that simulation is the easiest way to combine all the models, and sometimes the only one that is realistic for such a complex problem. Nevertheless, some good approximations are sometimes possible analytically.

1.1.6 The high energetic electron (and positron) production

High energetic electrons (and positrons) have been observed in the secondary pion beam. There is a lively discussion about where they are coming from. If we look at the possible channels, we first should consider that we use thick targets and therefore there are also indirect processes. With this situation, we think that there are three processes which could play an important role here:

1. e^+e^- gamma ray conversion following the channel $\pi^0 \to \gamma\gamma$ (with a branching ratio of 98.8%)

2. Dalitz decay of neutral pions, $\pi^0 \to \gamma e^+e^-$ (with a branching ratio of 1.2%)

3. e^+e^- pair conversion of gamma rays originated in $\Delta \to N\gamma$ (with a branching ratio of 0.5%)

The total cross-section for e^+e^- pair production by photons is expressed in a parametric equation with good accuracy in [Bru94]. It has a value that goes from 650 mb for 0.5 GeV photons to 711 mb for 3 GeV photons in beryllium. Thus, this is an important effect in our case. For example, for a 10 cm length beryllium target and supposing a 1 GeV photon traveling half this length, the probability of pair production is 34 %. So, photons are an important source of electrons.

Considering at the branching ratio of electron conversion, it seems that the first channel is the quantitatively most important. However, we think that the rest of the channels are also important because they produce higher energetic electrons in the final state and therefore, these channels may play an important role in the production of high energy electrons.

1.2 Motivation of the pion beam facility

The pion beam facility has been built in an attempt to broaden the physics program that is being pursued at GSI. A comprehensive source of the physics motivation of the pion beam facility can be found in its proposal [Met95].

Due to secondary particle production the dynamics of heavy-ion collisions at relativistic ($E_{kin}/A \approx m_N$) and higher energies is governed by cascades of elementary hadron induced reaction. A detailed knowledge of these elementary reactions, not available with sufficient accuracy in many cases, is thus an essential prerequisite for a quantitative description of relativistic heavy-ion collisions. As pions are the most abundantly produced particles, pion induced reactions play a particularly important role in this context. Corresponding data in the relevant momentum range can be obtained in experiments using secondary pion beams from the GSI facility.

Furthermore, many aspects of hadron structure are either only poorly known or even completely unknown although they are essential for understanding the low-energy, non-perturbative regime of Quantum Chromodynamics (QCD). Again, corresponding data, in particular on baryon and meson form factors will be obtainable with the pion beam. The facility at the heavy ion synchrotron SIS can broaden the research program at GSI by including those aspects of hadron physics which provide links between nuclear and particle physics.

The combination of the pion beam with the detector systems currently available at GSI will make this facility unique world wide. This facility will use the dilepton spectrometer HADES [Sch96], the 4π charged particle detector system FOPI [Gob93], the magnetic spectrometer KaoS [Sen93], the large area neutron detector LAND [Bla92] and the photon spectrometer TAPS [Nov91].

In the next sections we will describe briefly the different research directions of the pion physics program. In particular, the studies about elementary structure of hadrons, hadron properties in the nuclear medium and, finally, about other applications of the pion beam like its use for hyper-nuclei studies or for testing detectors.

We would also like to say that the pion beam is certainly not limited to these ideas. They represent the current thinking and serve as a starting point for a broader and richer research program. Moreover, there are meetings, like the "X HADES Collaboration Meeting" [Had01] or the "Hadronic Physics with HADES" [Had00], where people propose and discuss experiments. An important part of these experiments are related to the pion beam facility. Furthermore, the pion beam facility is not only opened for discussion but also to new users and new physics program. In fact, as we will see, several groups of scientists have already shown an interest in this facility and are planning experiments.

1.2.1 Elementary Structure of Hadrons

The structure of hadrons is an important testing ground for the non-perturbative regime of QCD. The distribution of charge and magnetism in hadrons is described by form factors. While space-like form factors have been studied, e.g. in electron scattering, electromagnetic form factors in the time-like regime are either poorly or only partially known at present. They can be measured, however, by the observation of dilepton emission or Dalitz decays of baryon resonances or neutral mesons. All relevant baryon resonances with masses below 2 GeV/c^2 as well as pseudo-scalar and vector mesons can be produced with pion reactions in the momentum range of this facility.

Transition form factors involving nucleon and baryon resonances can be measured at SIS in exclusive reactions, e.g. $\pi^- p \to n e^+ e^-$ whereby the e^+e^- pair is detected with the HADES spectrometer and the neutron with the LAND detector. Fig. 1.6 shows the present knowledge of the time-like form-factor of the proton derived from $p\bar{p}$ annihilation in comparison to fits with the ten-resonance unitary and analytic model [Dub00], which is an improvement of the vector meson dominance model (VMD). Exploiting off-shell effects the above pion induced reaction will provide access to the "unphysical" regime below the $2m_N$ threshold and thereby allow an experimental test of the VMD calculations that predict pronounced structures in the form-factor near known vector meson masses.

Transition form factors of neutral mesons (η,$\eta\prime$,ω) become accessible exper-

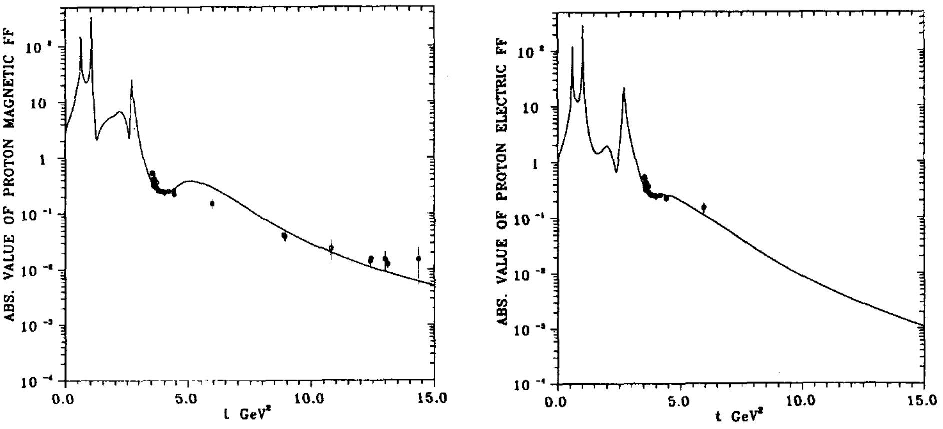

Figure 1.6: Magnetic and electric proton form-factor in the time-like regime. The figure and the fit within the ten resonance unitary and analytic model is from [Dub00].

imentally via Dalitz decays, e.g. $\pi^-p \rightarrow n\eta' \rightarrow n\gamma e^+e^-$ by combining HADES and LAND with the photon spectrometer TAPS. The analysis of the planned pion beam experiments will shed new light on the importance of vector mesons in the coupling of photons to hadrons and provide again a severe test of the vector meson dominance model.

The present still unsatisfactory status in this field are also noticed in [Lan85] where strong deviations from VMD predictions are observed for the ω-transition form factor which can be measured via the $\pi^-p \rightarrow n\omega \rightarrow n\pi^0e^+e^- \rightarrow n\gamma\gamma e^+e^-$ reaction. To corroborate these deviations and to make a high statistics measurement feasible, we could combine HADES and LAND with a large electromagnetic calorimeter with high geometric efficiency. Pion beams are favoured as compared to proton beams due to the higher production ratios for the mesons of interest compared to π^0-mesons. Therefore, the dilepton combinatorial background arising mainly from π^0-Dalitz decay is greatly reduced.

The above mentioned method of measuring the ω meson transition form factor has the drawback of a very small geometrical acceptance due to the exclusive measurement proposed. It also has the difficulty of combining large system of detectors, which is not only a technical problem but it also presents time schedule problems. Lately, a new way to measure the ω meson transition form factor with the HADES spectrometer has been proposed [Rit00] by measuring the reaction $\pi^+p \rightarrow \pi^+p\omega$. This reaction combines the advantage of the π^- beams, e.g. high cross sections, low background, low single rates in the detectors and those of the proton beams, fully exclusive kinematics.

1.2.2 Hadron Properties in the Nuclear Medium

The nucleus-nucleus reaction program at GSI concentrates on studying the properties of hot and dense hadronic matter. One main goal is to determine the global parameters characterizing this medium, like temperature and density, and their relation via an equation of state. With emerging information on these parameters a future challenging aim of the heavy-ion reaction program is to look for precursor phenomena of chiral symmetry restoration. Chiral symmetry is a fundamental symmetry of Quantum Chromodynamics in the limit of massless quarks. Strong interactions break this symmetry dynamically, a phenomenon which is manifest in the mass spectrum of free, light hadrons. Model calculations and lattice QCD results predict a restoration of the Chiral symmetry with increasing nuclear density and/or temperature. A signature of chiral symmetry restoration is the decrease in magnitude of the chiral (quark) condensate as is shown in Fig. 1.7. This implies a corresponding decrease of constituent quark masses which would in turn be reflected in a change of hadron masses in medium. However, theoretical predictions on mass shifts do not agree quantitatively which calls even more systematic experimental studies.

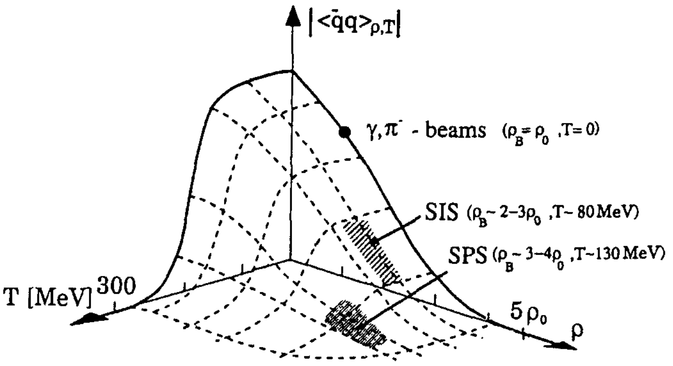

Figure 1.7: The chiral (quark) condensate calculated within the Nambu Jona-Lasinio model as a function of temperature and baryon density [Kli90]. The zones where experimental data from different kind of reactions can be extracted are also shown. The figure is from [Met99].

Substantial effects are expected at the large densities (about 3 times normal nuclear density) which can be reached in the central reaction zone of relativistic nucleus-nucleus collisions at SIS energies. The best probes for possible mass changes are vector mesons (ρ,ω,Φ) which are produced in heavy-ion collisions and have lifetimes comparable to those of the collision zone. Vector mesons have a small decay branch into e^+e^- pairs which escape from the highly compressed nuclear matter without final state interaction. From the measured lepton 4-momentum vectors the mass of the decaying meson can thus be determined and a possible mass change can directly be observed by comparing to the known mass of the free vector meson. The drawback of this approach is that the high nuclear densities are reached only for a very short time in a transient state.

The same model calculations, however, already predict a mass reduction of up to 20 % for vector mesons in nuclear matter at normal density. In complementary approaches, using photon, electron or pion beams vectors mesons can be produced at rest in nuclei for appropriately chosen kinematical conditions. The advantage of this approach is that a possible mass change, although smaller, can be monitored over the full lifetime of the meson without being limited by the finite lifetime of the dense nuclear environment as encountered in heavy-ion collisions. In addition, the pion induced reaction is again much cleaner with correspondingly reduced combinatorial background compared to proton or heavy-ion beams and allows a more direct and less model dependent interpretation of the data. The detector systems to be used are again HADES, LAND, TAPS and/or a large calorimeter.

A drop in the mass of the Φ-meson by more than 30 MeV would make the decay into K^+K^--pairs energetically impossible. An alternative way to detect a mass reduction of vector mesons in nuclei is therefore to compare this decay mode for the free proton and for nuclei using the charged particle detector system FOPI which is ideally suited for studying the $\Phi \to K^+K^-$ decay. A favourable process for almost recoilless Φ-production in nuclei is the $\pi^-p \to \Phi n$ reaction.

Changes in the mass of baryon resonances populated in π-induced reactions can be studied with the two arm photon spectrometer TAPS and the kaon spectrometer KaoS. Since the $N^*(1535)$ resonance is the only baryon resonance with a large $N\eta$ decay branch the observation of η-mesons via their 2 photon decay is a sensitive tag on this resonance in the nuclear medium. The energy position of this resonance and thereby its mass can be deduced from an excitation function of the $\pi^-p \to N^*(1535) \to N\eta$ reaction on nuclei. Analogously, the mass of the $\Lambda(1405)$ resonance at normal nuclear matter density can be deduced from a measurement of the $\pi^+p \to \Lambda(1405)K^+$ excitation function by detecting the K^+ in the KaoS spectrometer.

In conclusion, this part of the pion beam program supplements information from heavy-ion reaction studies and, at the same time, provides an independent test of theoretical predictions that precursor phenomena of chiral symmetry restoration should be observable already at normal nuclear matter density and not only at the higher densities achievable in central heavy-ion collisions.

1.2.3 Hyper-nuclei

We have already mentioned that the pion beam at GSI is a general purpose facility. In fact, there is an open call for proposals where different scientific groups may apply for this beam to realize their experiments. For example, an approved proposal exists for hyper-nuclear γ-spectroscopy.

Λ-hyper-nuclei may be created by the (K^-, π^-) and (π^+, K^+) reactions and can be used for hyper-nuclear γ-spectroscopy [Brü75, Dov80]. In spite of the long history, the existing experimental data are limited mostly to light hyper-nuclei and exhibits relatively poor energy resolution. The pion beam facility provide new opportunities for this field [Ger99], just in time, when large-volume germanium detectors have been introduced to improve substantially the resolution [Tam00].

Hypernuclei produced in π^+ induced reactions have to be detected through the $K^+\gamma$ coincidence, therefore a charged particle spectrometer in coincidence with a γ spectrometer is needed. For GSI, the combination of the kaon spectrometer, KaoS, with VEGA, a high-resolution, high-efficiency array of germanium crystals has been proposed [Ger99]. With this situation, the overall charged-particle energy resolution has contributions from the incident beam, the spectrometer and the target, that have to be considered together with the resolution of the germanium detectors.

In a first stage, there are three targets of particular interest. For ^7Li,and ^{13}C previous measurements and detailed predictions exist. VEGA at GSI will be able to greatly improve the detection efficiency and the precision of the γ energy measurements. In addition, for the first time, it will be possible to measure $\gamma - \gamma$ decay cascades which will aid in identifying observed γ rays in terms of the states involved in the transition. Such measurements will also test model predictions for branching ratios. The proposed measurements on a medium-mass nucleus (e.g., ^{90}Zr) constitute a search for sharp γ lines from inner-shell transitions that have not been observed before.

Some hyper-nuclei studies of this kind are being developed at KEK 12-GeV PS [Tam00]. The main advantage of the GSI in respect of KEK is that a cleaner and better defined beam is achievable. This situation allows to put the gamma detectors closer and increase substantially the efficiency. On the other hand, the pion intensities are lower at GSI, but, in any case, combining both aspects a clear improvement is expected.

1.2.4 Test of detectors

An important application of beams is to test and calibrate different kind of detectors. As we will show, the pion beam facility at SIS is also an effective tool for this purpose.

We can take advantage of the secondary beam to investigate the response of a detector for the particles that are passing through. The fact that the beam is a mix of different kind of particles could be seen as a drawback, but in some cases, it can help because we have the chance to make at the same time tests and calibrations with different particles or/and in a more realistic environment (or background). Another big advantage is that the beam is delivered to the experimental caves of the SIS, where the big systems of detectors are installed. The pion beam is the easiest way, and in most of the cases the only one, able to bring a specific kind of particles for the test and calibration of these systems. The experimentalists have shown a big interest in the electron component of the pion beam. Looking at this more carefully, we see that it is not so odd, because at GSI is easier to get a beam of hadrons than leptons. Next, we will describe some examples of the pion beam for testing and calibrating detectors.

Tests for the ALICE TRD.

The pion beam has already been used for the tests of the prototype for the ALICE Transition Radiation Detector (TRD) [And01], showing that the pion beam can be a successful tool for these purposes. The pion beam, which has a content in electrons of a few percent, is the best suited source of particles for the test of this kind of detectors because the aim of the TRD is the identification of the electrons from the pions. The setup used for the beam tests is sketched in Fig. 1.8. In addition to the ALICE TRD, which is composed of the Drift Chamber (DC) and the radiator (R), the setup consisted of three scintillator counters (S0, S1, S2), a gas-filled threshold Cherenkov detector (Ch), two position-sensitive detectors (XY1, XY2), either multi-wire proportional chambers or silicon strip detectors, and a Pb-glass calorimeter (Pb).

The measurements have been carried out at beam momenta between 0.5 and 2.5 GeV/c. The beam trigger was defined by the S1 and S2 scintillator counters, to which the Cherenkov signal was added as the electron trigger. Both, electron and pion events, were acquired during one spill by using appropriate pion scale-down factors. The events were selected off-line using the correlation between the signals delivered by the Cherenkov and the Pb-glass detectors (see Fig. 3.15). These tests have been useful to take important information about the different radiator behaviours and Drift Chamber operational

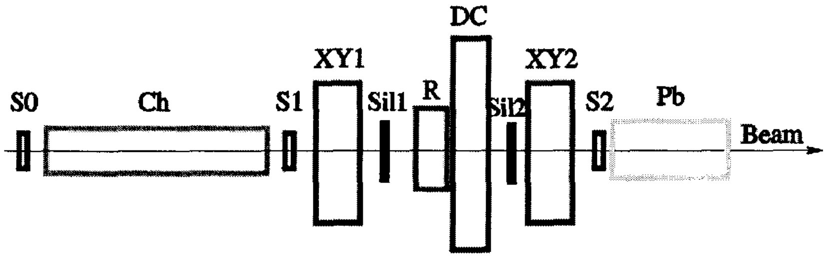

Figure 1.8: The setup used for the beam tests (not to scale). The different components are explained in the text.

conditions. Therefore, a better and more reliable choice of the radiator can be done for the final design of the ALICE TRD.

HADES calibrations with electrons of the pion beam.

It was suggested that the secondary electrons of the pion beam could be used for the calibration of the HADES drift chambers [Met00]. The idea is to scatter the coming electrons with a liquid hydrogen target and use the scattered electron for calibration purposes. However, it is not clear yet if the electron intensities are high enough and it is under discussion if this calibration is feasible.

Chapter 2

Setup of the pion beam-line

In this chapter, the setup of the pion beam is described. There are basically two different setups according to the two experimental areas being served, one line leading to the HADES cave and the other leading to cave C. First, we briefly describe the GSI accelerator complex. Then, we focus on the different components of the beam lines: production target, beam optics and diagnostic detectors.

2.1 The GSI accelerator complex

The GSI is a large heavy ion facility where more than 1000 scientist from 25 countries are doing their research. The experimental physics program contains topics in several areas: nuclear and hadron physics, atomic physics, plasma physics, accelerator physics, material science and radio-biology. Its activity is going beyond the research and lately, it is being used systematically for cancer radiotherapy with heavy ions.

The GSI is able to accelerate heavy ions up to 2 AGeV kinetic energy provided by the 18 Tm SIS. It can also provide protons up to 4.7 GeV kinetic energy. The diversity and quality of the different beams together with the different detector systems makes the GSI a facility unique world-wide for heavy ion research. The pion beam facility, which is recently installed, extends the GSI program to pion beams.

2.2 The pion beam facility

The pion beam facility provides secondary pion beams up to 3 GeV/c momentum. The different beam-lines leading to the major experimental caves in the

SIS target hall are shown in Fig. 2.1. The pion production target is located in the main beam-line coming from the synchrotron. The optical elements of the different beam-lines lead the secondary particles to the respective caves where the experiments are done.

2.3 Production targets

A good choice of the production target is extremely important. From it depends not only the pion production but also the correlated background.

For the study and optimisation of the pion beam factory a set of thick target rods have been used in the HADES and C beam-lines. Their characteristics and relevant physical properties density, mass number, atomic number and radiation length are given in Table 2.1.

Material	Lengths(cm)	$\rho(g/cm^3)$	A_{ef}(g/mol)	Z_{ef}	X_{ef}(cm)	Linc
Be	1, 2.1, 3.2, 10*	1.848	9.012	4	35.28	H
Be	1, 2.1, 3.2, 8, 10	1.848	9.012	4	35.28	C
B_4C	8, 10, 12	2.54	11.07	5.22	19.6	C
Ti	12	4.54	47.867	22	3.56	C

Table 2.1: Sets of production targets. The density, effective mass, atomic number and radiation length of the material are also shown. * indicates that this target is pencil shaped as explained in the text.

The first set of targets, which were used in the HADES beam-line, have a diameter of 7 mm, excepting the 10* cm length target, where $*$ indicates that the target has a diameter of 7 mm and is pencil shaped along the last 3 cm, tapered to a final radius of 4 mm. Afterwards, it was considered more convenient to use targets of 4 mm diameter in the C beam-line. These targets were chosen according to previous experimental data and simulations in order to optimize the pion production intensities and keep the background as low as possible [Lom97]. The shortest beryllium targets were installed for producing secondary nuclear beams by fragmentation and also to study the production of pions as a function of the thickness. The production targets were fixed in a water cooled copper block. Insertion and removal of any of the targets were controlled remotely from the SIS control room. A picture of the production targets installed in their support is presented in Fig. 2.2.

Lately, a small (2x1x1 cm^3) plastic scintillator has been installed in the

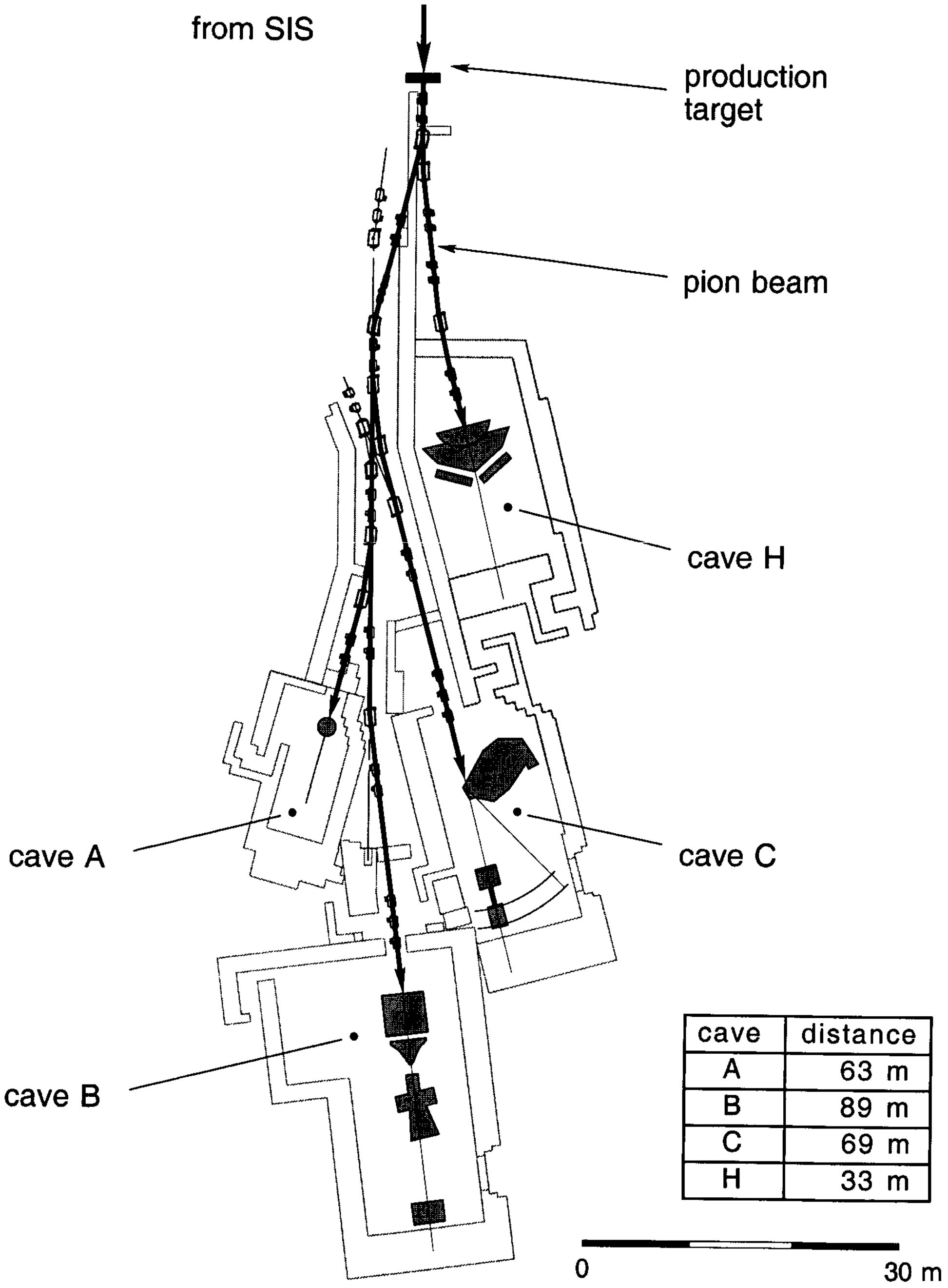

cave	distance
A	63 m
B	89 m
C	69 m
H	33 m

Figure 2.1: Beam-lines in the SIS target hall.

Figure 2.2: Set of production targets used in the HADES line commissioning in September 1998 fixed in their copper support. The three upper targets are 10* cm thick (and they are pencil-like) and the targets below have a thickness of 3.2, 2.1, and 1 cm beryllium, respectively.

upwards side of the production target device. The position of this scintillator can be remotely shifted from the bottom of this device to 30 cm higher in order to protect it from very high intensity rates. The intensity of this small counter complements the monitoring of the SIS intensity. It is a very useful diagnostic tool for a correct focusing of the beam at this sensitive point.

2.4 Beam-line optics

We are concerned here with the study of the beam in the HADES and C beam-lines where the commissionings and experiments have been done. These beam-lines are presented in two different levels of details in Fig. 2.3 and Fig. 2.4, respectively. The position of the different beam-line elements are given in Tables 2.2 and 2.3.

Although at first glance, both lines look very different, their design is equivalent. After the production target, there are a quadrupole doublet, a dipole and a second quadrupole doublet, after which the hodoscopes H_1 and H_2 are placed (H_1 does not appear in Fig. 2.4 because it was not used in the C beam-line experiments but it should be there if used). The dipole D_2 in Fig. 2.4 is the main difference of both lines. It has no correspondence in the HADES beam-line, but it was introduced because the beam has to be swung in order to reach

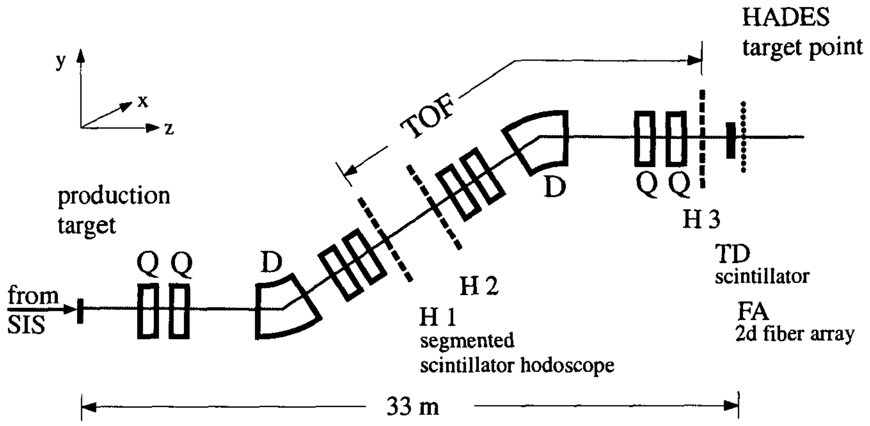

Figure 2.3: Schematic drawing of the pion beam-line leading to HADES cave and its different elements.

the beam-line going to cave C. it follows a quadrupole doublet, a dipole (dipole doublet for C beam-line) and another quadrupole doublet. Finally, the third hodoscope and the diagnostic detectors are found. In the C beam-line, due to the long distance from the production target to the cave target, a quadrupole triplet is needed at the end in order to have a good focus at the cave target point.

The $B\rho$ value of the beam-lines can be set up to 10 Tm to select the central momentum of the acceptance window. Thus, pions up to 3 GeV/c momentum can be provided.

The aperture of the quadrupoles is 6 cm in both X and Y direction, whereas the aperture of the dipoles is 6.5 cm in the X direction and 3.5 cm in the Y direction.

2.4.1 HADES beam-line optics

In Fig. 2.3 the positions of the beam-line optical elements, dipoles (D) and quadrupoles (Q), of the HADES beam-line are shown. Their positions and their characteristic constants, constant k for the quadrupoles and curvature

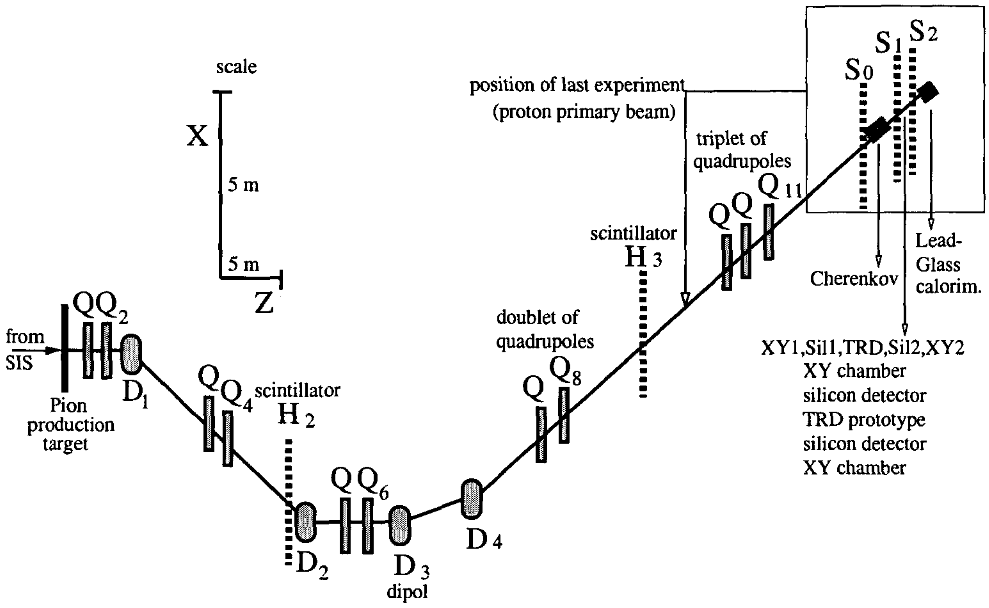

Figure 2.4: Schematic drawing of the pion beam-line leading to cave C and its different elements.

radius ρ for the dipoles, are given in Table 2.2.

This beam-line comprises two dipoles and 4 quadrupole doublets and has been designed for a momentum dispersion $\Delta x/(\Delta p/p)$ of -9 mm/%. The HADES target point is 70 cm higher than the pion production target. To transport the beam, the two dipoles had to be tilted slightly with respect to the horizontal plane in such a way that the first dipole introduces a vertical momentum component in the beam and the second dipole restores the momentum on the horizontal plane. The beam-line has a momentum acceptance window of about 8% (see section 4.2.3 for more details).

2.4.2 C beam-line optics

Fig. 2.4 shows the scheme of the C beam-line. The positions of the beam optical elements and their characteristic constants are given in Table 2.3.

As it has been mentioned at the beginning of the section, the beam-line leading to cave C is more complex than the HADES one due to the longer distance and to the difficulty to connect the beam-line coming from SIS to the beam-line leading to cave C (see Fig. 2.1). As a result, a greater number of optical elements are needed. The whole beam-line is in a single horizontal

Element	Pos. X [cm]	Pos. Y [cm]	Pos. Z [cm]	k[m^{-1}], $\rho(m)$
Prod. Target	0.00	0.00	0.00	
Q1	0.00	0.00	140.0	1.073055
Q2	0.00	0.00	340.0	−0.714676
D1	0.00	0.00	831.74	−11.2500
Q3	48.95	19.53	1232.02	0.734486
Q4	65.92	26.30	1370.83	−0.718936
H1	74.73	29.81	1442.89	
H2	100.75	40.19	1655.68	
Q5	109.56	43.71	1727.25	−0.718936
Q6	126.54	50.48	1866.55	0.734486
D2	175.48	70.01	2266.83	−11.2500
Q7	298.79	70.01	2763.49	−0.656742
Q8	346.98	70.01	2957.60	0.755037
H3	369.29	70.01	3047.47	
HADES Targ.	431.30	70.01	3297.46	

Table 2.2: Elements of the HADES line and their positions. The last column shows the quadrupole constants k in m^{-1} and the curvature radii ρ of the dipoles in m.

plane and has a lower acceptance than the HADES beam-line due to its longer length. More details about the acceptance of this beam-line is given in section 4.2.3.

2.5 The beam-line detectors

In order to know the beam intensity and profile, to discriminate the different kind of particles of the beam and to have a precise measurement of the momentum of the transported particles we need a collection of detectors in the beam-line. Below, we present the detector systems used in the different beam-lines.

2.5.1 Detectors in the HADES beam-line

During the commissioning experiments three detector systems were installed along the pion beam-line: three segmented hodoscopes to track particle trajectories and provide time-of-flight measurements, a plastic scintillator at the

Element	Pos. X [cm]	Pos. Z [cm]	k[m^{-1}], $\rho(m)$
Prod. Target	0.00	0.00	
Q1	0.00	140.0	1.073055
Q2	0.00	340.0	−0.714676
D1	−9.97	529.48	6.241347
Q3	−199.13	1299.59	−0.332621
Q4	−249.27	1493.21	0.391076
H_2	−412.24	2122.44	
D2	−447.13	2296.89	−6.245022
Q5	−457.10	2564.64	0.00
Q6	−457.10	2764.64	0.00
D3	−452.29	2948.07	−11.250000
D4	−376.48	3523.92	−11.250000
Q7	−191.68	4232.19	−0.376912
Q8	−139.92	4425.38	0.420390
H_3	54.03	5149.18	
Q9	231.32	5810.84	−0.476054
Q10	283.08	6004.02	0.655234
Q11	334.84	6197.21	−0.583438
S_0 / KaoS Targ.	487.55	6767.11	
Cherenkov detector	592.37	7183.05	
S_1	620.84	7264.56	
XY1,Sil1,TRD,Sil2,XY2	633.27	7300.13	
S_2	645.69	7357.29	
Lead-glass calorim.	648.83	7366.55	

Table 2.3: Elements of the C beam-line and their positions. All the elements are in the horizontal XZ plane. The last column shows the quadrupole constants k in m^{-1} and the curvature radii ρ of the dipoles in m. The XY1,Sil1,TRD,Sil2,XY2 represent the set of detectors formed by the first XY ionization chamber, the first silicon detector, the TRD prototype, the second silicon detector and the last XY chamber. A scheme of the last detectors is shown in Fig. 1.8.

HADES target position with the purpose of measuring the total number of particles crossing this point and a fiber scintillator array to determine the beam profile behind the HADES target position and the focal point of the beam.

The time-of-flight hodoscopes

These detectors are certainly the most important detectors of the pion beam, because they are used for the time discrimination and momentum measurement of the particles. The election of this kind of detector is based on two requirements. Firstly, the required momentum resolution for the various experiments is about $\Delta p/p = 0.5\%$ which is significantly better than the 8% momentum acceptance of the beam-line. Therefore, an additional momentum measurement system was introduced based on tracking the pion trajectories. Secondly, other particles produced along with the pions and having the same charge will be transported as well. Positive pion beams are contaminated with positrons, positive muons, positive kaons, protons and nuclear fragments, while negative pion beams contain electrons, negative muons and kaons. In order to have a clean beam, pions have to be discriminated from other particles. Time-of-flight measurements is one of the standard techniques employed for separating particles of different mass and this method is applied here. These requirements were satisfied by using three segmented hodoscopes, indicated as H1, H2 and H3 in Fig. 2.3. They were installed along the pion beam-line to achieve both momentum determination and mass separation. The first two hodoscopes H1 and H2 were placed between the second and third quadrupole doublet, as shown in Fig. 2.3. In this region the beam is dispersively defocused and distributed on a relatively large cross section, which allows to keep the count rate of the individual hodoscope modules at acceptable values. In addition, this defocusing produces a useful correlation between the momentum and point of impact in the hodoscopes which can be exploited to determine the momentum of particles as described in section 3.1.3. The position of the third hodoscope, H3, was chosen such that the distance with respect to both H1 and H2 is as long as possible to optimize particle discrimination by time-of-flight.

Previous simulations showed that a segmentation of the first two hodoscopes of 1 cm in the horizontal direction and a segmentation of the third hodoscope of 0.65 cm in the vertical direction would allow to obtain the required momentum resolution and to cope with the high counting rate expected. With this choice, the counting rate is kept below 10^6 counts/s per rod at the highest intensities of the primary beam. The first two hodoscopes are composed of 16 rods of BC404 plastic scintillator of 1 cm width, 0.5 cm thickness and 10 cm length, while the third hodoscope has 16 rods of 0.65 cm width, 0.65 cm thickness and 10 cm length. The scintillation light is read on both sides by Hamamatsu R3478 photo-multiplier(PM) tubes which were selected for their excellent time resolution and small size. The scintillators were coupled to plexiglas light-guides glued to the PM tube windows. The light-guides of the first

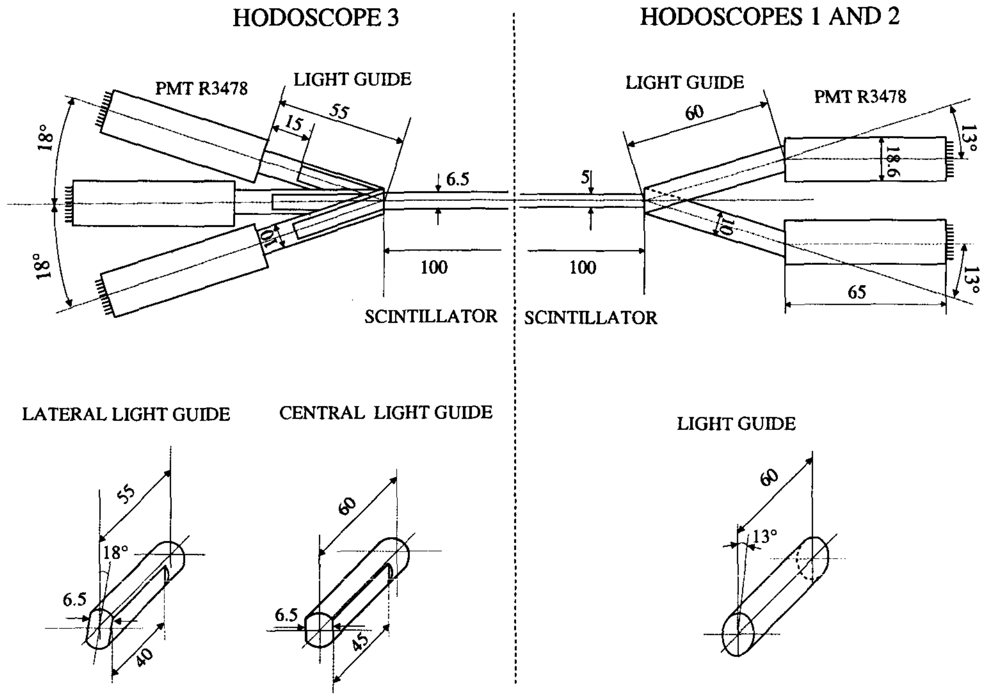

Figure 2.5: Drawing of the scintillator modules of the first and second hodoscope (right) and third hodoscope (left). Only half of the modules are shown, the other half is symmetric. Detailed drawings of the corresponding light-guides are given as inserts in the bottom of the figure. Units are given in mm.

and second hodoscopes formed an angle of ±13° with the plastic scintillator in order to fit the PM tubes into the available space. The more compact design of the third hodoscope required to alternate modules with light-guides tilted an angle of ±18° with modules with straight light-guides. The scintillators and light-guides were wrapped with 40 μm aluminum plated mylar to make them light-tight. A technical drawing of the scintillator modules and their assembling is shown in Fig. 2.5.

In order to avoid a signal reduction associated to high counting rates, active photo-multiplier voltage divider chains were used. The chains are designed by SINKO (St. Petesbourg, Russia) closely following the emitter-follower scheme of Kim et al. [Kim96, Mur02].

The hodoscopes were housed in black metacrilate boxes as shown in Fig. 2.6. The boxes were screwed to the flanges of the beam-line pipe for high accuracy positioning. The connectors needed for scintillator signal cables and high volt-

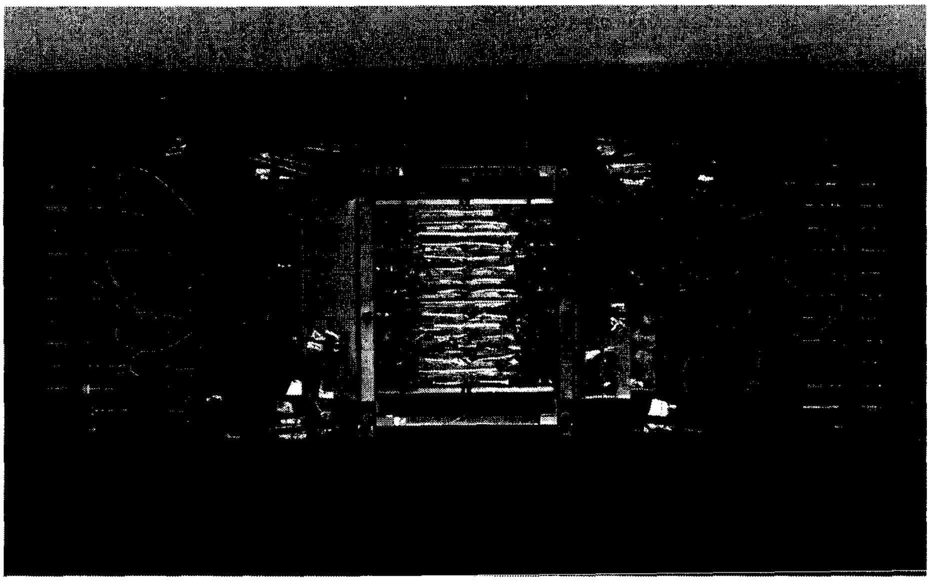

Figure 2.6: Third hodoscope mounted inside its metacrilate housing.

age cables were installed on the metacrilate boxes. The use of feed-through connectors, SHV for high voltage and LEMO for scintillating signals, facilitates the installation of the hodoscopes without an observable deterioration of the time profile of the scintillator signals.

The hodoscopes were equipped with a laser source sending light pulses to each PM tube through quartz fibers with a three-fold purpose: to have a time reference, to monitor the electronics during the experiment and to correct in the off-line data analysis for drifts in the electronics. A N_2 pulsed laser of 3 mW power which radiates ultraviolet light (337 nm) was used. The direct laser signal was fed into four 1 mm optical fibers which in their turn were split into bunches of 16 quartz fibers of 200 microns diameter. These fibers, previously polished to provide uniform splitting of light, were directly coupled to the windows of the PM tubes. The laser was operated at a frequency of 20 Hz during the experiment. A trigger for laser events was implemented by means of a reference PM which was directly illuminated by the laser.

Target detector

In order to determine the pion intensity at the HADES target position during the experiment a hexagonal ($\phi = 10\ cm$) 1 cm thick plastic scintillator read out by a Phillips XP2972 photo-multiplier was installed. A dedicated trigger was implemented for this detector.

The scintillating fiber array detector

An array of 48 BCF92 Bicron scintillating fibers read out in groups of 16 by position sensitive H6568 Hamamatsu photo-multipliers was placed 2.85 m downstream of the third hodoscope. This detector was used to reconstruct the focus of the secondary beam [Har99] and to provide an additional signal for the beam particles crossing the HADES target position. A sketch of this detector is shown in Fig. 2.7.

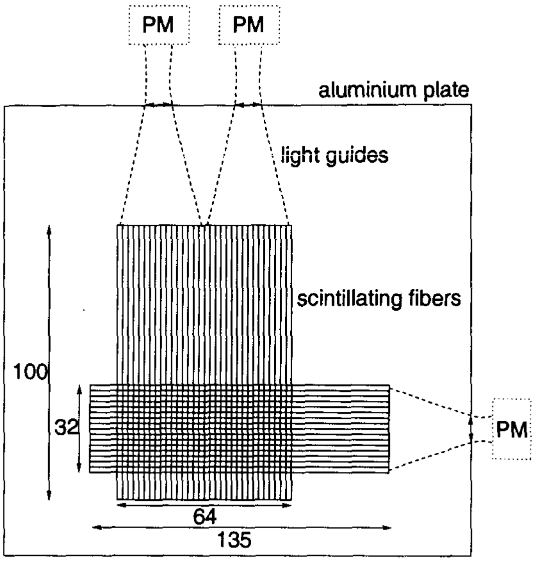

Figure 2.7: Sketch of the scintillating fiber array. Dimensions are given in mm.

The scintillating fibers were coupled through optical fibers to the photomultipliers and were wrapped with 0.15 mm thick teflon foil in order to reduce light background and cross-talk. The surface of this detector is 6.4 × 3.2 cm^2 and the spatial resolution is about 2 mm along the coordinate axes.

Electronics setup

The electronics setup consisted of a combination of VME and CAMAC modules. The electronic modules, apart from the VME crate, were placed in the HADES cave. The VME crate was placed in the counting room, separated from the CAMAC crates by about 90 ns of cable length. High quality RG58 signal cables were used to transport the PM signals from the hodoscopes to the electronics; 22 m and 10 m long cables were needed to transport the signals from the two first hodoscopes and from the third hodoscope, respectively. Each scintillating signal had to be split into three for timing, energy integration and triggering. The required timing accuracy of the order of 100 ps did not allow to perform active splitting of the signals. For this reason, the signals were fed directly into 8-channel CAMAC GSI 8001 constant fraction discriminators (CFD). These modules provide one OR output for the eight input channels, two differential ECL outputs per discriminated signal, and two additional analog outputs, operating as active splitters after discrimination. One of the analog outputs was used for energy integration. The OR output was used to make triggers for individual hodoscopes. The first of the logic outputs were sent as individual stop signals to the TDC modules. The second logic outputs were sent to the scalers that recorded individual channel rates. In order to reduce cross talk effects, the signal cables from the hodoscopes were connected to the CFD discriminators in such a way that neighbouring rods of the hodoscopes were never read into neighbouring CFD channels. Triggers were derived for the laser events, the target detector, the fiber array detector, and for each hodoscope. The triggers of individual hodoscopes consisted of the OR of the 32 hodoscope channels. The coincidence trigger was then produced as the AND of the three individual hodoscope triggers. A GSI TB8000 trigger box was used to implement the triggers. This module has the possibility of selecting suitable reduction factors for each individual trigger in order to adapt the rate of accepted events to the speed of the acquisition system. In addition, triggering was inhibited by the busy signal of the VME controller. Trigger signals that were neither inhibited nor scaled down were counted by scalers for an off-line dead time correction. The Master Trigger output of the trigger box was used to build the Common Start signal for the Phillips 7186H TDC modules and the gates for the Silena ADC 4418/Q charge integration modules. To postpone the arrival of the individual signals at the acquisition system, so that they come after the trigger signals, the TDC START and STOP logic signals were delayed by 500 ns using GSI DL1610 active delay modules which are designed for high accuracy timing.

Energy signals were delayed by means of cable delay. The overall loss in time resolution by the electronics is estimated to be around 50 ps. This should be compared to the total resolution of 110-150 ps presented in section 3.1.1. The trigger scheme is shown in Fig. 2.8.

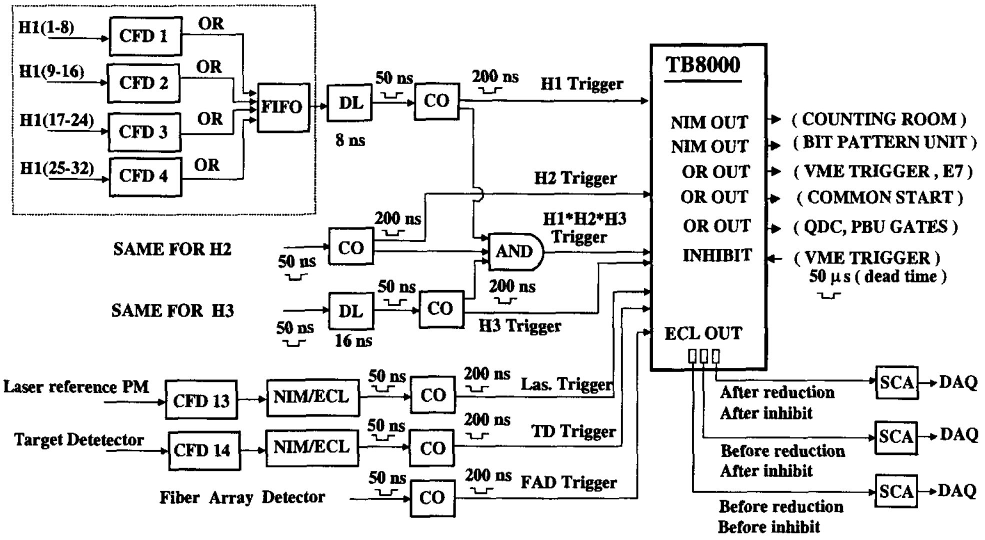

Figure 2.8: Scheme of the electronics setup of the different triggers used.

Data acquisition and data analysis

The experimental data were taken with the MBS [Bar97] data acquisition system developed at GSI. The event structure contained the time and energy signals provided by each hodoscope scintillator, the energy signals of the target detector and fiber array detector, the trigger pattern and the scalers of all the CFD channels and triggers. The data acquired during the experiment were recorded on DLT magnetic tapes and analysed off-line with the help of PAW [Paw95] based code APE [Sam92], which decodes the raw events and stores the relevant data in PAW n-tuples.

2.5.2 Detectors in the C beam-line

The experiments in the C beam-line had a double objective. The first one was to do a commissioning of the C beam-line itself and have a knowledge of different characteristics of this beam-line as intensities, acceptance and particle ratio. The second objective is to use this secondary beam for the first application of the pion beam factory at GSI: tests and calibrations of the TRD ALICE prototypes with electrons and pions. Therefore, we were interested not only in pion production, but also in electron production and identification.

According to the new needs and trying to improve the efficiency of the data acquisition system, the experimental setup was changed. For instance, the hodoscopes were not installed, due to the fact that they were not necessary for the mentioned purposes and they were previously tested in the HADES beam-line. Besides, their installation would have complicated unnecessarily the setup and decreased the acquired event rates. Instead, a series of individual plastic scintillators along the beam-line were installed, as shown in Fig. 2.4. These detectors were used to discriminate particles by time-of-flight and to measure the intensity of particles at these points. In addition, the diagnostic detector system was composed of a Cherenkov detector and an electromagnetic calorimeter for electron identification. Finally, we also had two drift chambers and two micro-strip silicon detectors to get information about the beam profile near the target of cave C. A scheme of the last part of the beam-line is shown in Fig. 1.8. A picture of the last part of the setup is shown in Fig. 2.9.

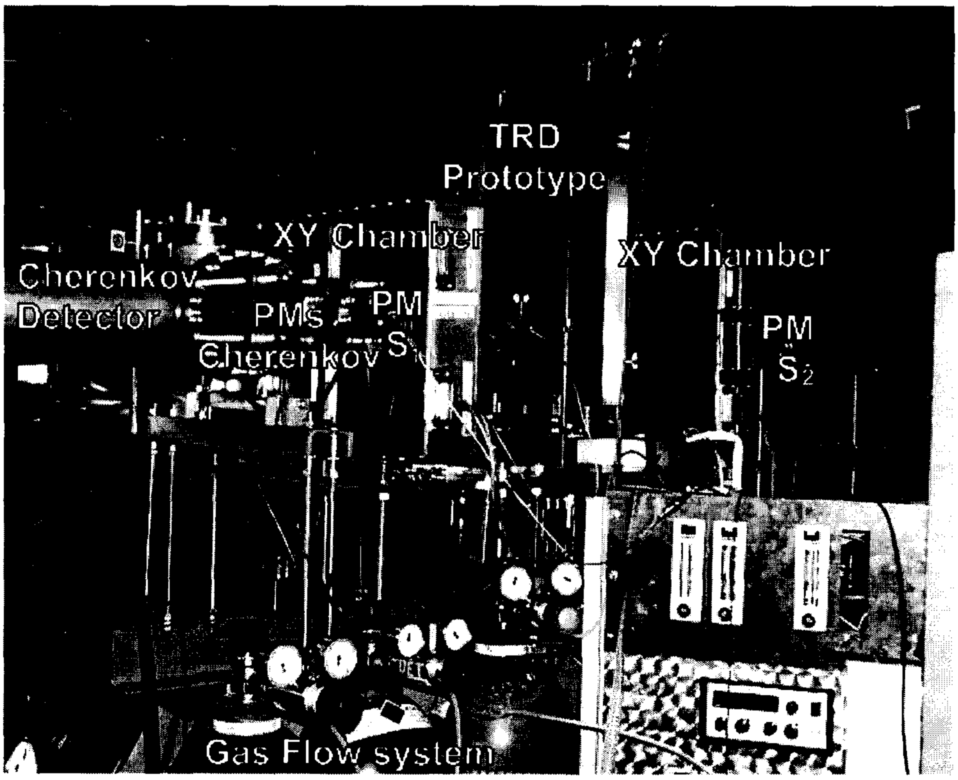

Figure 2.9: Picture of the setup in cave C.

Scintillators along the beam-line

We used 5 plastic scintillators, labelled as H_2, H_3, S_0, S_1 and S_2 in Fig. 2.4. The first two scintillators H_2 and H_3 were in the hodoscope 2 and 3 positions, respectively, but they were not used as a position sensitive detectors. They were two hexagonal ($\phi = 6.5\ cm$) NE102 plastic scintillators with a thickness of 5 mm. A light-guide connected one side of the scintillator to the PM. Their position (in or out the beam-line) was remotely controlled. by putting them inside a mobile box, which had 0.1 mm thick stainless steel walls. This allowed us to use them for optimizing the beam-line, and afterwards removing them to avoid a loss of the intensity of particles. With the information of the intensities obtained from these detectors we could set more reliably the optical elements. At the same time they were very helpful to study the effects of matter in the beam-line. Another use of these detectors was the time-of-flight measurement employed for particle discrimination.

The other 3 scintillators were placed near the target of the cave C. In fact, S_0 was exactly in that position. It was a big scintillator 19x20 cm^2 area and 1 cm thickness. The main purpose of this detector was the measurement of the total intensity at the target position. Scintillators S_1 and S_2 have dimensions of 5x10 cm^2 area and 1 cm thickness. The coincidence signal in these two detectors informs that a particle cross the TRD module. This coincidence was usually one of the triggers.

All these detectors also give us an energy signal which is specially helpful to discriminate nuclear fragments with charge greater than one when the beam-line is set to positive polarity.

The Cherenkov detector

Cherenkov light was produced in an aluminium tube of 14.5 cm diameter and 190 cm length. It was filled with CO_2, N_2 or air. At the end of the tube, there was a flat mirror that reflects the light to two photomultipliers. Under the conditions of the experiment and in the momentum range of the pion beam, electrons (or positrons) were the only particles that produced Cherenkov light. In conclusion, it was a very good detector to discriminate and have a trigger for this kind of particles.

The electromagnetic calorimeter

This was a lead glass calorimeter with dimensions 7x10x24 cm^3. This detector gives a higher signal for electrons than for other particles. Although it is not a threshold detector as the previous one, the combination with the Cherenkov detector produces a cleaner discrimination signal for electrons, as it can be seen in Fig. 3.15.

The drift chamber

Two drift chambers gave XY information of the particles in order to reconstruct the track and to get the beam profile near the target position. Each of the chambers contained 200 horizontal and 200 vertical wires separated 1 mm from each other. The readout of the chamber was done in the following way: for each wire a characteristic delay was applied, and then all the outputs of these 200 wires converge on a unique output that was read by a TDC. According to the time channel we know the wire that was responding and consequently the corresponding position.

The micro-strip silicon detectors

Two micro-strip silicon detectors were used to track the particles with higher accuracy. The area covered by these detectors was 32x32 mm^2. It was smaller than in the case of the drift chambers, but they have the advantage of having a better spatial resolution. Each device is composed of 1280 separate readout strips arranged at intervals of 25 μm. The thickness of the silicon is 300 μm, which implies that for a minimum ionising particle, the average energy loss is 90 keV, i. e. 25000 electron-ion pairs are produced. In order to collect all the charge, a voltage of at least 60 V was applied. Although only one of two strips are read, a resolution better than 50 μm is obtained by calculating the center of gravity of the charge collected. A resolution of this order was necessary for the TRD test.

The electronic setup

Like in the HADES beam-line, there was a combination of VME and CAMAC modules. In this case, all the electronics was in the counting room, where all the signals were brought. The operation of these modules is basically the same as in the HADES cave, therefore we only will add some comments. The signals from the photo-multipliers (scintillators, Cherenkov and calorimeter) were brought to a linear fan-in fan-out Lecroy 428F, from which two outputs were used. The first output was delayed and brought to one of the 12 channels of an ADC LRS 22498W. The second output went to a constant fraction discriminator, the output of which was three-fold splited by a logic fan-in fan-out Lecroy 429A. The first logical output was delayed to make the STOP of the TDC, the second output was brought to a scaler to record individuals rates of each detector and the third one was brought to a coincidence module to implement the triggers. To make the triggers a GSI TB8000 module was used. The triggers were the S_1 and S_2 coincidence, and this coincidence plus the Cherenkov for the electron trigger. The drift chambers signals were read by a TDC Lecroy 2228A module. A 20 KHz pulser connected to the scaler was used as a clock. The MBS system was used for data acquisition and the event structure was composed of the time and energy signals of every PM, the time of the drift chambers, the trigger pattern, the scalers of individual rates, clock and triggers and, finally, the information from the TRD. The data acquisition system information was automatically loaded on disk by the acquisition module E7.

Chapter 3

Experimental data

In this chapter we describe the results of the experiments in the HADES and C beam-lines. For each beam-line, we look at the performance of the experimental setup and at the different results extracted from the experiments, such as momentum and time resolution, intensities as a function of the momentum, primary beam, production target and detectors in the beam-line.

3.1 Experiments in the HADES beam-line

Here, we describe the results of the commissioning performed with protons and ^{12}C primary beams at several energies using beryllium production targets and different polarity (charge selection) of the beam-line, shown in Table 3.1. Some of these results have already been described in [Día02].

Projectile	Energy (AGeV)	Target (lengths in cm)	Polarity
^{12}C	1.2	Be(10*)	+, -
	1.7	Be(1, 2.1, 3.2, 10*)	-
	2.0	Be(1, 2.1, 3.2, 10*)	-
proton	1.6	Be(10*)	-
	3.5	Be(1, 2.1, 3.2, 10*)	+, -

Table 3.1: Conditions of projectile, primary beam energy, production targets and polarity of the beam-line used in the experiments performed in the HADES beam-line.

In first place, we look at the performance of the experimental setup and discuss the momentum calibration and resolution of the pion beam-line. Then, we study particle discrimination and the particle ratios of the different components of the beam. Finally, we study the intensity of pions and electrons as a function of the momentum, primary beam and target thickness.

3.1.1 Performance of the experimental setup

The adjustment of the optical elements of the HADES beam-line was done as foreseen in a previous design and the response of the magnets was excellent. The pion production target is placed in the beam-line from SIS to HADES cave, so no special optical adjustment was needed. In this experiment the relevant features of the pion beam-line investigated were the efficiency and maximum count rate that the hodoscopes can accept and the time-of-flight and momentum resolution. In this section, we report on the behaviour of the hodoscopes at relatively high counting rates, particularly about the time-of-flight resolution. The mass resolution achieved at different momenta and the accuracy in the momentum reconstruction of the particles from the tracking information provided by the hodoscopes are discussed in section 3.1.3. Moreover, particle discrimination achieved by the system of detectors is described in section 3.1.4.

Performance of the hodoscopes

The trajectories of the particles are defined by the scintillators responding in each hodoscope. Time-of-flight spectra were obtained for each H1-H2-H3 trajectory. The trajectories with higher statistics were always those corresponding to equal or neighbouring rods in the two first hodoscopes.

Two time signals were read out for each rod and the average of these signals was utilized to avoid position sensitivity in the time determination. The time calibration was performed with a time calibrator that produces a bunch of narrow pulses separated by 10 ns which are fed into the CFD channels. A linear behaviour was found over the full TDC's range. For each individual rod combination the time-of-flight spectrum was fitted by a Gaussian and this defined the peak position and the width (σ) of the distribution. Times are measured with respect to the COMMON STOP signal and therefore contain individual TDC offsets which were corrected for by requiring that the time-of-flight of pions of 2.5 GeV/c between different rods in each hodoscope has the same value.

As an overall result we find that the time-of-flight resolution (σ) between hodoscopes H1 and H3 or H2 and H3 varies from 100 ps to 150 ps, with most of the rod combinations giving $\sigma < 120$ ps [Mur02]. This is independent of the choice of beam or momentum setting of the beam-line. This resolution has contributions from the scintillators and PM tubes and from the electronics. The time resolution of the electronics for individual channels (comprising both CFD and TDC modules) has been estimated from the width of the peaks produced by the time calibrator. This was on average less than 50 ps, but with a wide distribution between 30 ps and 100 ps. The time resolution of the scintillator modules deduced from these results varies between 70 ps and 100 ps.

The time peaks corresponding to laser events revealed the existence of a significant timing drift of the electronics over several hours. For recording during short times the drift was however well below 50 ps. The time-of-flight was corrected for drift by utilizing the laser events.

The performance of the hodoscopes at high counting rates was studied in detail with the production target removed and the proton beam sent directly into the pion beam-line. The beam intensities varied between 10^4 particles/s and several times 10^6 particles/s. The primary beam intensity is not constant during the spill and this fact has been used to collect data at different bombarding rates. The effective bombarding frequency per rod, I, is calculated event by event with the help of a 10 kHz pulser clock:

$$I[kHz] = 10\frac{N}{C}, \tag{3.1}$$

where N is the number of hits in the specific rod and C the number of clock pulses. The time of flight resolution as a function of the frequency is showed in Fig. 3.1. For this plot we have selected a central rod in hodoscopes 1 and 3. The frequency corresponds to the rod of the hodoscope 1. For the rod of hodoscope 3 the frequency is much lower due to the fact that the intensity in hodoscope 3 is distributed over the 16 rods whereas in hodoscope 1 is focused in one or two rods. We can see that there is a smooth worsening in time resolution between 110 and 140 ps.

At a count rate of about $3\cdot10^6$ particles/s a strong decrease in the amplitude of the PM signals was observed in a monitoring oscilloscope. The time-of-flight resolution (σ) between H1 and H3 or between H2 and H3 is around 100 ps up to a counting rate of about 10^6 particles/s, for the best rod combinations. At higher rates the time-of-flight resolution gets worse. At $2\cdot10^6$ particles/s the resolution is around 150 ps. The detailed analysis of these data is described in [Mur02].

The efficiency of each hodoscope has been measured through the coincident events triggered by the target detector which have a multiplicity of at most one in each of the three hodoscopes (at most one scintillator in each hodoscope responds). These events correspond to particles that have passed through all

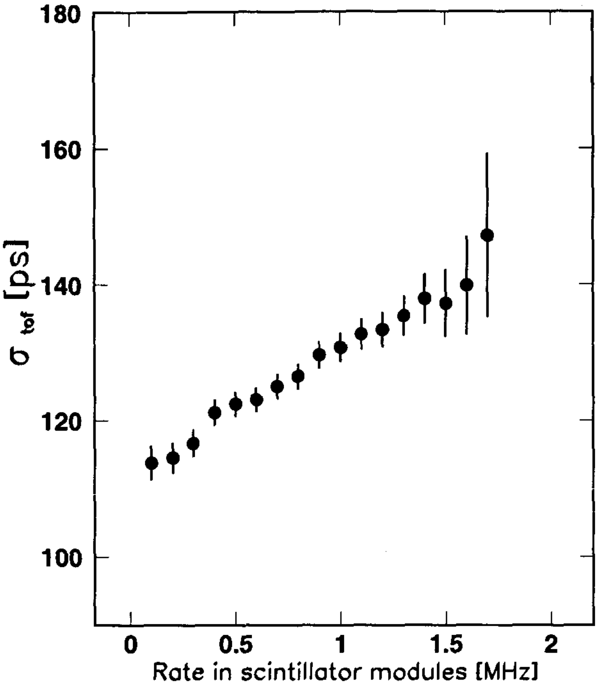

Figure 3.1: Time of flight resolution as a function of the rate in scintillator module in hodoscope 1.

the three hodoscopes. The events with a multiplicity larger than one in any of the hodoscopes have been disregarded for this analysis. The hodoscope efficiency has been defined as the ratio between coincident events and events detected in the other two hodoscopes, for example, $\epsilon_1 = H1 * H2 * H3 * TD/H2 * H3 * TD$ in the case of H1. These efficiencies, shown in Fig. 3.2 as a function of the beam momentum, are always close to 1. They characterize only the geometrical efficiency of the hodoscopes and the threshold setting quality and do not exhibit any significant variation with momentum.

3.1.2 Background rate

Events with a multiplicity larger than 1 or with missing information in a hodoscope have been considered as background. In an attempt to quantify the

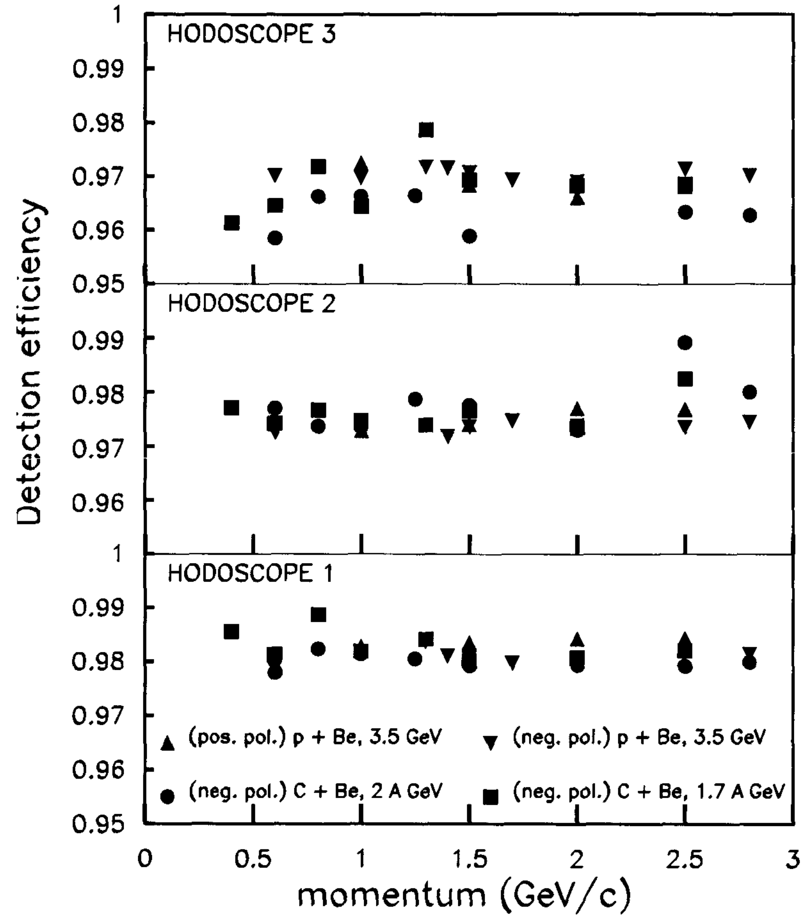

Figure 3.2: Efficiency of the three hodoscopes for particles arriving to the target (multiplicity 1) versus central momentum for the different beams used in the experiment and for both polarities.

background of a given hodoscope, it has been defined as the relative difference between the total number of events in the hodoscope and the number of coincident events with multiplicity 1 in the three hodoscopes. These numbers of events have been derived from the information provided by the scalers which were not inhibited by dead time. For hodoscopes H1, H2 and H3, the background ratio varies between 85% and 99.4%, between 74% and 98%, and between 2.8% and 5.4%, respectively, depending on the primary beam and central momentum settings.

3.1.3 Momentum calibration and resolution

The fact that the beam is defocused between the hodoscopes H1 and H2 and that the x-coordinates in the hodoscopes of particle trajectories depend strongly on the particle momentum has been used to obtain the momentum calibration. Varying the $B\rho$ setting of the beam-line for a beam of fixed momentum produces the same modification of particle trajectories as varying the momentum of the beam in the opposite sense with $B\rho$ fixed. This was used to obtain a relation between the momentum of the particles and the x-position of particle trajectories in the hodoscopes by removing the production target and letting a direct proton beam of 1.6 GeV incident energy into the pion beam-line. The $B\rho$ value was shifted by ±2%, ±5%, and 7% from the central value. In Fig. 3.3 (top panel) the correlation between the x-position in H1 and H2 hodoscopes for different $B\rho$ values is shown. The centroids of these distributions follow a straight line. In the middle panel of Fig. 3.3, the distribution of events is projected onto the $(x_1 + x_2)/2$ axis. As the momentum dispersion of the incident primary beam is negligible, the width of the $(x_1 + x_2)/2$ distributions is related to the momentum dispersion of particle trajectories. The widths of the projected distributions are slightly smaller than 0.4%, which gives an estimate of the momentum resolution of the pion beam-line. In the bottom panel of Fig. 3.3, the relative variation of momentum versus $(x_1 + x_2)/2$ is plotted. There is a linear correlation between these two quantities. This correlation has been exploited to obtain a momentum calibration from $(x_1 + x_2)$.

As the momentum resolution and momentum calibration are of crucial importance in determining the feasibility of a given experiment, it is necessary to check the momentum calibration procedure and to measure the momentum resolution also in the case of a secondary beam. With this purpose in mind, we have compared the momenta obtained from the calibration as a function of $x_1 + x_2$ to the momenta obtained directly from time-of-flight measurements. We present the results for the case of a secondary proton beam of 1 GeV/c central momentum. The primary proton beam and the outgoing protons produced by the re-scattering and reaction processes in the production target were transported along the beam-line. In Fig. 3.4, the momentum of the protons determined from the TOF is compared to the momentum set by the $x_1 + x_2$ scintillator rod position in the first two hodoscopes. The linear correlation is quite good, albeit with a slight deviation from unity slope as seen in Fig. 3.4.

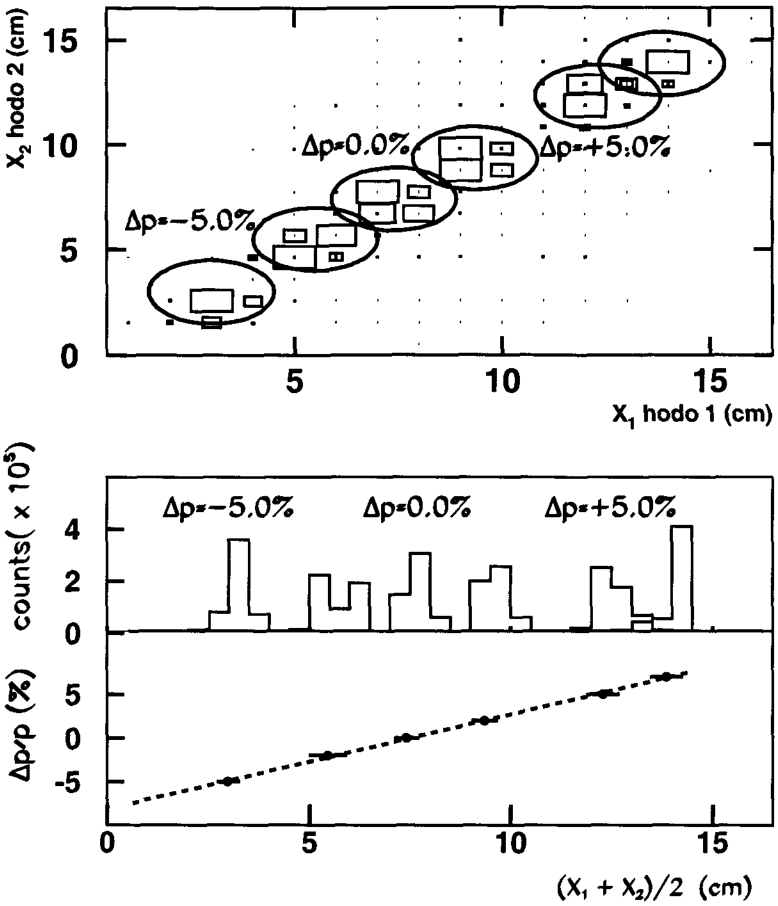

Figure 3.3: Momentum calibration. In the upper picture, the bidimensional plot of the x coordinate in H2 versus the x coordinate in H1 for the six $B\rho$ settings measured is shown. In the central picture, the projection of the number of counts versus $(x_1 + x_2)/2$ is plotted. In the lower picture, the relative variation of momentum versus $(x_1 + x_2)/2$ is represented.

This discrepancy is probably due to the fact that the momentum from the TOF information is inaccurately calculated because the dependence of the exact path-length of the individual particle trajectories in the pion beam-line on

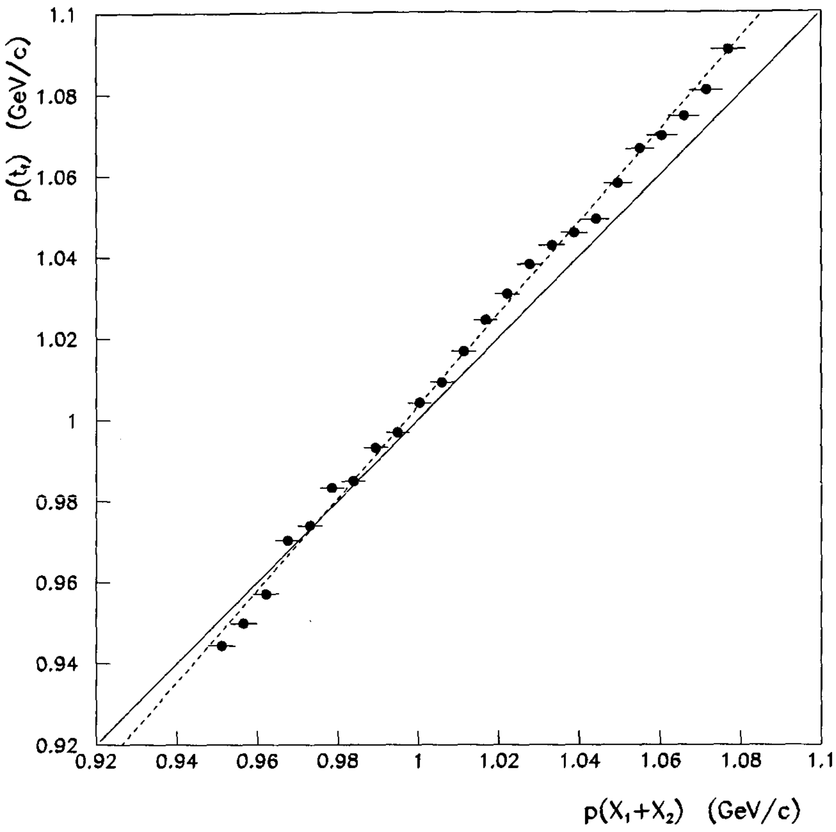

Figure 3.4: Momentum from time-of-flight information versus momentum from impact position in the hodoscopes. The dashed line is a linear fit to the data and the solid line is a linear fit for vanishing coordinate in the origin. It is seen in the figure that the momentum resolution is of the order of 0.5%.

momentum has been ignored in this calculation. The deviation between time-of-flight and hodoscope coordinate momenta is however important only outside the central part of the acceptance window, where the number of transported pions is small. The momentum resolution is thus related to the fluctuations around the linear correlation of Fig. 3.4. It is found to be within 0.5%, in agreement with the results of the calibration in Fig. 3.3.

3.1.4 Particle discrimination and particle ratios

Particle masses can be calculated from time-of-flight measurements, provided the momentum is known, by the equation

$$mc^2 = \frac{pc}{l} \cdot \sqrt{(ct_f)^2 - l^2}, \tag{3.2}$$

where l is the length of the trajectory between one of the first two hodoscopes and the third one, t_f is the corresponding time-of-flight, and p is the momentum of the particle. The most intense peaks observed in the mass spectra correspond to pions and protons for negative and positive polarities of the beam-line, respectively, for all the momentum settings measured. Electrons, positrons, charged pions of both signs, kaons, protons, and deuterons have been observed in the time-of-flight spectra. Muons can be distinguished from pions only for the lowest $B\rho$ settings due to the time-of-flight resolution. In the following, we discuss the results obtained for different primary beams and beam-line polarities.

Results of measurements for a proton primary beam and positive polarity of the beam-line

Proton primary beams of 1.6 GeV and 3.5 GeV incident energy impinged on the production target with the beam-line set to transport positive particles. For the 3.5 GeV primary beam, data were taken for central momenta of the beam-line between 1 GeV and 2.5 GeV. For the 3.5 GeV primary beam, the relative intensity of pions, protons, and positrons for different central momenta and different beam energies are given in Table 3.2. Positrons could be identified only at $p_0 = 1$ GeV/c.

Proj.	E GeV	p_0 GeV/c	e^+ %	π^+ %	K %	p %	d+^{4}He %	^3H %	^3He %
p	3.5	1.0	1.9	44.7	$4 \cdot 10^{-2}$	50.3	1.3	$5 \cdot 10^{-3}$	$5 \cdot 10^{-2}$
		1.5	-	42.8	$5 \cdot 10^{-2}$	54.0	1.2	$3 \cdot 10^{-2}$	$2 \cdot 10^{-2}$
		2.0	-	13.7	$6 \cdot 10^{-2}$	82.8	1.3	$3 \cdot 10^{-2}$	-
		2.5	-	4.20	$2 \cdot 10^{-2}$	90.9	1.0	$2 \cdot 10^{-2}$	-

Table 3.2: Relative abundance of particles measured in the target detector for various central momenta of the positive polarity beam. Dashes (-) indicate that the corresponding particles could not be observed or resolved with the available statistics.

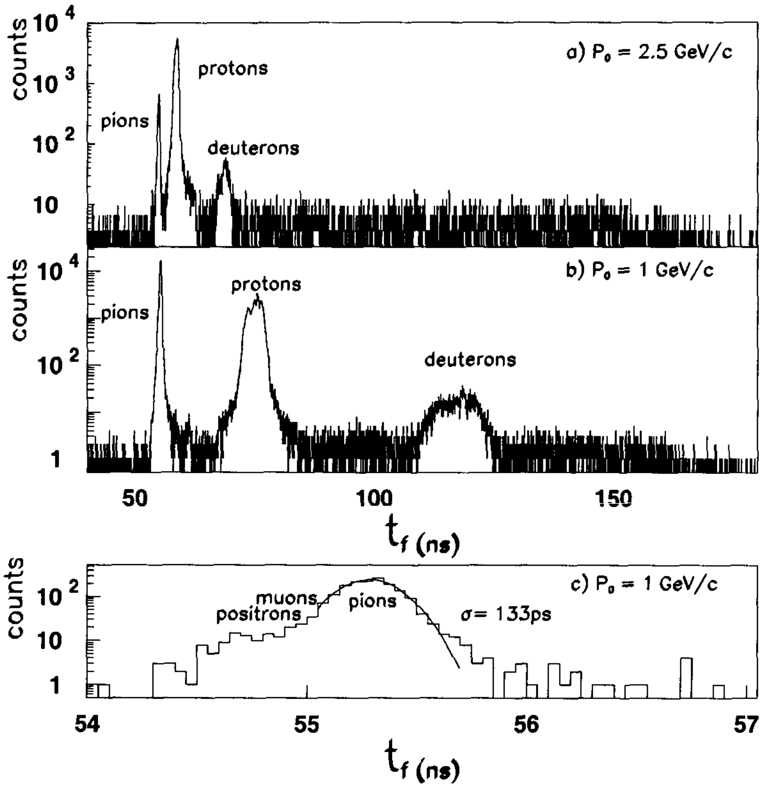

Figure 3.5: Time-of-flight spectra for p at 3.5 GeV primary beam and for central momentum of the beam-line of 1 GeV/c and 2.5 GeV/c and for positive polarity. Picture c) shows a zoom of the pion peak for the 1 GeV/c case and for events hitting the rod 8 in the three hodoscopes. Positrons appear as a shoulder to the left of the pion peak.

In Fig. 3.5, time-of-flight spectra are shown for a proton primary beam at 3.5 GeV and for central momentum of the beam-line of 1 GeV/c and 2.5 GeV/c, respectively. Peaks corresponding to pions, protons and deuterons are clearly seen. In the lower part of Fig. 3.5 the pion peak is displayed on a magnified scale showing a flat tail on the left side generated by positrons.

In Fig. 3.6, the mass spectra, calculated through Eq. 3.2 for the corresponding time-of-flight spectra of Fig. 3.5, are shown. At 1 GeV/c, apart from pions, protons, and deuterons two peaks corresponding to kaons and ^3He emerge.

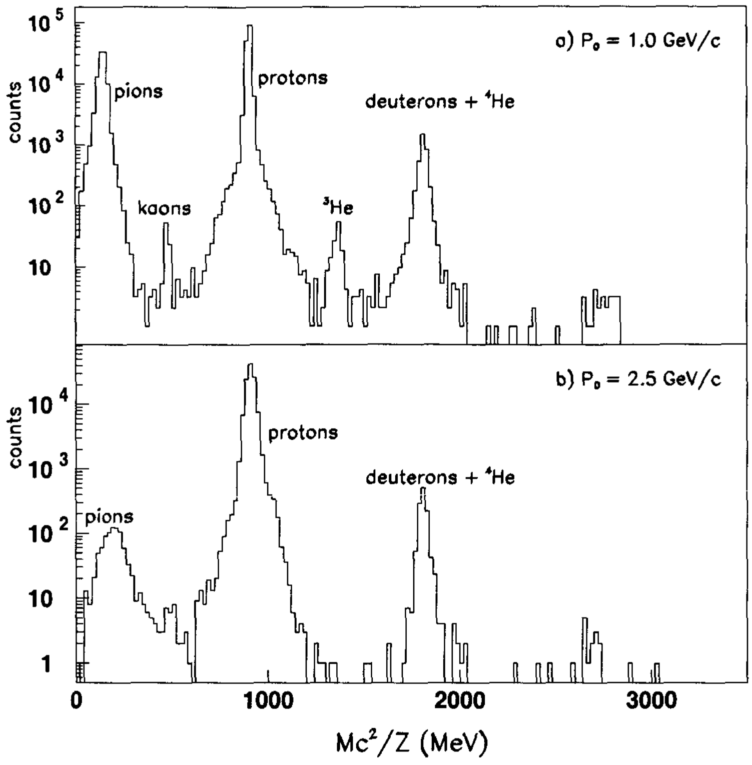

Figure 3.6: Mass spectra of positive charged particles for the 3.5 GeV p primary beam and for central momenta of the beam-line of 1 GeV/c and 2.5 GeV/c.

Results of measurements for negative polarity of the beam-line

When the beam-line is set to negative polarity, electrons, muons, and negative pions are transported up to the HADES target position. Measurements were performed for primary proton beams of 1.6 and 3.5 GeV and for primary carbon beams of 1.7, and 2.0 AGeV. The central momentum was varied between 0.4 GeV/c and 2.8 GeV/c. Muons could not be separated from pions. The relative intensities of electrons and negative pions are given in Table 3.3 for proton and ^{12}C primary beams.

In Fig. 3.7, the time-of-flight spectra of particles produced by a 2 A GeV ^{12}C and a 3.5 GeV proton primary beam are compared in the case of central momentum of the beam-line of 1 GeV/c. In Fig. 3.8, the time-of-flight sepa-

Proj.	E (AGeV)	P_0 (GeV/c)	e^-(%)	π^-(%)
p	3.5	0.6	31.2	65.4
		1.0	12.4	87.0
^{12}C	1.7	0.4	29.5	62.0
		0.6	8.5	88.6
		0.8	4.5	92.5
		1.0	1.1	96.0
	2.0	0.6	9.8	85.1
		0.8	5.1	93.6
		1.0	2.8	95.8

Table 3.3: Relative abundance of pions and electrons at the HADES target position for different primary beams and central momenta below or equal to 1 GeV/c, in the case of negative polarity of the beam-line.

ration of the electron and pion peaks is shown for a 3.5 GeV proton primary beam and for central momenta of the beam-line of 0.6 GeV/c, 1 GeV/c, and 1.3 GeV/c, respectively. The muon peak showing up at the momentum setting of 0.6 GeV/c is not visible when going to higher beam-line momenta. The time-of-flight spectra for 3.5 GeV proton and 1.7 and 2 AGeV carbon primary beams are compared in Fig. 3.9 for a central momentum of the beam-line of 0.6 GeV/c.

3.1.5 Intensity of pions at the target position

The maximum achievable pion rate at the HADES target position is the main information to be extracted from this commissioning experiment. This experiment was carried out at intensities much lower than the highest possible which is determined by the space-charge limit of the SIS primary beam. To calculate the highest intensities we have measured the coincident events in the three hodoscopes as a function of the intensity of particles extracted from SIS. The extraction efficiency from SIS was measured before every run with the help of ionization chambers placed along the beam-line preceding the production target and it was always found to be between 73% and 75%. The focusing of the beam-line was optimized before the runs by performing a fine tuning of the currents in quadrupoles and steerers in order to get the maximum intensity in the target detector. The intensity of coincident pions in the three hodoscopes

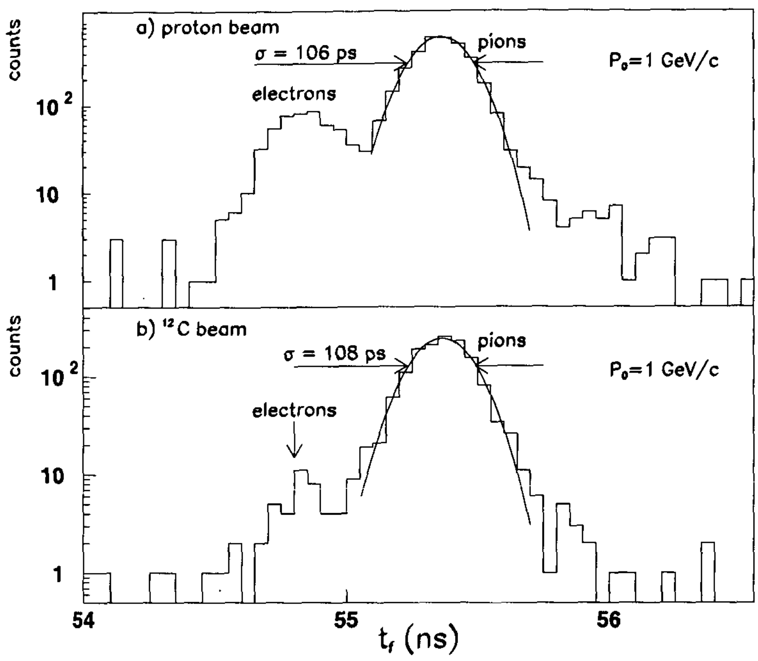

Figure 3.7: Time-of-flight spectra of secondary particles for proton at 3.5 GeV and ^{12}C at 2 AGeV primary beams and for 1 GeV/c central momentum of the beam-line, set to negative polarity. Each channel corresponds to 50 ps.

is given in Fig. 3.10 as a function of the central momentum of the beam-line, for p and ^{12}C primary beams of the maximum intensity that can be extracted from SIS. These intensities are 1.7×10^{11} and 5×10^{11} particles/spill for proton and carbon beams, respectively. For these data we have used the 10* cm length beryllium production target. It is observed that at low pion momenta the carbon beam produces higher pion intensities, at about 1.5 GeV/c the pion intensities are comparable and at the highest pion momenta proton beams are more effective.

The error bars are mainly due to uncertainties in the primary beam and in the magnets settings. The relative error is about 15% according to our estimates.

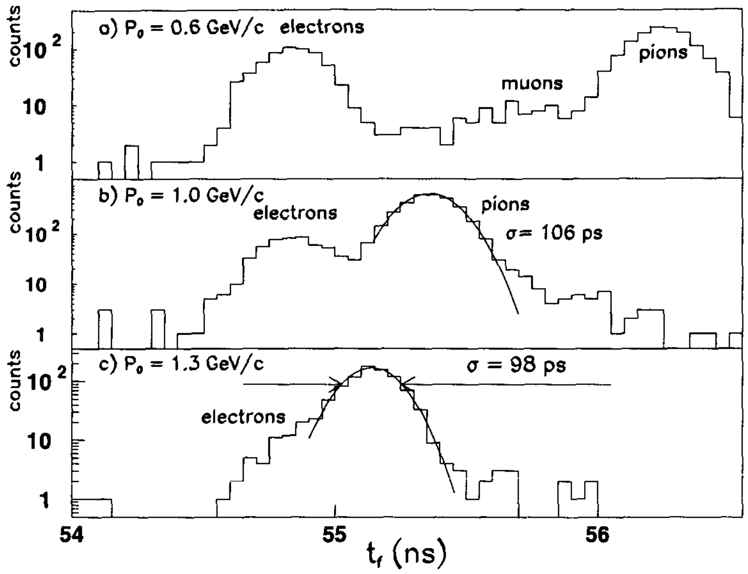

Figure 3.8: Time-of-flight spectra of secondary electrons and pions for the 3.5 GeV proton primary beam and for central momenta of the beam-line of 0.6, 1 and 1.3 GeV/c.

3.1.6 Intensity of electrons at the target position

The intensity of the electron component, extrapolated to the maximum intensity of SIS stated above, of the secondary beam is plotted in Fig. 3.11 for the different primary beams and for central momenta below or equal to 1 GeV/c, region where the electron identification is possible. The electron intensity is quite considerable in this region, which allows its use for detector tests and calibration purposes.

3.1.7 Pion intensity versus production target thickness

With the aim of determining the optimal design of the production target, the pion yield has been measured from the four available production targets at the time of the commissioning: beryllium targets of thicknesses 1.9, 3.9, 5.9 and 18.5 g/cm^2. The pion intensity should have a maximum for the optimal

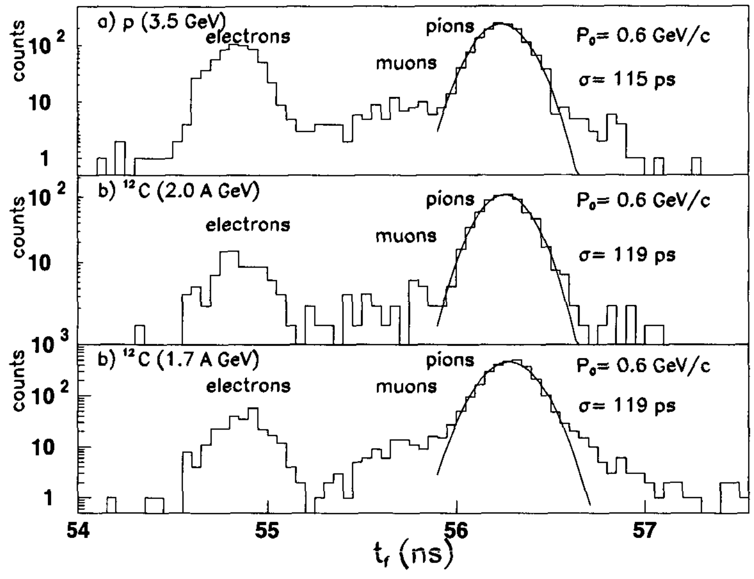

Figure 3.9: Time-of-flight spectra of secondary electrons and pions for p at 3.5 GeV and ^{12}C of 1.7 and 2 GeV primary beams for 0.6 GeV/c central momentum of the beam-line.

target thickness and decrease for thicker targets due to the domination of pion absorption over pion production. The pion intensity is plotted versus the production target thickness in Fig. 3.12 for primary beams of 1.7 and 2 AGeV ^{12}C and 1.6 and 3.5 GeV protons. Although the pion intensity error is about 15%, the error in the relative intensities for a run with different targets with the same conditions of primary beam and momentum selection is smaller than 10%. In Fig. 3.12 we can observe that pion intensity increases with the target thickness and it looks like if saturation was not reached. However, this target study is not very conclusive due to the small number of targets available. In the C beam-line a higher number of targets have been used and a more detailed study has been done.

3.2 Experiments in the C beam-line

In this section, we describe the results of the experiments performed in the C beam-line with different characteristics of projectile, primary beam energy,

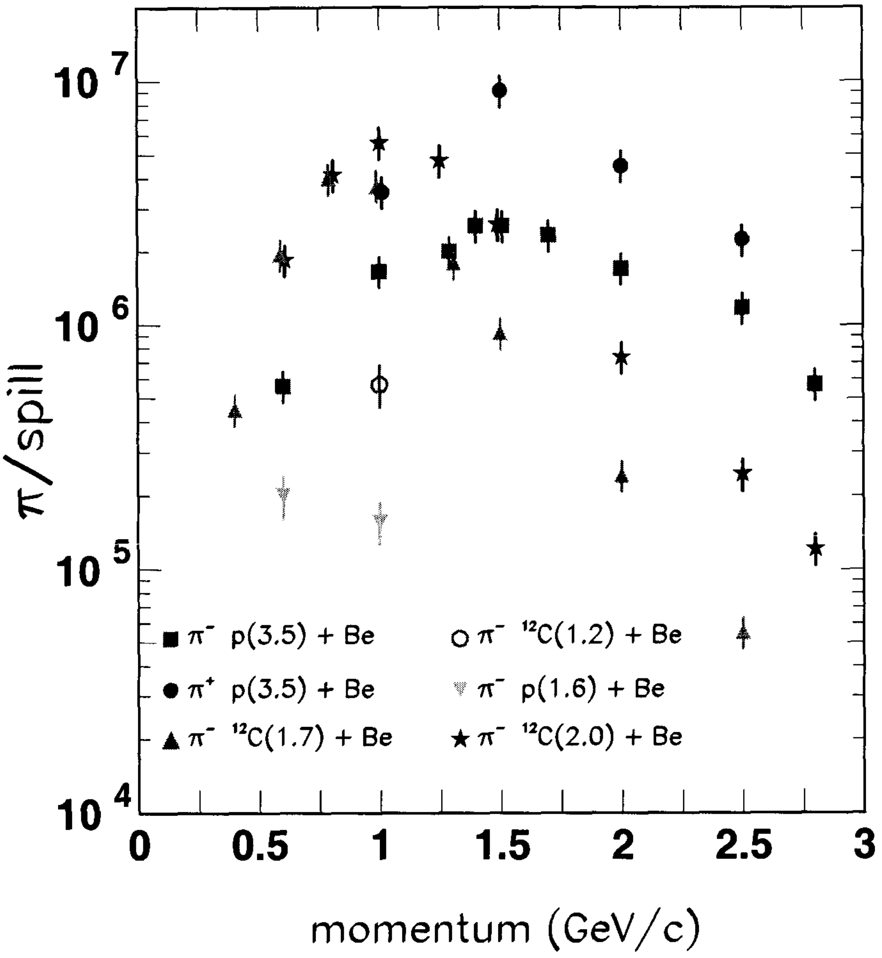

Figure 3.10: Pion intensity in the target detector for p and ^{12}C primary beams at different energies as a function of the central momentum of the beam-line. The primary beam intensities correspond to the maximum intensity to be extracted from SIS, i. e. 5×10^{11} protons/spill and 1.7×10^{11} Carbon ions/spill, respectively. The pion production target was the 10* cm length beryllium.

polarity and production target as summarized in Table 3.4.

As in the HADES beam-line experiment, we look in first place at the performance of the beam-line. In second place, we study the particle discrimination and the particle ratios of the beam. Finally, we show the intensity of pions

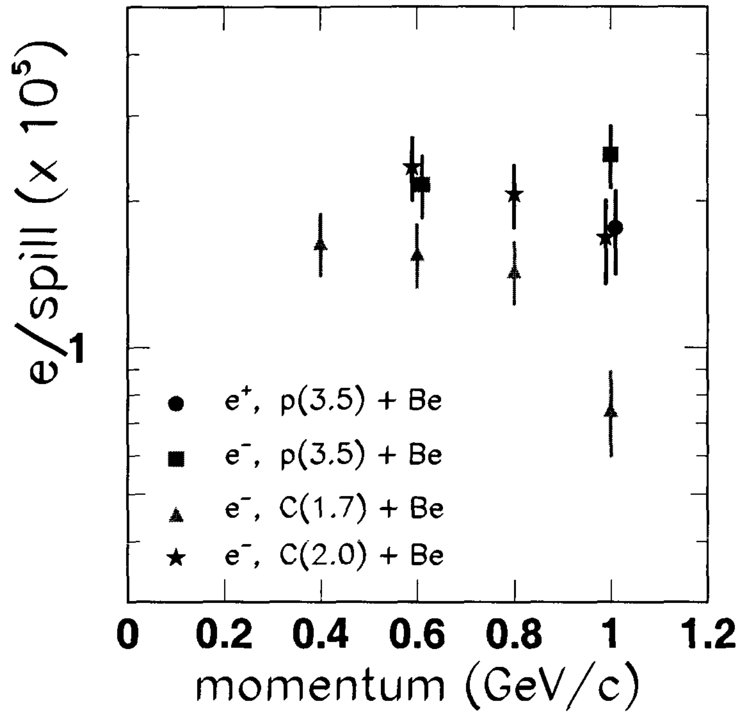

Figure 3.11: Intensity of electrons in the target detector for p and ^{12}C primary beams at the different measured energies as a function of the central momentum of the beam-line. The production target was the 10* cm length beryllium.

Proj.	E (AGeV)	Target (lengths in cm)	Polarity
^{12}C	1.3	Be(1, 2.1, 3.2, 8, 10), B_4C(8, 10, 12)	+
	1.5	Be(1, 2.1, 3.2, 8, 10), B_4C(8, 10, 12), Ti(12)	+, -
	2.0	"	-
^{14}N	2.0	"	-
p	4.7	"	+, -

Table 3.4: Characteristics of projectile, primary beam energy, production targets, and polarities in the experiments performed in the C beam-line

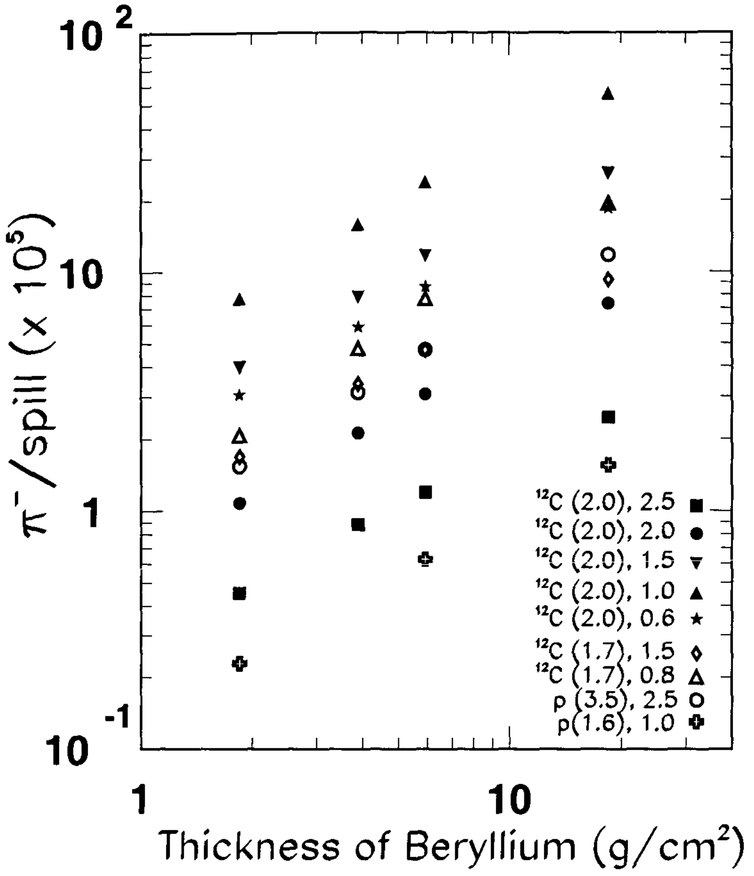

Figure 3.12: Pion intensity in the HADES beam-line versus production target thickness for different projectiles, primary beam energies and central momenta.

and electrons as a function of the momentum, primary beam, target thickness and material in the beam-line.

3.2.1 Performance of the beam-line

The performance of the optical elements in the C beam-line is much more sensitive to possible innacuracies than in the HADES beam-line. This is due to the longer total path and the higher number of elements involved, as shown in Fig. 2.1. In the first experiments in the C beam-line we had some difficulties to achieve a good setting of all the optical elements. In addition to the sensitivity mentioned before, we had to face the problem of remanent magnetic fields in some magnets that had to be switched off. These remanent fields resulted in a degradation of the beam. In order to solve this problem, we have used a special procedure of switching off the magnets in a degaussian way, which is based in reducing the current of the magnets very slowly and changing the polarity several times.

After setting the optical elements, we could get the secondary beam through. The beam in this beam-line is not so intense as it is in the HADES one because the longer path results in a lower acceptance of the beam-line, a higher decay probability and a larger multiple scattering attenuation, which is confirmed by the results of simulations in sections 4.2.3 and 4.2.4.

The set of plastic scintillators in this beam-line was not so sophisticated nor so precise as in the HADES one, i. e., we did not use segmented hodoscopes with high time resolution. However, they were good enough for the purposes they were thought of. They gave us the total intensities at some important positions, like the nominal positions of hodoscopes 2 and 3. These intensities were very helpful for the setting, monitoring and understanding of the beam-line. We obtained a time of flight resolution around 300 ps, which was enough to separate pions from protons and heavier particles. As we have here a longer path than in the HADES cave, we were also able to discriminate electrons at low momentum (below 1.0 GeV/c), and in that sense, to check the electron discrimination provided by the system of the Cherenkov detector and the Lead glass calorimeter. This system has a high detection efficiency, greater than 90% for all momenta. The XY ionization chambers served to record the beam profile, as it can be seen in Fig. 3.13, and to control the focusing at the end of the beam-line.

3.2.2 Particle discrimination and particle ratios

The combination of different detectors allowed us to discriminate the different kind of particles in the secondary beam. The time of flight between the different scintillators served to discriminate pions from heavier particles as seen in Fig. 3.14, whereas the energy signal of the scintillators was used to discriminate nuclear fragments at positive polarity. The combination of the lead glass calorimeter and the Cherenkov detector was used to discriminate electrons. The goodness of the discrimination is shown in Fig. 3.15. With this situation the only particles which could not be separate were muons from pions. However, muons come mainly from pion decay, and the contribution can be estimated from simulations as explained in section 4.2.4.

The particle composition of the secondary beam in cave C for negative and

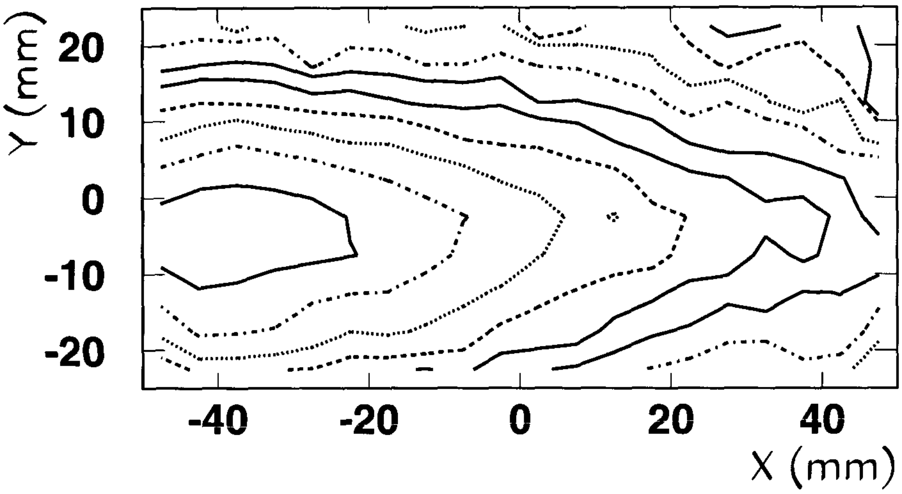

Figure 3.13: Beam profile in cave C from the XY1 ionization chamber. Each successive level of contour corresponds to an intensity decrease by a factor $e^{-1/2}$. This beam profile has been obtained during the TRD-ALICE prototype tests using negative pions with a central momentum of the beam-line of 2.5 GeV/c and the S_1-S_2 coincidence as trigger.

positive polarity for different production settings are given in Tables 3.5, 3.6 and 3.7.

3.2.3 Effect of the material in the beam-line

The intensity of the secondary beam depends strongly on the amount of material placed along the beam-line. However, it is necessary to place detectors in the beam-line for the experiments in order to have a good momentum resolution and to discriminate between the different kind of particles. In this section we study the attenuation of the pion beam produced by material in the beam-line, which is an essential aspect that have to be considered in order to optimize the secondary beam.

The attenuation of the pion beam produced by the presence of detectors is mainly due to multiple scattering according to our simulations presented in

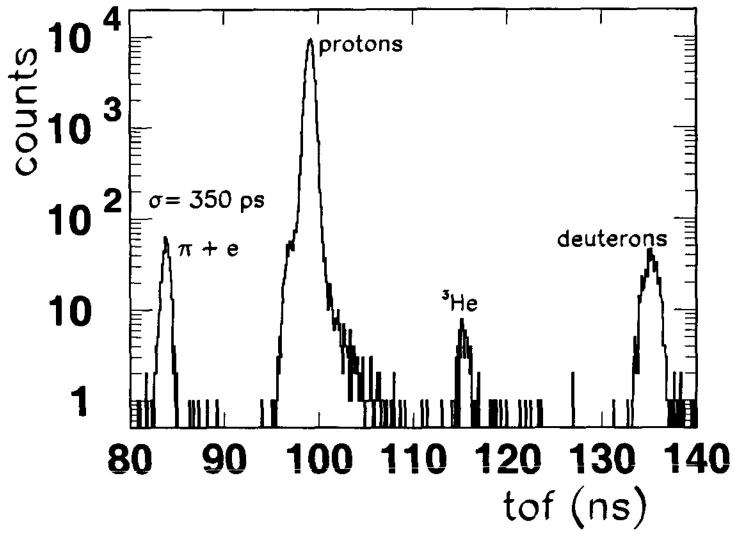

Figure 3.14: Time-of-flight spectrum between H_3 and S_2 for 1.4 GeV/c central momentum of the beam-line and positive polarity with 1.5 AGeV ^{12}C primary beam. The distance between the scintillators was 22.9 m.

section 4.2.4. This intensity attenuation depend not only on the quantity of material, but also on its position. This is easy to understand following the next reasoning: multiple scattering changes the direction of the particles and, therefore, it changes the probability that they are accepted by the beam-line. These small deviations in the direction of particles have a different effect which importance depends on the presence of optical elements near the point where they take place and on the distance of this point to the target in the cave. In order to have a better understanding of this effect, which will help for the design of future experiments, we have measured the attenuation produced by the scintillators H_3 and H_2. The insertion of these detectors is remote controlled, which allowed us to perform fast measurements with them in and out of the beam-line. The description of the detectors has been done in chapter 2. In Fig. 3.16 the attenuation factor for negative polarity due to the presence of these scintillators is given as the ratio of beam intensity with and without detectors. We have estimated this ratio as the ratio of S_1-S_2 coincidences with and without the detector(s) in the beam-line. We observe that the attenuation depends strongly on the central momentum selected, being extremely impor-

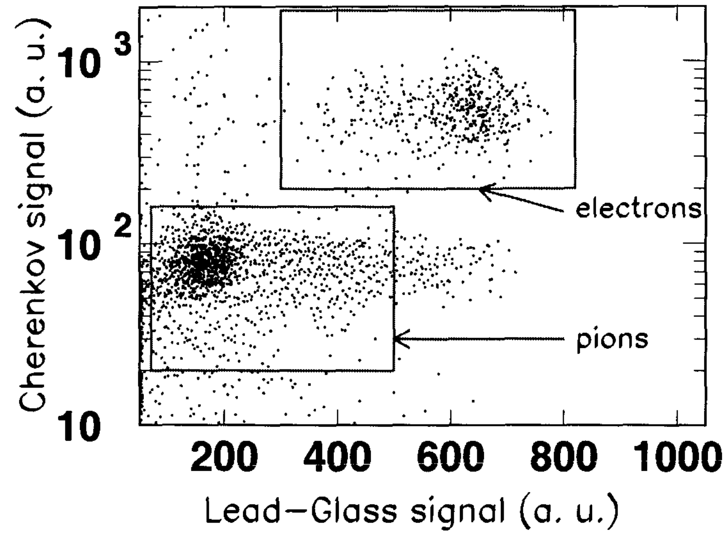

Figure 3.15: Cherenkov signal versus lead glass signal for 2 GeV/c central momentum and negative polarity of the beam-line. The zones corresponding to pions and electrons are well separated.

tant for low momenta and never negligible even for the highest momenta. The shape of the curves is in accordance with the simulations presented in section 4.2.4, which predict that the main cause of attenuation is multiple scattering. This effect depends on the velocity of the particle. It is larger when it travels slower, i. e., for the same central momentum this effect is larger for protons than for pions. Around 1 GeV/c the effect is quite similar for pions and electrons. For example, if we select 1.0 GeV/c central momentum and introduce the scintillator H_3 the attenuation factor of transmission for protons is 0.37, while for π^+ is 0.50 and for e^+ is 0.48.

3.2.4 Pion intensity versus production target thickness

Going on with the purpose of determining the optimal design of the production target, the pion yield in cave C has been measured for all the available production targets of different thicknesses, i. e., for the 1.9, 3.9, 5.9, 14.7 and 18.5 g/cm^2 beryllium targets, for the 19.8, 24.8, 29.8 g/cm^2 B_4C targets and for the 54.1 titanium target. To have a better knowledge of the target thickness

Proj.	E (AGeV)	Target (length in cm)	p_0 (GeV/c)	π^- %	e^- %
^{12}C	1.5	Be (10)	0.4	32	68
			0.6	77	23
			1.0	98.2	1.8
			1.4	98.7	1.3
^{12}C	1.5	B_4C (12)	1.0	97.1	2.9
^{12}C	1.5	Ti (12)	1.0	96.6	3.4
^{12}C	2.0	Be(10)	0.5	49	51
			0.75	83	17
			1.0	94.5	5.5
			1.4	97.8	2.2
			2.0	98.6	1.4
			2.5	99.4	0.6
^{12}C	2.0	B_4C (12)	0.5	39	61
			0.75	74	26
			1.0	91.4	8.6
			1.4	96.3	3.7
			2.0	98.0	2.0
^{12}C	2.0	Ti(12)	1.0	91.2	8.8
p	4.7	Be(10)	0.7	42	58
			1.0	66	34
			1.5	86	14
			2.0	93.2	6.8
			2.5	95.9	4.1

Table 3.5: Particle ratios at the target position of the C cave for negative polarity using carbon primary beams at 1.5 and 2.0 AGeV with different production targets and protons at 4.7 GeV with the 10 cm length beryllium target.

dependence than the one obtained in the HADES beam-line study, we have increased the number of targets with the intermediate 14.7 g/cm^2 Be target and we have gone further in thickness with heavier targets. The pion intensity is plotted versus the production target thickness in Fig. 3.17 for different primary beams, polarities and central momenta. Here, as in the HADES case, the main errors are due to primary beam intensity uncertainties and to the

Proj.	E (AGeV)	Target (length in cm)	p_0 (GeV/c)	π^- %	e^- %
^{14}N	2.0	Be(10)	0.6	67	33
			0.75	84	15
			0.9	93.1	6.9
			1.0	95.5	4.5
			1.1	96.7	3.3
			1.2	97.5	2.5
			1.35	98.1	1.9
			1.5	98.2	1.8
			1.75	98.7	1.3
			2.0	98.9	1.1
			2.25	99.2	0.8
			2.5	99.4	0.6
^{14}N	2.0	B_4C(12)	0.3	16	84
			0.45	30	70
			0.6	56	44
			0.75	78	22
			0.9	89	11
			1.0	92.6	7.4
			1.1	94.4	5.6
			1.2	95.7	4.3
			1.35	96.8	3.2
			1.5	97.2	2.8
			1.75	97.8	2.2
			2.0	98.3	1.7
			2.25	98.8	1.2
			2.5	99.2	0.8
			3.0	99.7	0.3
^{14}N	2.0	Ti(12)	0.6	53	47
			0.9	90	10
			1.5	97.7	2.3
			2.25	99.2	0.8

Table 3.6: Particle ratios at the target position of cave C for negative polarity when ^{14}N projectiles at 2.0 AGeV impinge on different production targets of the beam-line.

Proj.	E (AGeV)	Target (cm)	p_0 (GeV/c)	π^+ %	e^+ %	p %	^2H %	^3He %
^{12}C	1.3	Be(10)	0.5	45	31	23	-	-
			0.75	23	1.1	76	-	-
			1.0	3.9	0.04	96	0.3	-
			1.25	0.5	0.004	98	1.0	-
^{12}C	1.3	B_4C(12)	1.0	3.4	0.08	96	0.4	-
^{12}C	1.5	Be(10)	0.4	22	78	-	-	-
			0.6	31	10	59	-	-
			1.0	6.5	0.13	93	0.2	-
			1.4	0.47	0.006	97.5	1.8	0.2
			1.8*	0.03	-	99.0	0.5	0.1
			2.1*	-	-	99.7	0.15	0.04
			2.4*	-	-	99.3	0.4	0.3
			3.0*	-	-	7	-	93
^{12}C	1.5	B_4C(12)	1.0	8.5	0.2	91	0.3	-
^{12}C	1.5	Ti(12)	1.0	2.4	0.1	97	0.5	-
p	4.7	Be(10)	0.7	29	33	37	-	-
			0.9	31	15	54	-	-
			1.0	33	11	57	-	-
			1.1	34	7.5	59	0.13	-
			1.5	39	2.6	59	0.82	-
			2.0	35	1.0	63	0.87	-
			2.5	14.3	0.36	85	0.95	-
p	4.7	B_4C(12)	1.0	28	15	57	-	-
p	4.7	Ti(12)	1.0	29	16	55	-	-

Table 3.7: Particle ratios in the C cave for positive polarity and for different projectiles, primary beam energies and production targets of the C beam-line.

---

* These measurements were taken with an air gap of 3 meters at the hodoscope 2 position. So, the material in the beam-line was different and they cannot be directly compared to the rest of data with the same accuracy. However, we have decided to present these data because they give a good idea of what the situation is when using 1.5 AGeV carbon primary beam and selecting a high central momentum.

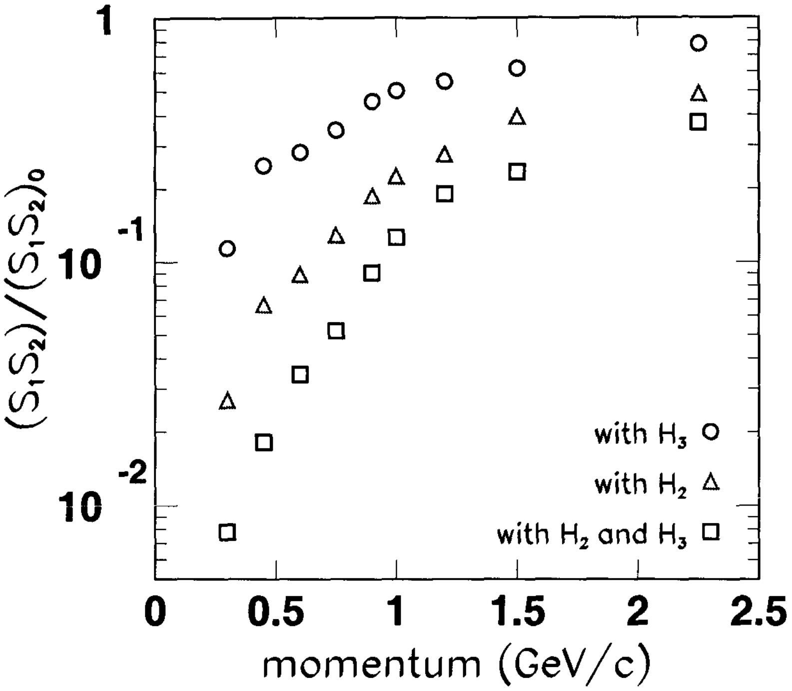

Figure 3.16: Attenuation factor at the C cave target when we introduce in the beam-line H_3, H_2 and both detectors, measured as the ratio of S_1-S_2 coincidences with and without the detectors in the beam-line. The measurements have been done with negative polarity and using ^{14}N (2.0 AGeV) as primary beam.

magnet settings. Our estimate of the relative error is about 15-20%.

We obtain as a general trend that there is a flat maximum between 15 and 30 g/cm^2 for all the carbon and nitrogen data at different momenta.

3.2.5 Electron intensity versus production target thickness

For the electron case, a target study similar to the one done for pions is summarized in Fig. 3.18. Here, an increase in the electron intensity is observed up to 30 g/cm^2, showing that thicker targets than in the case of pions are required to get the maximum intensity possible.

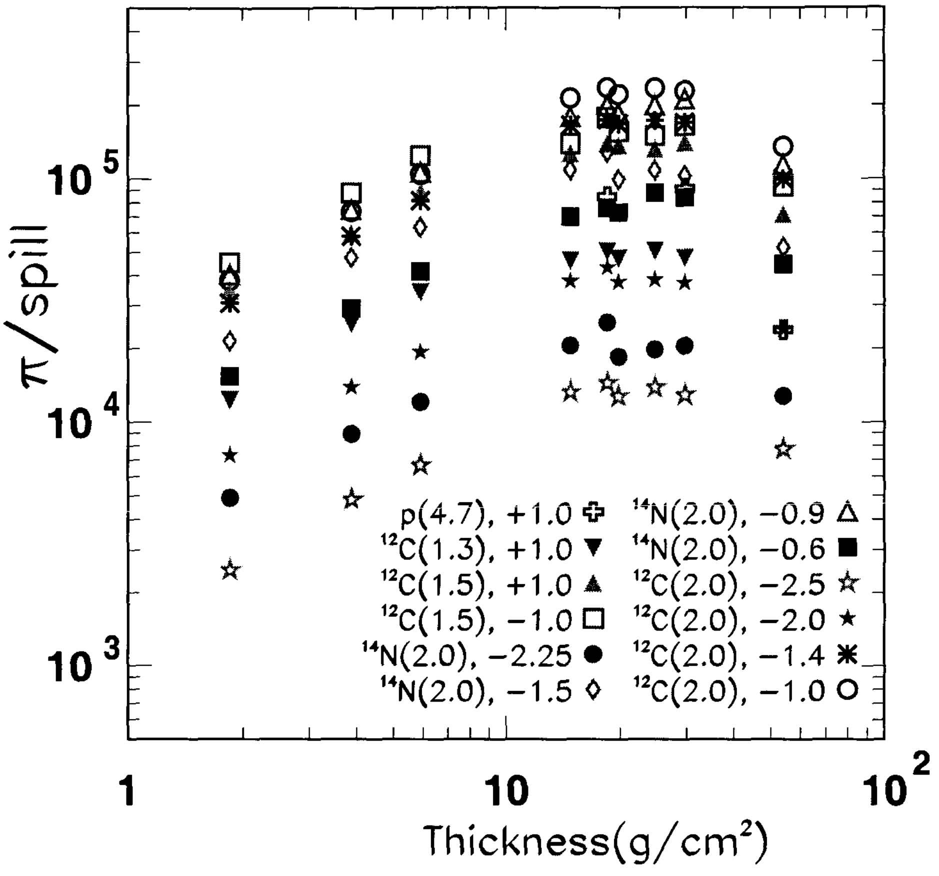

Figure 3.17: Pion intensity in the C beam-line target versus production target thickness for different projectiles, polarities, beam energies and central momenta.

3.2.6 Intensity of pions at the KaoS target position

The way in which the pion intensities in the KaoS target have been measured is the same as in the HADES target. The only difference is that in this case we are able to discriminate even at the highest momenta the electron component. The intensity of pions at the cave C target is given in Fig. 3.19 as a function of the central momentum of the beam-line, for the 12 cm length B_4C and the 10

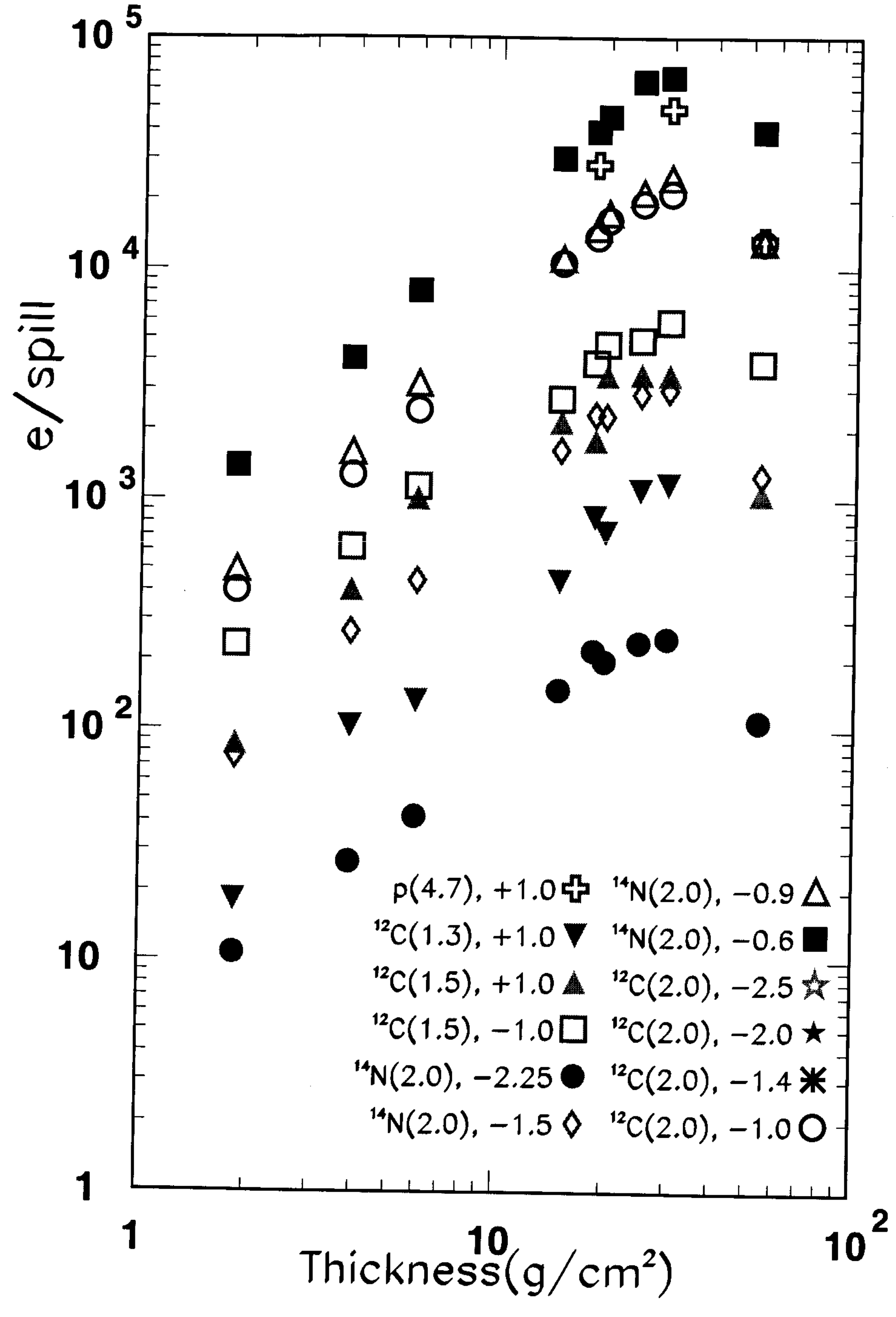

Figure 3.18: Electron intensity in the C beam-line target versus production target thickness.

cm length Be production targets and for proton[1], ^{12}C and ^{14}N primary beams of the maximum intensity that can be extracted from SIS. These intensities are 5×10^{11}, 1.7×10^{11} and 1.4×10^{11} particles/spill for proton, carbon and nitrogen beams, respectively.

It is observed that protons at 4.7 GeV are more efficient for producing high momentum pions whereas for low momentum pions a better yield is reached using ^{12}C or ^{14}N primary beams.

3.2.7 Intensity of electrons at the KaoS target position

The intensity of electrons, extrapolated to the maximum intensity of SIS is plotted in Fig. 3.20 for different primary beams over the whole momentum range. Here, it is also observed that proton beams are more favourable to produce high energetic particles, even more than in the pion case. Proton beam is the best choice when a secondary electron beam with momentum higher than 1 GeV/c is required. The electron intensity measured is an important result, because it will be sufficient for detector tests and calibration purposes. In fact, it is already being used for the tests of the TRD-ALICE [And01].

3.2.8 Intensity of secondary protons

The available data of secondary proton intensity as a function of the momentum for the 10 cm length beryllium target are shown in Fig. 3.21. The proton yields using a carbon primary beam at different kinetic energies, 1.3 and 1.5 AGeV, are compared. The proton intensities produced by a proton primary beam of 3.5 GeV and 4.7 GeV in caves HADES and C, respectively, are also shown.

---

[1] The proton data were measured in a position located 15 m upstream of the C target (see Fig. 2.4).

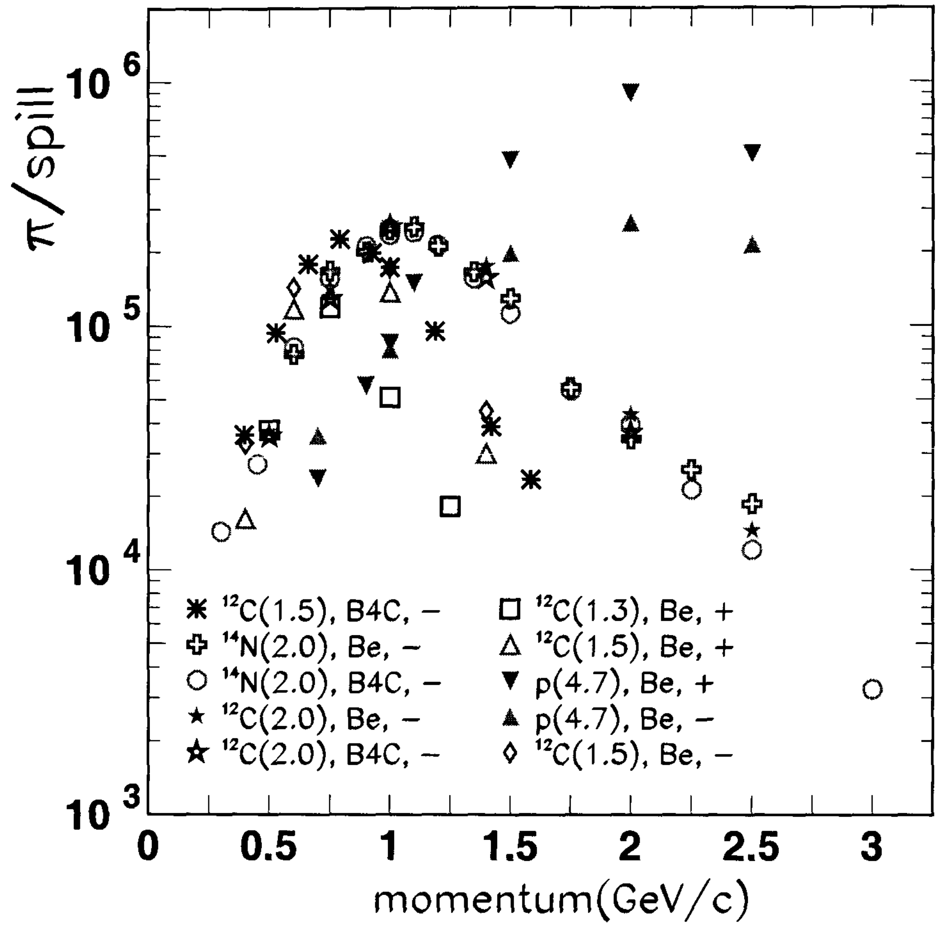

Figure 3.19: Pion intensity in the KaoS target detector for p, ^{12}C and ^{14}N primary beams at different energies as a function of the central momentum of the beam-line. The primary beam intensities correspond to the maximum intensity to be extracted from SIS, i. e., 5.0×10^{11} protons/spill and 1.7×10^{11} ^{12}C/spill, 1.4×10^{11} ^{14}N ions/spill , respectively. The data plotted correspond to the 12 cm length B$_4$C target and the 10 cm length Be target. The sign following the target symbol indicates the polarity of the beam-line.

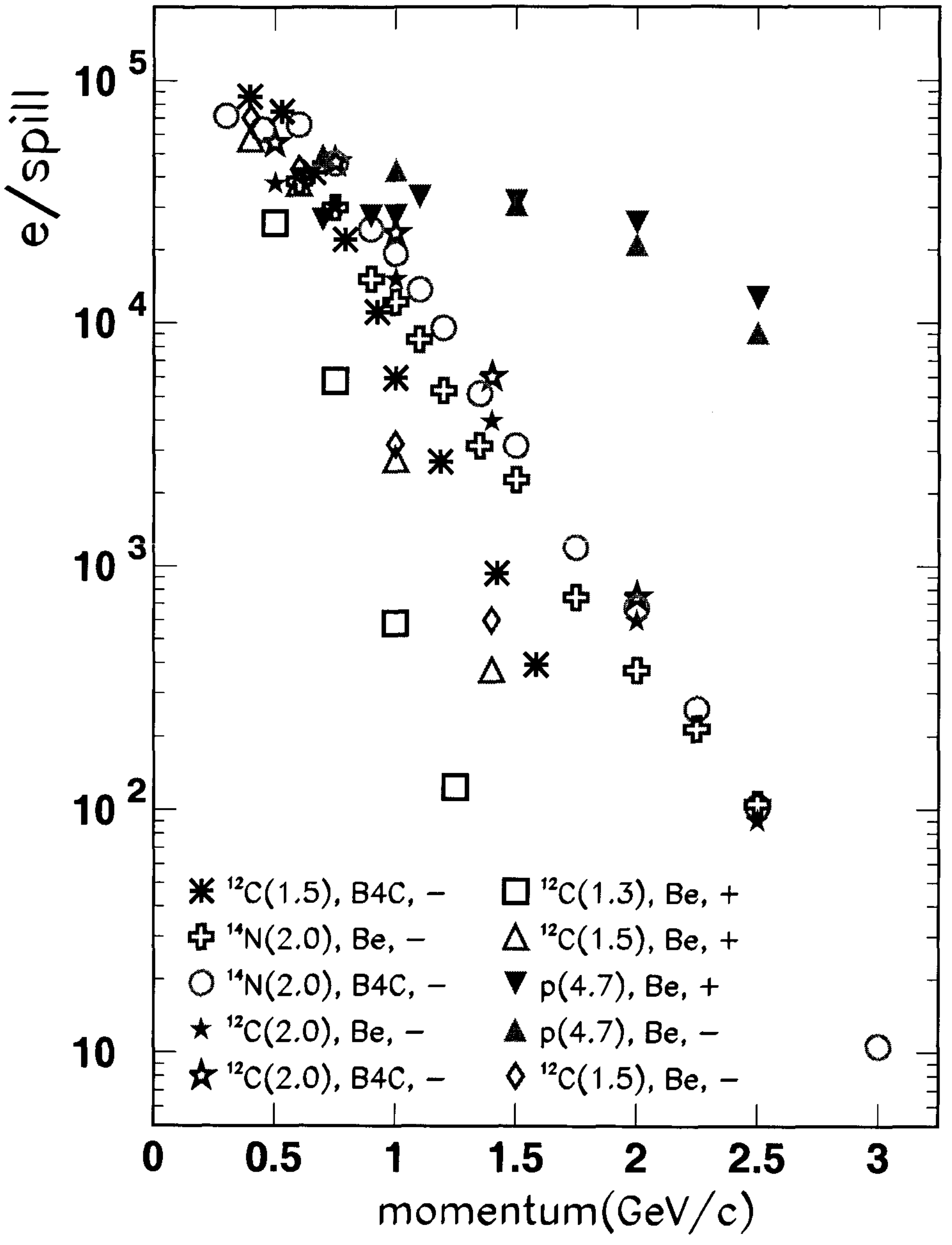

Figure 3.20: Intensity of electrons in the target detector for the 12 cm length B_4C and the 10 cm length Be production targets for p, ^{12}C and ^{14}N primary beams at different indicated energies as a function of the central momentum of the beam-line. The sign following the target symbol indicates the polarity of the beam-line.

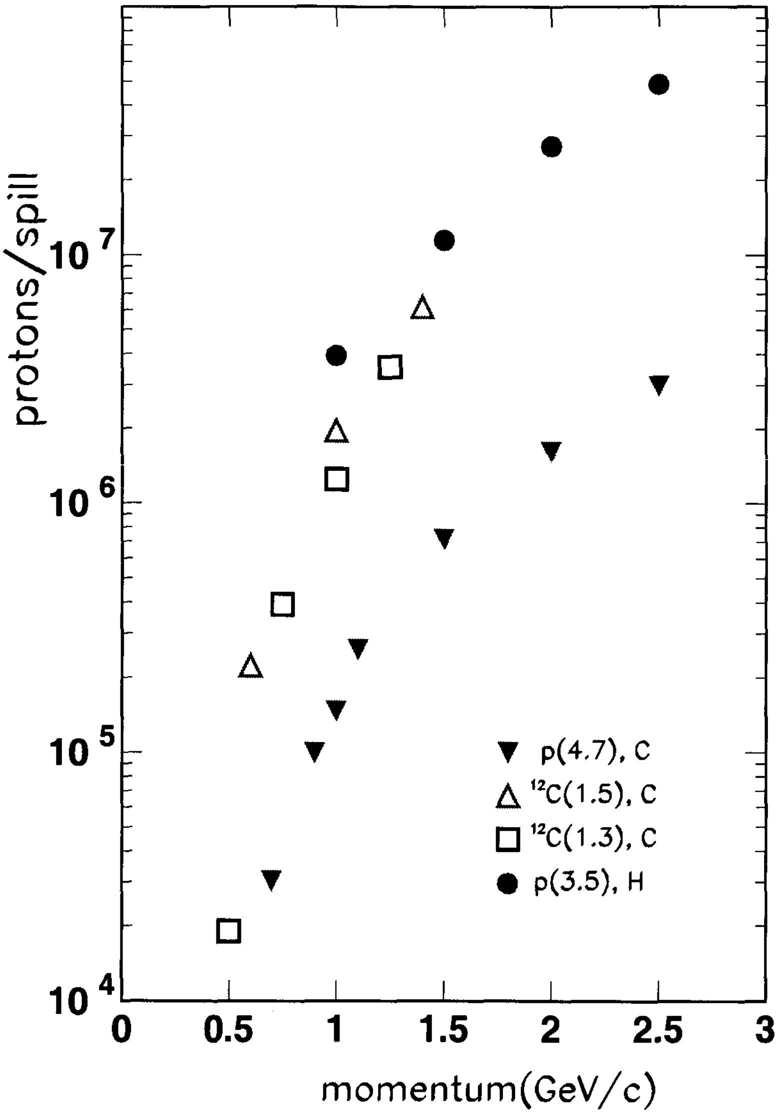

Figure 3.21: Intensity of protons in the caves C and HADES for the 10 cm length Be production target using 3.5 and 4.7 GeV proton and 1.3 and 1.5 AGeV ^{12}C primary beams as a function of the central momentum of the beam-line.

Chapter 4

Production target and beam-line simulations

In this chapter, we describe the simulations of production and transport of the pion beam in the C and HADES beam-lines. There are some previous investigations regarding the HADES beam-line. M. Alvarez [Álv98] studied this beam-line, mostly the aspect related to the transport of pions. In his work, attenuation of pion intensity due to their decay in flight, to multiple scattering and hadronic interaction in the diagnostic detectors were studied. Simulations of the hodoscope response were done in order to predict their performance during the measurements of time of flight resolution, particle identification of the secondaries and their momentum reconstruction. In addition, O.N. Hartmann [Har99] simulated the momentum reconstruction and studied the properties of the focus of the pion beam at the HADES target point.

Here, we present further studies concerning the transport of particles along both HADES and C beam-lines. We also present the results of a study of pion and electron production with several primary beams and production targets, performed in order to find out the optimal conditions in which the maximum pion and electron yields are obtained. In our simulations, we have used the GEANT code, version 3.21 [Bru94], which includes several packages to simulate the relevant physical interactions. In first place, we develop models to describe a heavy ion projectile impinging on a production target and the consequent pion and electron production. In second place, we consider the transport of pions in the HADES and C beam-lines, in particular, the acceptance of the beam-lines, the decay in flight of pions and the corresponding muon contamination of the secondary beam (very important because muons cannot be resolved from pions). We study, as well, the attenuation of the beam intensity due to multiple scattering and hadronic interactions. Finally, we present predictions of pion and electron intensities transported until the end of the beam-line. These computer simulated results can be directly compared to the experimental data presented in chapter 3.

GEANT3 allows the complete simulation of the setup of a typical high energy physics experiment and it is able to track the particles taking into account all the relevant physical processes. This allows us to study and predict the pion production and transport in the secondary pion beam at GSI in a reliable way. It also allows to study each interaction separately by switching off all the others. In this way, it is possible to focus on a given interaction in order to estimate its relative importance.

The code GEANT has the following characteristics:

- It can simulate projectile-target collisions. GEANT contains packages for the interactions involved in particle production and transport. GEANT allows to do the tracking of a proton primary beam along the production target to simulate the collision and the secondary particles produced according to one of the three different models of hadronic interactions included in the code, FLUKA [Aar87], GHEISA [Fes85] or GCALOR [Zei94], respectively, and to track secondary particles along the whole beam-line.

- It is faster than other more sophisticated codes available, which is really essential in our case due to the large amount of simulations required to study the different aspects of the beam-line.

- It is able to perform accurate simulations of the interaction of particles with detectors and magnetic elements and of secondary particle transport by electromagnetic fields.

GEANT3, however, has also serious drawbacks. While proton-nucleus cross-sections are included in the code, it does not treat neither nucleus-nucleus collisions nor the interaction of the resulting nuclear fragments. This is, certainly, an important aspect in our study, so we have to provide a solution. One possibility is to implement a better hadronic interaction package in GEANT, and in fact, there are some people working along this line in the new version GEANT4 [Ago02]. But considering our severely restricted time scale, we have decided to follow a different approach to treat the nucleus-nucleus collisions. We have preferred to use two simple models for this purpose, which are described in sections 4.1.1 and 4.1.2 respectively.

4.1 Simulations of the production target

In this section we study particle production by simulating the collision of the primary beam with the production target and transporting the secondary pions produced in forward direction up to the end of the production target. Electron production is taken into account by means of the $\pi^0 \rightarrow \gamma\gamma$ process followed by gamma-ray conversion into e^+e^- pairs.

There are several sophisticated models available for pion production cross-sections, as seen in section 1.1.4. But it would be difficult to include them in GEANT3, and moreover the resulting code would be too slow for our needs. For this reason we have preferred to use the FLUKA and GCALOR packages, which are already included in GEANT.

4.1.1 Pion and electron production from a Maxwell-Boltzmann distribution model

Our first model of pion production consists in generating pions directly from a Maxwell-Boltzmann distribution fitted to the experimental data as we have described in chapter 1. Therefore, the pion energy distribution will be given by Eq. 1.3. The emission of pions in the nucleon-nucleon center of mass is not isotropic. It has been experimentally observed that there is a higher probability of emission in the forward-backward direction [Bro84]. To be in agreement with this fact, angular distributions are modelled by Eq. 1.2. Due to the lack of experimental data about the asymmetry parameter a for the pion angular distributions of the system C+Be at 2 AGeV, we have generated the pions according to an angular distribution with the average a value obtained from the measurements of the system Ar+Kr at 1.8 AGeV ($a = 1.03$) [Tei97]. This parameter depends on energy, as shown in the right part of Fig. 1.2. However, we work first with the average value, and finally we study the changes produced by the introduction of an energy dependent a parameter.

The particles are generated in a cylinder of a radius of 1 mm, which is assumed to be the effective beam radius, and a length of 10 cm, which is the length of the beryllium production target. The pion production rate is not uniform along the production target due to the attenuation and energy loss of the primary beam [Álv98]. On the other hand, the pion absorption in the production target is directly simulated by GEANT.

In GEANT we work in the laboratory system with the origin in the center of the production target. Therefore, we need to boost the momentum of the pions from the center of mass system to the laboratory system,

$$\begin{aligned} P_x^{lab} &= P_x^{cm} \\ P_y^{lab} &= P_y^{cm} \\ P_z^{lab} &= \gamma^{cm} \cdot (P_z^{cm} + \beta^{cm} \cdot E^{cm}), \end{aligned} \tag{4.1}$$

where $\beta^{cm} = 0.718$ and $\gamma^{cm} = 1.437$ for the N-N c.m. system at 2 AGeV. To complete the model, we need the multiplicity of pions produced by each colliding primary beam ion, which we denote by $\pi/^{12}C$. To estimate this quantity we have used the following assumptions:

- The pion multiplicity per participating nucleon, M_{π^0}, measured in C + C at 2 AGeV [Ave97], was found to be 0.15 approximately. As it is a symmetric isospin system, we assume the same value for M_{π^-}.
- The geometric model [Cug81], which gives the number of participating nucleons in the collision,

  $$A_{part} = \frac{A_p\, A_t^{2/3} + A_t\, A_p^{2/3}}{(A_p^{1/3} + A_t^{1/3})^2}, \tag{4.2}$$

  where A_p and A_t are the nuclear masses of projectile and target, respectively. For the $^{12}C +^9 Be$ system we have A_{part}=5.19.
- The $^{12}C +^9 Be$ reaction cross-section is given by the geometrical prescription:

  $$\sigma_{geo} = \pi \left[r_0 (A_p^{1/3} + A_t^{1/3}) \right]^2, \qquad r_0 = 1.2 fm. \tag{4.3}$$

  which gives a value of 863 mb corresponding to a macroscopic cross section $\Sigma = 0.107\ cm^{-1}$.

The length l of the beryllium target is 10 cm. The probability that a ^{12}C ion interacts in it is $1 - exp(-\Sigma l)$. Therefore, the number of pions produced per carbon ion can be estimated by

$$\pi/^{12}C = [1 - exp(-\Sigma l)] * M_{\pi^-} * A_{part} \approx 0.51. \tag{4.4}$$

We have assumed above that each ^{12}C ion suffers only one interaction which amounts to neglect second chance interactions and interactions produced by secondary nuclear fragments produced in collisions. Therefore, the multiplicity given by Eq. 4.4 should be lower than the real one. In order to get an estimation of the pion multiplicity error introduced by the previous assumption we consider the limit in which most of the products of the first chance collisions are able to interact again producing additional pions, that is, that there is no primary beam attenuation. This upper value for the pion multiplicity is given by

$$\pi/^{12}C = [\Sigma l] * M_{\pi^-} * A_{part} \approx 0.84. \tag{4.5}$$

It should be noticed that Eq. 4.4 and Eq. 4.5 are equivalent for $\Sigma l << 1$. In our case, $\Sigma l \approx 1$, the second expression could be more accurate due to the contribution to pion production by nuclear fragments. Certainly, this expression will not be valid for very thick targets satisfying $\Sigma l >> 1$. Eq. 4.4 and Eq. 4.5 are limit cases and it is reasonable to assume that the real multiplicity is somewhere in between. However, ought to the complexity of the problem of a ^{12}C ion impinging on a thick target, a better estimation is hard to obtain.

To verify the accuracy of this model for pion production cross-sections, we have compared the predicted pion production invariant cross-section at 0 degrees with experimental data [Moe83] in Fig. 4.1. In this figure, we show model predictions for four cases corresponding to two different temperatures for the pion energy distribution, T=80 MeV and T=100 MeV, and to two different energy dependences of the asymmetry parameter a, a constant and equal to the average value and a given by

$$a(E) = 2 \times \exp\left(-\left(\frac{[E - m_{\pi}] - 0.3}{0.2}\right)^2\right), \tag{4.6}$$

where E is the pion energy in center of mass and m_{π} is the pion rest mass. The latter is a rough parameterization of the experimentally extracted $a(E)$ seen in the right part of Fig. 1.2, which does not show a gaussian shape. However, this parameterization is simple and serves to get some feeling about the importance of the energy dependence of a in the description of the forward pion production distribution. Fig. 4.1 shows the relative importance of temperature and asymmetry in the predicted cross-sections. We can observe that T=80 MeV with the average a gives a good description of the shape but the absolute cross-section is clearly lower than the data. The introduction of $a(E)$ given by Eq. 4.6 only increases the cross-sections at low momenta and worsens the global shape. On the other hand, T=100 MeV with a constant gives a bad description of both magnitude and shape, but when the energy dependence is considered, both the shape and the magnitude of the pion energy distribution are quite well reproduced.

4.1.2 Hot gas model of the primary beam projectile

As heavy ion collisions cannot be simulated by GEANT, we have developed a model in which the primary beam heavy ion is considered as an ensemble of independent nucleons, in which correlations and collective effects are neglected. This model is certainly very limited, specially when we are trying to reproduce particle production beyond the kinematic nucleon-nucleon limit (which is indicated in Fig. 1.4). The simplest model is to take nucleons as non-interacting particles but in this case their momentum distribution is that of a Fermi gas, which has not enough high momentum component to reproduce the experimentally observed high energy pions. One phenomenological way in which high momentum tails can be included in the nucleon momentum distribution is to assume that the projectile is a hot Fermi gas. In the collision, the gas of nucleons is heated which introduces a high momentum component. A temperature slightly higher than the really reached in the collision can mock the high momentum component present in the momentum distribution of an interacting Fermi gas. Thus, the effective temperature used accounts for the real heating of the nucleons produced in the collision and for the neglected high momentum tails. In fact, in our phenomenological model we have used exponential distributions with an inverse slope parameter T instead of Fermi distributions because the former are easier to simulate and produce practically equivalent high energy tails. So, our method of simulation of a heavy ion projectile is to replace it by its nucleons and to assume that their energy follows an exponential distribution with inverse slope parameter T in the projectile reference system. Actually, the process of simulation of a heavy ion projectile impinging on a thick target is, step by step, the following. The interacting point of each nucleon of the impinging nucleus is sorted. Its energy at the interaction point is taken as the sum of the kinematical energy per nucleon of an impinging ion interacting at this point (incident energy corrected for energy loss) plus a Fermi energy sorted according to an exponential distribution of inverse slope T. The corresponding Fermi momentum is randomly sorted in the projectile system and boosted to the laboratory system where it is added to the incident momentum per nucleon at this point. The resulting energy and momentum are used to simulate the production of secondary particles, their energies and their momentum. The reason of introducing the Fermi momentum of the nucleon after calculating the interaction point is to assure that this Fermi momentum does not affect the trajectory of the incident nucleon in the

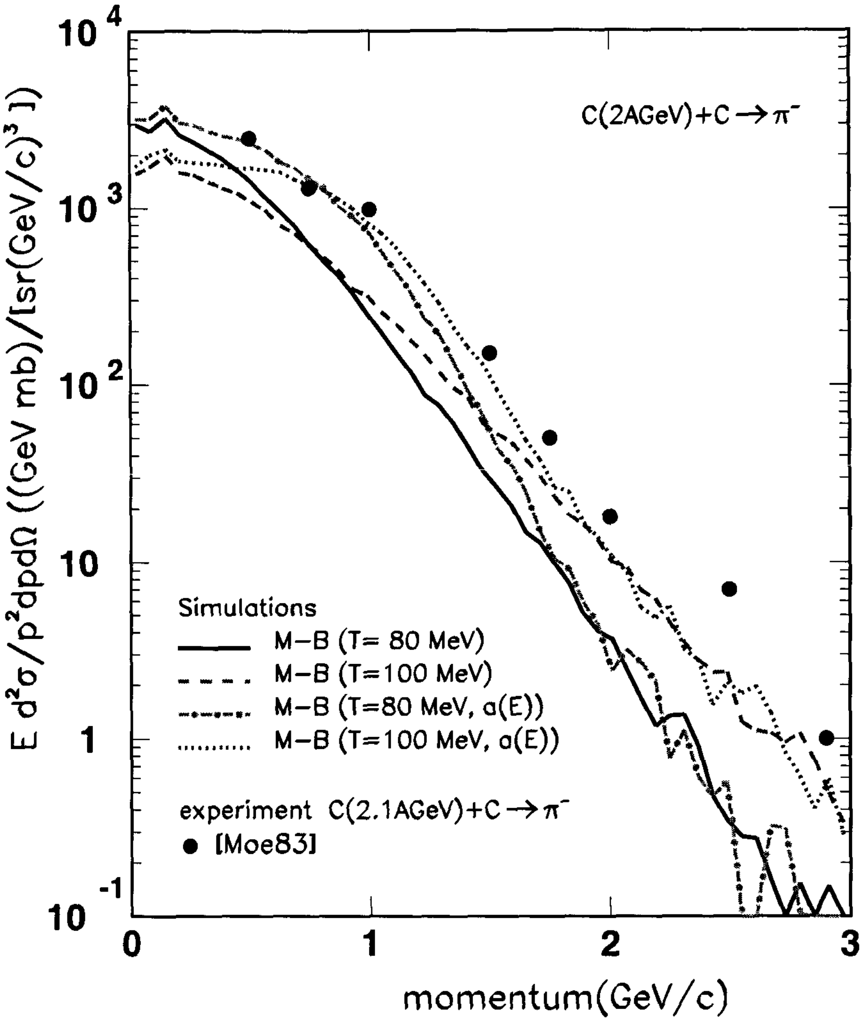

Figure 4.1: Calculated forward pion production invariant cross-sections as a function of the pion laboratory momentum in C+C collisions, as explained in the text. The results from a Maxwell-Boltzmann distributions with T=80 MeV or T=100 MeV and with and without energy dependence of the asymmetry parameter a are shown. The fluctuations at high momenta are statistical. The experimental data from [Moe83] are shown for comparison.

production target. Finally, GEANT3 does the tracking of the produced secondary particles until they are absorbed or they leave the target. In principle, all the nucleons of a given nucleus should have been forced to interact at the same point, but after a large number of simulated ions the effects produced by each nucleon interacting in a different point are averaged out.

We have tested the model for two different inverse slope parameters T of the nucleons, T=20 MeV and T=60 MeV. The reason behind this choice is the fact that experimental pion spectra show energy distributions which can be interpreted as a mixture of pions at two different temperatures, as already mentioned in chapter 1. The pions belonging to the lower and higher temperature ensembles are responsible of the low and high energy tails of the spectra, respectively. The relative weight of each temperature has been taken as 90 % for T=20 MeV and 10 % for T=60MeV. These weighs correspond to the observed relative yields of low momentum to high momentum pions. These parameters and weights are arbitrary to some extent. However, our motivation here is not to fit the data but to show the general trends of the simulations provided by this model. The pion production invariant cross-section in the forward direction obtained in this model for 2 AGeV ^{12}C impinging on a carbon target of 1 cm length is shown in Fig. 4.2. The simulated cross-sections correspond to pions arriving to the first quadrupole. These simulations are compared to the data of forward pion production for $^{12}C(2.1AGeV) + C \to \pi^-$ from [Moe83]. It can be seen that there is an overall agreement, specially with FLUKA, although the simulations are nearly a factor 2 lower than the data for momenta below 1 GeV/c. However, we have to stress that no parameter has been fitted. From these results we can conclude that the simulated intensities at the end of the beam-line are expected to underestimate the data by similar factors. Somewhat lower cross-sections in the whole momentum range are obtained by using GCALOR.

This model has the advantage of allowing us to simulate secondary particle production from the primary beam interaction with the production target. Once a model for primary beam and production target collisions is provided to GEANT, the whole simulations of particle production and transport from the production target to the end of the beam-line can be achieved without any additional ingredient. This model is very convenient for thick targets because in this case second chance interactions are accounted for in part and the momentum distribution of pions obtained by this model is more reliable than that from the model of section 4.1.1.

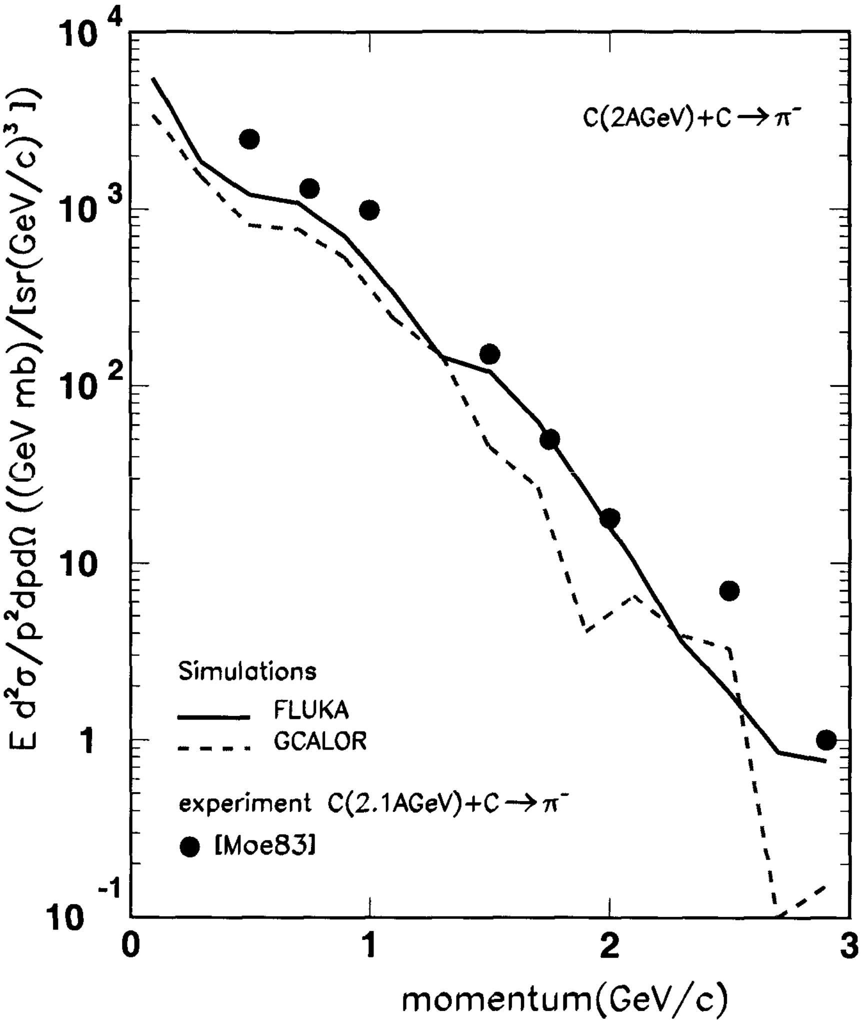

Figure 4.2: Calculated forward pion production invariant cross-section as a function of the pion laboratory momentum for C+C as explained in the text. The results obtained with the FLUKA and GCALOR hadronic packages are shown. The experimental data taken from [Moe83] are also plotted for comparison.

4.1.3 GEANT simulations of proton primary beams

Our model for proton primary beam is to generate by GEANT a beam of monoenergetic protons at the beginning of the production target. In this case all the uncertainties related to heavy ion dynamics are absent. Although with some limitations in accuracy this model can be useful for simulating not only secondary pions and electrons but also secondary protons and can be used to optimize the production target design.

In Fig. 4.3 we present the negative pion production cross-section of 3.5 GeV protons impinging on a carbon target obtained using the FLUKA and GCALOR hadronic packages. They are compared to the experimental data from [Pap75, Sug98]. The curves given by Maxwell-Boltzmann distributions with temperatures T=150 MeV and T=200 MeV are also shown. We can observe that both FLUKA and GCALOR data overestimate significantly the experimental data at around 1.4 GeV/c. At higher momenta the FLUKA predictions remain clearly above the experimental data and show a second peak whereas the GCALOR predictions fit better the experimental data. For lower momenta, simulations underpredict the experimental cross-section, specially in the GCALOR case. In the case of positive pion production a similar behaviour is observed. Going to higher primary beam energy, 4.7 GeV, the same behaviour is observed but the maximum of the cross-section is shifted to higher momenta, around 1.9 GeV/c.

This model has been applied for the optimization and design of production targets to be used with the recently available 4.7 GeV proton primary beam. This beam is more efficient in producing high energy pions than 2 AGeV heavy ion primary beams and will also be useful to provide high energy electrons to be used for calibration purposes. To optimize the target we have done simulations of 4.7 GeV protons impinging on different production targets of 14 cm total length made of one or two segments of carbon and copper. The momentum distributions of electrons and positrons transported up to the first quadrupole produced by several different targets are shown in Fig. 4.4. It can be observed in this figure that the target composed of a 11.5 cm carbon segment followed by a 3.5 cm copper segment is the most efficient in all the momentum range explored. The reason is that the carbon segment is efficient in producing neutral pions and the copper segment is the best for converting in e^+e^- pairs the γ-rays produced in the π^0 decay. A full carbon target produces less e^+e^- pairs because its lower γ conversion power while a full copper target will be less efficient because its higher absorption rate. The order of the segments is crucial because the pion producing segment has to be placed before the γ converting segment. It can be observed in Fig. 4.4 that among the two targets composed by 7 cm of copper and 7 cm of carbon, the one in which the carbon is placed first is the more efficient to produce electrons. We see that simulations help us in deciding the order and relative length of different

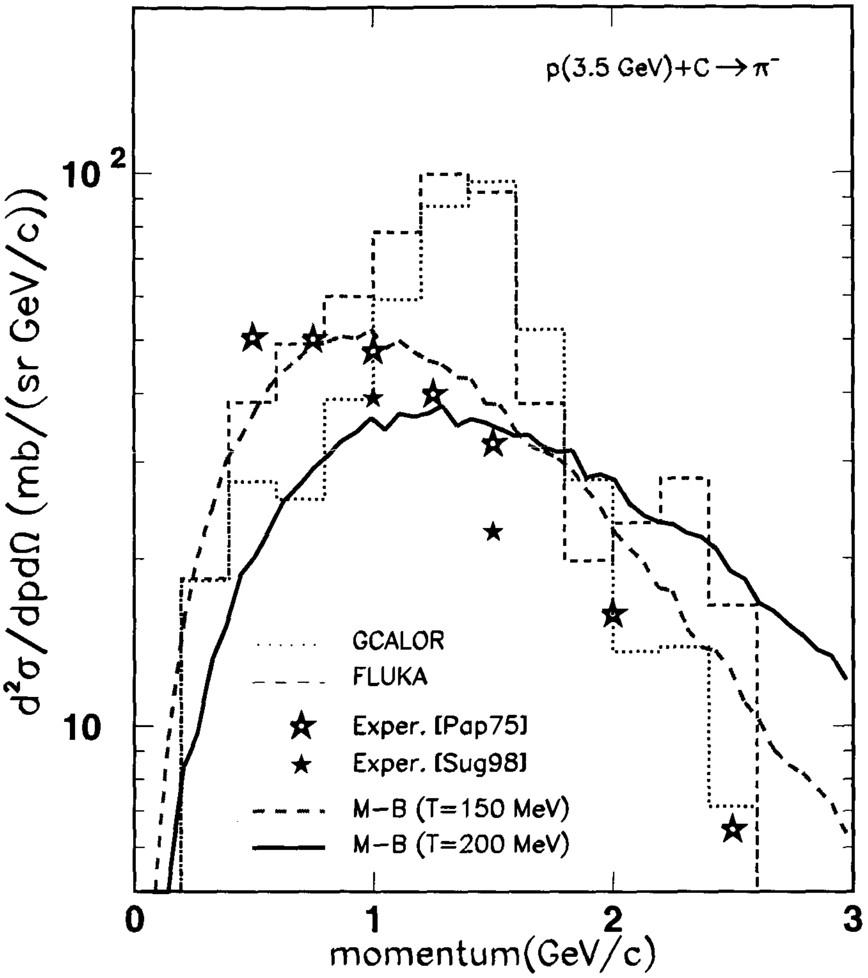

Figure 4.3: Calculated π^- production cross-section in the forward direction as a function of the pion laboratory momentum for p(3.5 GEV) + C from FLUKA and GCALOR simulations of protons impinging on a 1 cm long carbon target. The available experimental data [Pap75, Sug98] are plotted for comparison. The distributions obtained by generating pions according to a Maxwell-Boltzmann distribution of T=150 MeV and T=200 MeV, respectively, are also shown.

materials in composed targets and to translate into a quantitative base the initial guess that for producing e^+e^- pairs the best is to put behind a low atomic mass production target a short heavier target of about one radiation length thickness.

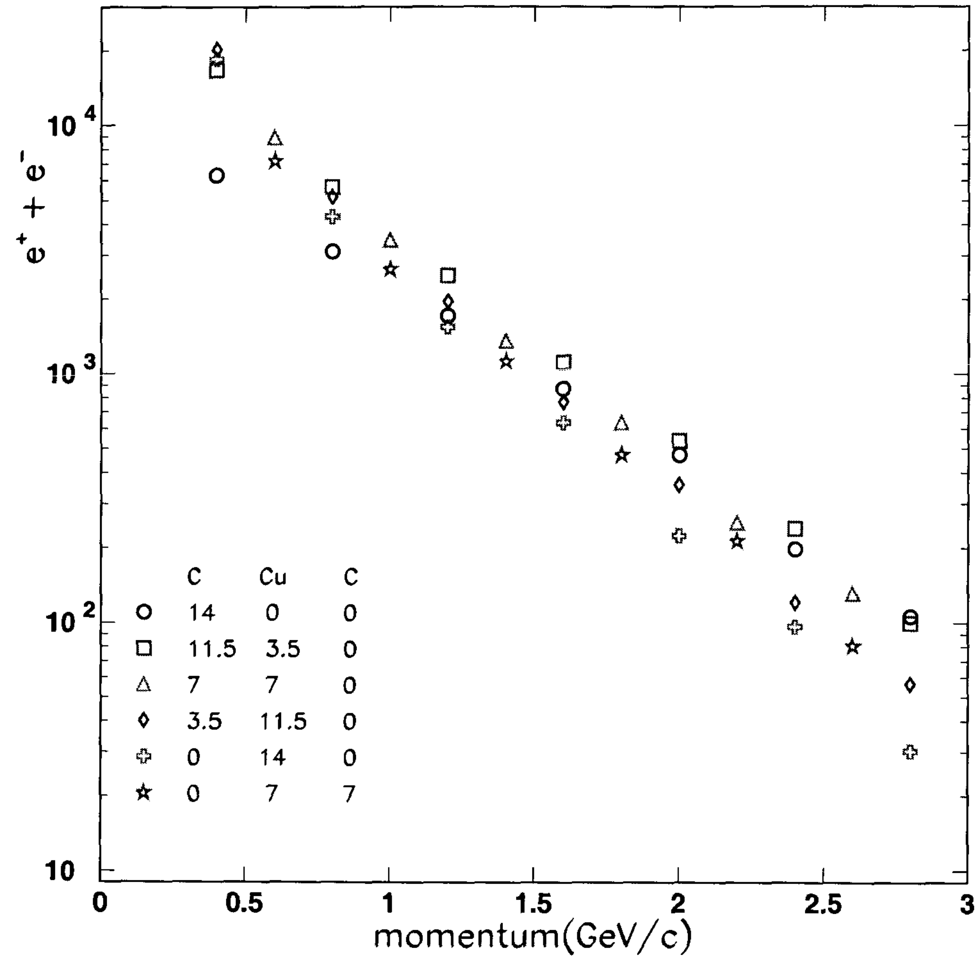

Figure 4.4: Simulated electron and positron distribution at the entrance of the first quadrupole for 4.7 GeV protons colliding on several copper and carbon composite targets of 14 cm total length. The simulations have been done using GEANT with FLUKA. A total number of 4×10^6 protons have been generated.

The result of a similar study for pions is plotted in Fig. 4.5. Although the intensities obtained with different targets show less marked differences than in the e^+e^- case it is still concluded that the best choice to produce pions at high momenta is a composite target. At low momenta, however, a full copper target is the best.

4.2 Simulations of pion transport in the beam-line

In this section we describe simulations of pion transport, acceptance of the beam-line and attenuation of the pion beam due to decay in flight and different interaction processes. As we are only concerned in this section with transport along the beam-line, we generate pions in the production target by a Maxwell-Boltzmann distribution with T=80 MeV which agrees with the experimental data as explained in section 4.1.1.

4.2.1 Coordinate system for the simulations

The kinematic variables of the particles transported in GEANT are always referred to the so-called Master Reference System (MARS). This system is implicitly defined as the local reference system of the first volume defined, which contains all the others. This is a cartesian coordinate system with axes $\widehat{x}$, $\widehat{y}$ and $\widehat{z}$, where $\widehat{z} = \widehat{x} \times \widehat{y}$. We take as the z-direction the beam direction, the x-direction as the horizontal direction, which is perpendicular to z axis, and the y-direction is the vertical direction, perpendicular to z and x.

The different elements of the setup and the geometry of the beam-lines are described in chapter 2. The position of the different elements of both beam-lines are given in Tables 2.2 and 2.3.

4.2.2 Simulation of the optical elements

Pions are transported along the beam-line with the help of magnetic quadrupoles and dipoles. The equation of motion of charged particles in a magnetic field is

$$\frac{d\vec{v}}{dt} = \frac{e}{m} \cdot \vec{v} \times \vec{B}, \tag{4.7}$$

where $m = m_0(1 - \beta^2)^{1/2}$. These equations are solved in GEANT by the Runge-Kutta method.

A magnetic dipole generates an homogeneous field B_0. The curvature radius of the trajectory of a particle with charge e and momentum P_0 moving in this field is given by the expression

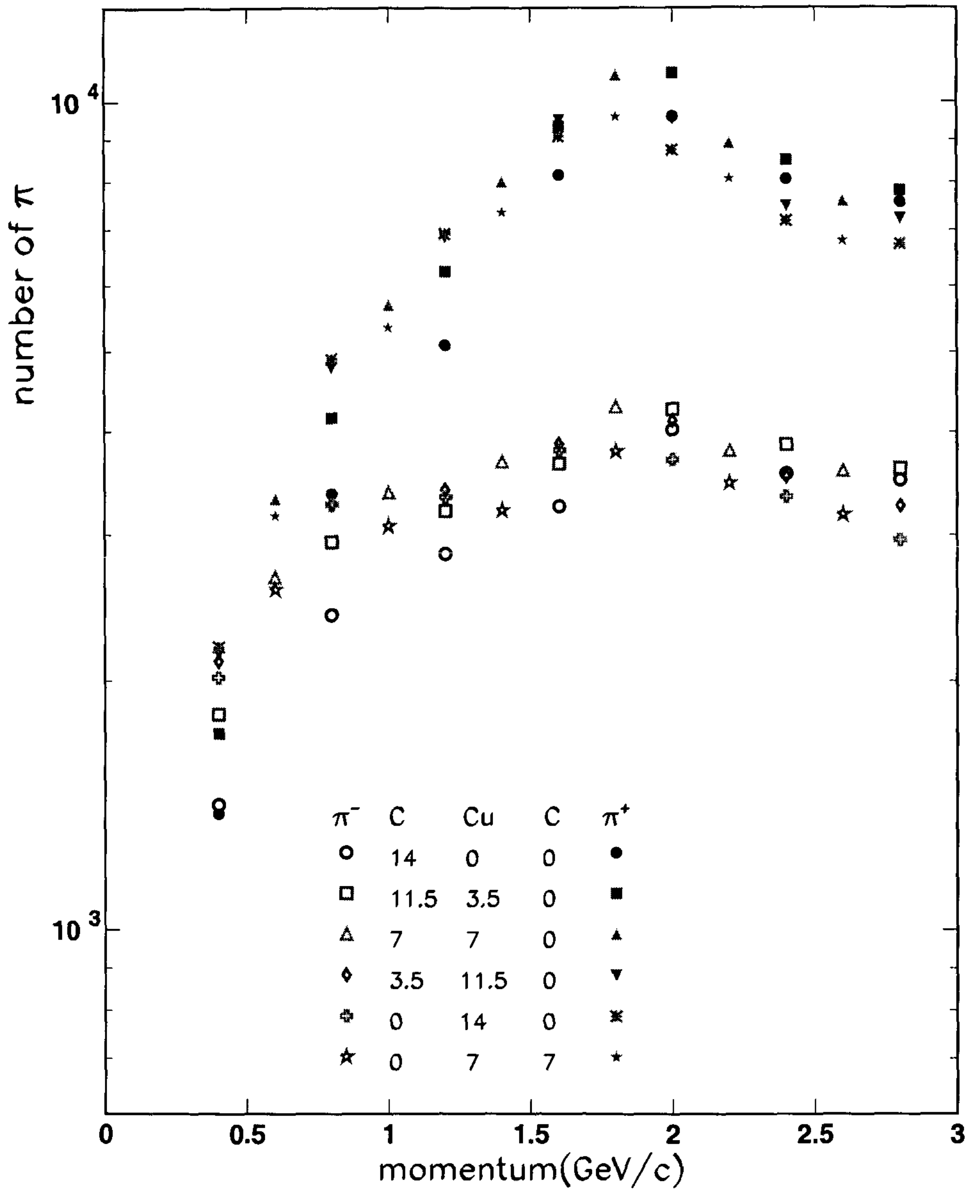

Figure 4.5: Simulated π^+ and π^- distribution at the entrance of the first quadrupole for 4.7 GeV protons colliding on several copper and carbon composite targets of 14 cm total length. The simulations have been done using GEANT with FLUKA. A total number of 4×10^6 protons have been generated.

$$\frac{1}{\rho}[m^{-1}] = \frac{e \cdot B_0}{P_0} = 0.2998 \frac{B_0[T]}{P_0[GeV/c]}. \tag{4.8}$$

On the other hand, a particle crossing a quadrupole experiences a magnetic field given by

$$\vec{B} = (G \cdot y, G \cdot x, 0), \tag{4.9}$$

where the constant G is called the gradient of the quadrupole. In analogy with the dipole magnet, it is convenient to introduce a momentum-independent quadrupole strength

$$k[m^{-2}] = \frac{e \cdot G}{P_0} = 0.2998 \frac{G[T/m]}{P_0[GeV/c]}. \tag{4.10}$$

The ρ values of the dipoles and the k values of the quadrupoles for both HADES and C beam-lines are given in Tables 2.2 and 2.3, respectively.

4.2.3 Calculations of the acceptance by simulations

The fraction of initial pions arriving to the beam-line target is called the acceptance. In our case it is small. The beam-line is designed in such a way that the particles with the highest probability of being accepted are those entering the beam-line at 0 degrees and with momentum P_0, the selected central momentum of the beam-line. However, pions coming out of the production target have momentum and angular distributions on which the acceptance depends strongly. Since this dependence is not well known and since the calculation of the acceptance from geometry considerations is very complex, we have calculated it for different ranges of momenta and angular directions by means of simulations.

In Fig. 4.6 the bidimensional acceptances for θ, φ and $\Delta p/p$ are plotted for both the C and HADES beam-lines. We see in the figure the different characteristics of the beam-lines. For instance, looking at φ we see that the HADES beam-line has higher acceptance in the Y-Z plane while it is very low in the X-Z plane. The hole of the acceptance in the X-Z plane is responsible of the reduced global acceptance of this beam-line. In the C beam-line, the φ distribution is wider. However, there is a clear asymmetry in the X-Z plane, the acceptance is much higher in the left (φ=180°) that in the right (φ=0) half plane. The $\Delta p/p$ dependence of the acceptance is also quite different in both beam-lines. The $\Delta p/p$ window for the C beam-line is very narrow, about

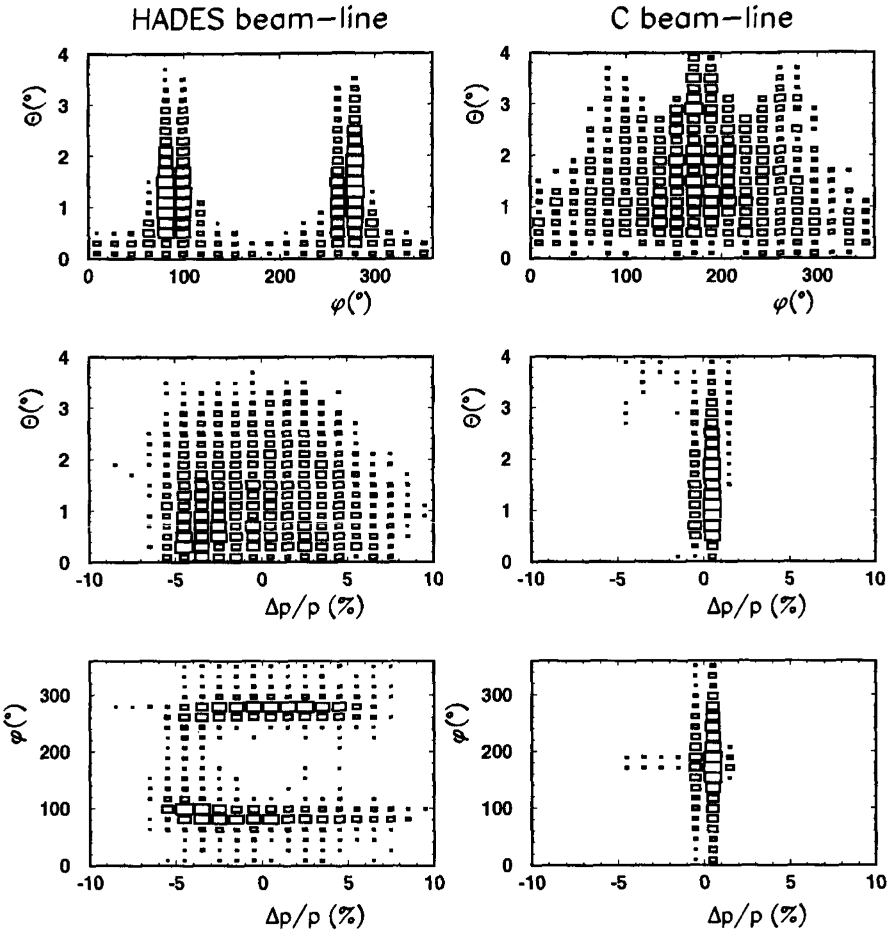

Figure 4.6: Acceptance of π^+ as a function of $\Delta p/p$, θ and φ for the HADES and C beam-lines and P_0 equal to 1 GeV/c.

1%. This is the main origin of the low global acceptance of the C beam-line. On the other hand, the $\Delta p/p$ acceptance of the HADES beam-line is wider, approximately 8%, which results in a higher global acceptance. The acceptance in θ for both beam-lines shows a wide distribution limited by the entrance radius of the first quadrupole. The acceptance depends on momentum only through the relative variable $\Delta p/p = (P - P_0)/P_0$, where P is the momentum of the particle and P_0 is the central momentum of the beam-line set by the magnetic dipoles. In Table 4.1 the ratio of pions that arrive at the HADES and KaoS targets to the pions generated by a Maxwell-Boltzmann distribution of T=80 MeV in the production target, for different $\Delta p/p$ and solid angle $\Delta\Omega$ windows, are reported.

4.2.4 Simulation of interactions

There are three interaction phenomena that attenuate the initial pion beam intensity: decay in flight, multiple scattering and hadronic interactions. In order to know the relative importance of each of these interactions, we compare simulations in which one of them is switched on to those in which it is switched off. The quantity used for comparison is the fraction of initial pions arriving to the HADES and C beam-line targets.

Decay in flight and muon to pion ratio

The number of pions that decay in flight can be, in principle, approximately calculated by the formula $exp(-Lm/(\tau P_0))$, where L is the length of the beam-line, m is the rest pion mass, τ is the pion mean life at rest and P_0 is the central momentum. However, simulations are necessary if we need high accuracy, because in that case we have to correct for the different trajectory lengths and for the time of flight corresponding to different $\Delta P/P_0$ values. A relevant information which can only be extracted by simulations is the content of muons in the pion beam at the cave target. In this case, an analytical calculation is quite involved because the acceptance of produced muons depends on their point of production, energy and momentum. Moreover, the experimental setup is unable to discriminate between muons and pions. Thus, simulations are the only way to know what is the fraction of muons in the pion beam, which has to be corrected for in order to calculate pion cross-sections. In Fig. 4.7 the muon to pion ratio at the targets of HADES and C caves as a function of the central momentum is shown. The pions have been generated according to a Maxwell-Boltzmann distribution with T=80 MeV in the momentum range $\Delta P/P_0 = 8\%$ and solid angle interval $\Delta\Omega = 2.5$ mrad. Increasing both, $\Delta P/P_0$ and $\Delta\Omega$, no significant variation is produced because the distance between the production target and the first quadrupole is small, as it can be seen in Table 2.3. So, the chance a muon is produced in a pion decay within the acceptance window of the first quadrupole is mall.

Although the muon to pion ratio could be expected to be higher in the C than in the HADES beam-line because the higher length of the former, our simulations show that the muon contents are similar in both beam-lines, or

$\Delta p/p(\%)$	$\Delta\Omega(msr)$	$\varepsilon_{H1}(\%)$	$\varepsilon_{H2}(\%)$	$\varepsilon_{C1}(\%)$	$\varepsilon_{C2}(\%)$
10.0	0.2	34 ± 3	54 ± 4	2.9 ± 0.4	7.0 ± 0.6
8.0	0.2	42 ± 3	65 ± 5	3.4 ± 0.4	8.4 ± 0.7
5.0	0.2	57 ± 5	81 ± 7	5.4 ± 0.7	13.1 ± 1.1
2.0	0.2	44 ± 7	77 ± 11	14.0 ± 1.8	34 ± 3
0.5	0.2	45 ± 15	80 ± 20	35 ± 6	81 ± 11
10.0	1.0	15.7 ± 0.8	26.2 ± 1.0	2.60 ± 0.14	5.9 ± 0.2
8.0	1.0	19.6 ± 1.0	32.9 ± 1.3	3.26 ± 0.19	7.4 ± 0.3
5.0	1.0	27.2 ± 1.5	42 ± 2	5.1 ± 0.3	11.5 ± 0.5
2.0	1.0	23 ± 2	39 ± 3	13.2 ± 0.8	29.9 ± 1.3
0.5	1.0	23 ± 4	36 ± 6	33 ± 3	76 ± 5
10.0	2.5	9.7 ± 0.4	16.3 ± 0.6	1.95 ± 0.08	4.41 ± 0.12
8.0	2.5	12.1 ± 0.5	20.3 ± 0.6	2.45 ± 0.10	5.53 ± 0.15
5.0	2.5	17.2 ± 0.7	26.7 ± 0.9	3.94 ± 0.17	8.9 ± 0.3
2.0	2.5	16.0 ± 1.1	25.7 ± 1.1	10.1 ± 0.4	22.9 ± 0.7
0.5	2.5	17 ± 2	25 ± 3	25.7 ± 1.5	59 ± 2
10.0	4.0	7.1 ± 0.3	12.1 ± 0.3	1.51 ± 0.06	3.36 ± 0.08
8.0	4.0	8.9 ± 0.3	15.1 ± 0.4	1.89 ± 0.07	4.22 ± 0.11
5.0	4.0	12.7 ± 0.5	20.1 ± 0.6	3.04 ± 0.11	6.77 ± 0.17
2.0	4.0	12.5 ± 0.7	19.9 ± 1.0	7.9 ± 0.3	17.5 ± 0.5
0.5	4.0	12.3 ± 1.5	18.9 ± 1.9	20.2 ± 1.0	46.3 ± 1.7
10.0	16.0	2.18 ± 0.07	3.63 ± 0.09	0.54 ± 0.02	1.18 ± 0.02
8.0	16.0	2.73 ± 0.09	4.55 ± 0.11	0.67 ± 0.02	1.48 ± 0.03
5.0	16.0	3.96 ± 0.13	6.17 ± 0.17	1.08 ± 0.03	2.37 ± 0.05
2.0	16.0	4.0 ± 0.2	6.2 ± 0.3	2.68 ± 0.08	5.83 ± 0.13
0.5	16.0	4.0 ± 0.4	6.1 ± 0.5	7.2 ± 0.3	15.4 ± 0.4

Table 4.1: Geometrical acceptance of HADES and C beam-lines for π^+ generated by a Maxwell-Boltzmann distribution of T=80 MeV and assuming different $\Delta p/p$ and $\Delta\Omega$ windows. ε_{H1} and ε_{H2} are the ratios between the number of π^+ that arrive to the HADES target (within a radius of 1.0 and 2.0 cm, respectively) and the generated number of π^+ in the production target. ε_{C1} and ε_{C2} are the same quantities referred to the KaoS target in cave C. The pions have been transported neglecting decay and interactions along the beam-line. The nominal momentum, P_0, is 1 GeV/c.

even higher in the HADES beam-line. This means that, in addition to the distance, the acceptance of the beam-line plays a major role in the final muon content. If the acceptance of the beam-line is small in comparison with the breadth of momentum distribution of the resulting muons, only a small fraction of these will be accepted. The momentum limits, $P_{\mu-}$ and $P_{\mu+}$ of the muon momentum distribution can be calculated from kinematical considerations,

$$P_{\mu\pm} = \frac{1}{2}(\frac{M_\mu^2}{M_\pi^2} + 1)P_\pi \pm \frac{1}{2}(1 - \frac{M_\mu^2}{M_\pi^2})E_\pi = 0.79P_\pi \pm 0.21E_\pi, \qquad (4.11)$$

where M_μ and M_π are the muon and pion rest mass and E_π and P_π are the energy and momentum of the original pion. The use of ± has been used to put both limits in one expression. From Eq. 4.11 we can conclude that the muon momentum range is clearly greater than the window acceptances of the beam-lines, which are approximately 8 % and 1 % for HADES and C beam-lines, respectively. Thus, it is possible to have less muon content in the C beam-line. A similar reasoning is also valid for the momentum dependence of the muon to pion ratio. In principle, we expect that this magnitude decreases with increasing momentum because of the lower decay in flight rate. However, the angular deviation of the resulting muon from the direction of the original pion is smaller at higher momenta and, therefore, the acceptance for these high momentum muons is larger. It is the combination of both aspects, decay in flight probability and acceptance of the resulting muon, which is responsible of the final muon to pion ratio shown by simulations.

Multiple scattering

The effect of multiple scattering can be estimated by comparing the acceptances calculated with multiple scattering switched on and off, respectively. The models of gaussian and Molière multiple scattering are included in GEANT through the routines GMGAUS and GMULTS, respectively. To quantify the multiple scattering in the beam-line we calculate the fraction of pions entering the beam-line which arrive to the cave target. As all the other interactions are switched off, they can only be removed from the beam-line by multiple scattering in the detectors. Let us first remind that these detectors are the three hodoscopes H_1, H_2 and H_3 for the HADES beam-line, and the hexagonal scintillators H_2 and H_3 for the C beam-line. That is, we have simulated the beam-lines with the same detectors that were used in the experiments described in chapter 3. The description of these detectors and their positions in the beam-line have been given in chapter 2. In Fig. 4.8 the results obtained

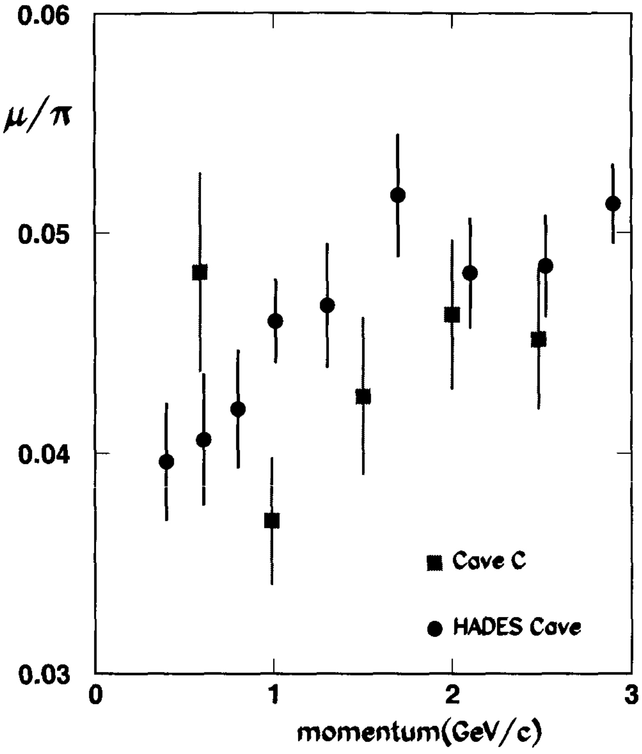

Figure 4.7: Simulated muon to pion ratio at the targets of HADES and C caves as a function of the central momentum of the beam-line.

with the gaussian and Molière models are plotted. Both models give similar results. The pions have been generated according to a Maxwell-Boltzmann distribution with T=80 MeV, in the momentum range $\Delta P/P_0 = 8\%$ and in the angular range $\Delta\Omega = 2.5$ mrad. The conclusion of these simulations is that multiple scattering is very important at low momenta. However, for the HADES beam-line it is negligible above 2 GeV/c.

We have also investigated the pion beam attenuation by multiple scattering obtained for three different combinations of the detectors of the C beam-line. In this case only the Molière model has been used. The results are plotted in Fig. 4.9. In this plot the attenuation factor due to multiple scattering when

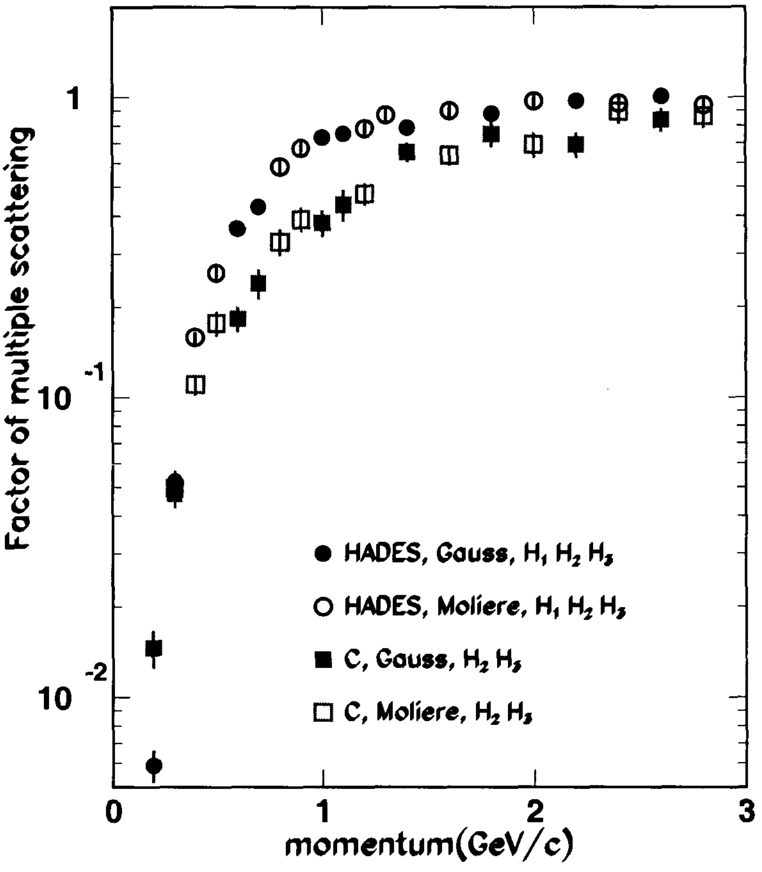

Figure 4.8: Reduction factor of the pion beam intensity produced by multiple scattering in the beam-line detectors as a function of the central momentum for HADES and C beam-lines and for the gaussian and the Molière models.

both detectors, H_2 and H_3[1] are placed along the beam-line is compared with

---

[1] The simulations in the C beam-line were done considering that the only elements in the beam-line were the plastic scintillators. However, both detectors, H_2 and H_3, were fixed in a stainless steel box ($2 \times 0.1mm$), which should also have been considered. We have tried to take this additional contribution into consideration by means of the following calculations. The length divided by the radiation length is approximately the same for 0.2 mm of steel as for 5 mm of plastic scintillator. Therefore, the multiple scattering effect produced by

the attenuation produced when only one of the two is present. We have also compared these attenuation factors to the experimental values presented in section 3.2.3. As expected, the attenuation is higher when we have both H_2 and H_3 detectors. When we only have H_2 or H_3, the attenuation is higher for the detector placed farther from the KaoS target. The experimental data and the simulated values are in good agreement and the shapes of the curves are quite similar, which supports multiple scattering in the beam-line detectors as the main cause of the pion beam attenuation observed, at least for low momenta.

Hadronic interaction

Finally, we consider hadronic interactions. This can be taken into account by any of the three available packages in GEANT: FLUKA, GCALOR and GHEISHA. We have obtained comparable results with the three packages. The attenuation of the pion beam at the HADES target due to hadronic interactions in the hodoscopes is found to be between 3 and 4% for momenta above 1 GeV/c. Between 0.5 and 1.0 GeV/c the attenuation factor remains below 5%, and for lower momenta (up to 0.3 GeV/c) it rises up to 8%.

4.3 Simultaneous simulation of production target and beam-line transport

In this section we present simulations of the whole system: the production target and the transport of secondary particles along the beam-line. The simulated intensities of pions and electrons in the cave targets are compared to our experimental data.

4.3.1 Simulations for the HADES beam-line

In first place, we simulate the production target by a source of Maxwell-Boltzmann distributed pions, as explained in section 4.1.1. The generated

---

scintillator and steel box should also be similar. Moreover, the attenuation factor produced by H_2 and H_3 is approximately the product of the factors due to H_2 alone and H_3 alone. This fact has been observed both, for experimental data and for the simulated values. Thus, we assume that the total attenuation (box + scintillator) is the square of the attenuation produced by the scintillator alone. Thus, in Fig. 4.8 and Fig. 4.9 and for the C beam-line the square of the attenuation factor for the scintillators is represented.

New simulations with the right geometry are on the way, but the results should not differ significantly from those presented here.

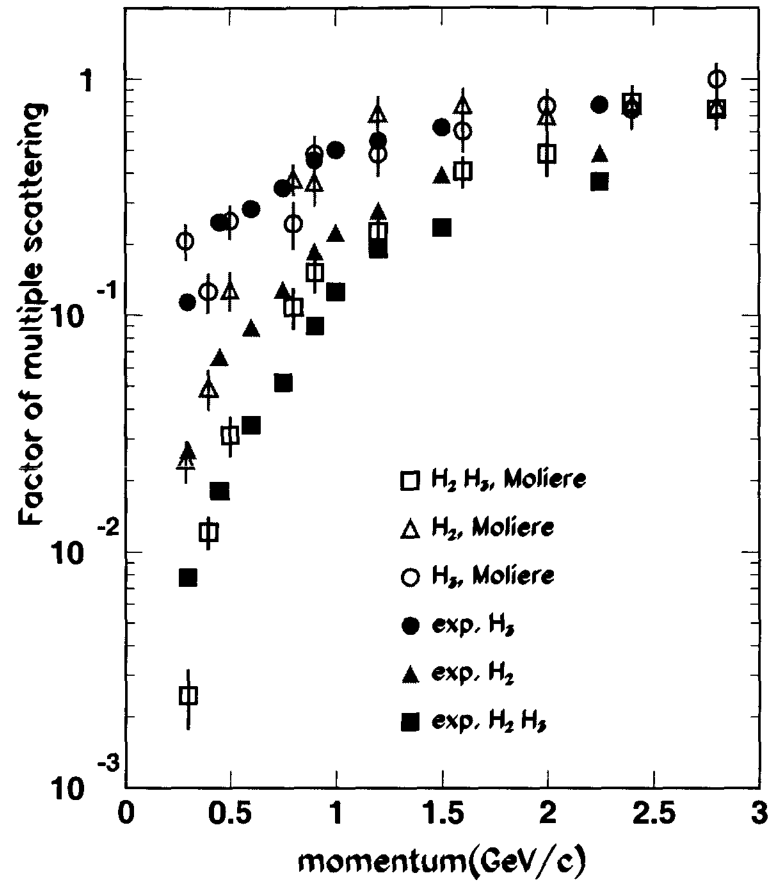

Figure 4.9: Attenuation factor of pion beam intensity due to multiple scattering as a function of the central momentum and different combinations of detectors along the C beam-line. The Molière theory for multiple scattering has been used. The filled symbols represent the measured pion beam attenuation, as explained in section 3.2.3.

pions are transported along the production target and the beam-line. During the transport, pions can be rejected either because their kinematical variables get out of the acceptance window of the beam-line or because they are absorbed by an interaction, i. e., hadronic interaction, multiple scattering or decay in flight. In Fig. 4.10 the simulated number of negative pions crossing the HADES target within a circle of 4 cm radius, generated by two different M-B distributions of temperatures T=80 MeV and T=100 MeV, respectively, are shown as a function of the central momentum. Simulations with and without attenuation of the primary beam in the production target are presented. All the simulated pion intensities are lower than the experimental data except for the case in which T=100 MeV and no attenuation of the primary beam in the production target is considered. In this case the data are fairly well reproduced except at energies around the maximum where the simulated intensity is still somewhat low. A quite good reproduction of the data in the whole momentum range is obtained when we introduce the energy dependent asymmetry parameter $a(E)$ given by Eq. 4.6 instead of using an average a. The fact that the simulations without attenuation of the primary beam are those which reproduce the best the experimental pion intensities could be considered as an indication that pion production in second chance collisions cannot be disregarded.

In second place, we consider the model in which the carbon projectile is considered as a hot hadron gas of nucleons as explained in section 4.1.2. The number of negative pions per spill arriving to HADES target within a circle of 4 cm radius as a function of the central momentum for a 2 AGeV ^{12}C primary beam is plotted in Fig. 4.11. The hadronic interactions have been calculated by both the FLUKA and GCALOR packages and the experimental data are also shown for comparison. We can observe that the simulated pion intensities are lower than the experimental values, especially with GCALOR. Only around 1.5 GeV/c there is a good agreement between the experimental data and the simulations. In the remaining energy range the simulations underpredict the experimental data. This fact is not surprising because, as it can be observed in Fig. 4.2, this model underpredicts the experimental pion production cross section except around 1.5 GeV/c.

Finally, simulations of positive and negative pion intensities for a proton primary beam are plotted in Fig. 4.12. It can be observed in this figure that low momentum pions are underestimated for both polarities by both FLUKA and GCALOR. However, the simulations are close to the experimental data around 1.5 GeV/c. At high momenta the two hadronic packages give very different results. A decrease of the number of pions is predicted by GCALOR, as observed in the experimental data, whereas FLUKA gives over 2 GeV/c an additional increase of pions. The reason of this increase is not clear but it seems to be related with the second peak observed in Fig. 4.3. Moreover, we can say that, in general trends, there is a correspondence between Fig. 4.12 and Fig. 4.3.

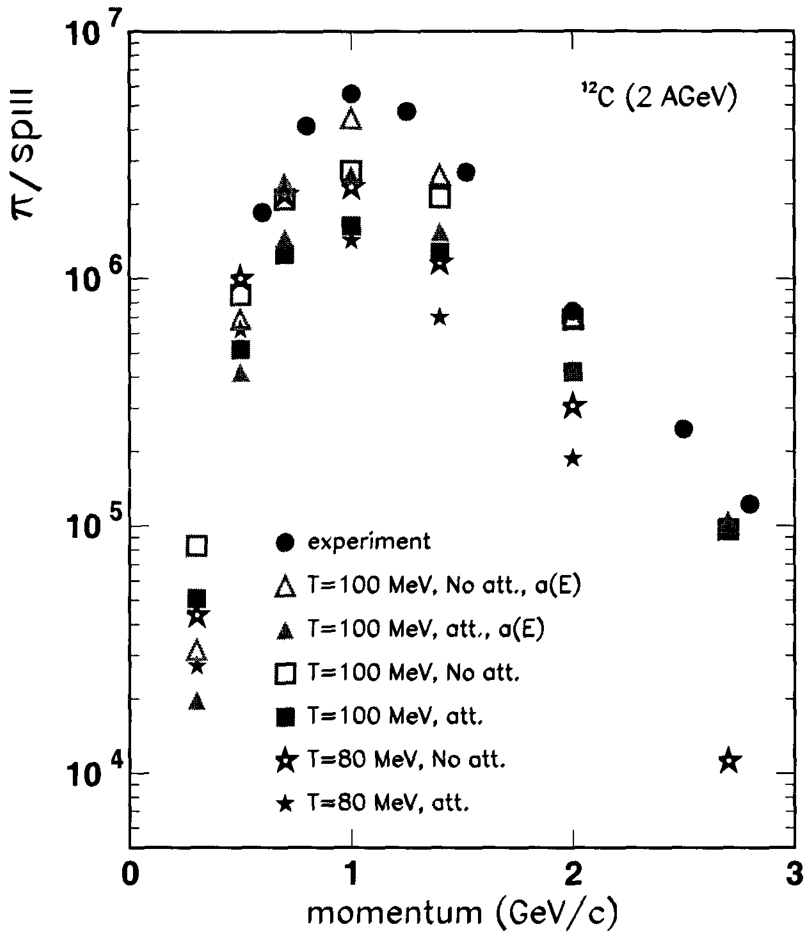

Figure 4.10: Number of simulated π^- per spill at the HADES target as a function of the central momentum for a 2 AGeV ^{12}C primary beam generating pions according to Maxwell-Boltzmann distributions with temperatures T=80 and T=100 MeV. For each temperature, there are two simulated values corresponding to the two different $\pi^-/^{12}C$ multiplicities given by Eq. 4.4 and Eq. 4.5. For T=100 MeV, simulations with an energy dependent asymmetry $a(E)$ are also shown. Our measured data are plotted for comparison.

4.3.2 Simulations for the C beam-line

The simulations for the C beam-line have been carried out in the same way as for the HADES beam-line.

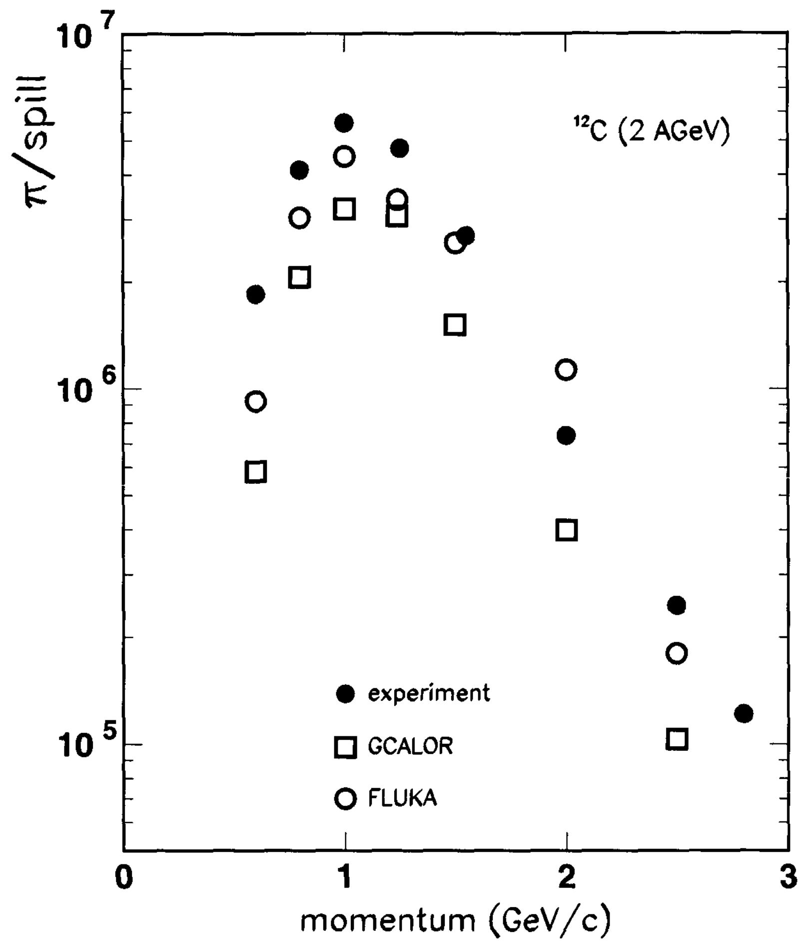

Figure 4.11: Number of π^- per spill in the HADES target as a function of the central momentum of the beam-line obtained from simulations of the whole system. Results for hadronic interactions simulated by FLUKA and GCALOR are presented for a 2 AGeV ^{12}C primary beam considered as a hot hadron gas of nucleons. Experimental data are plotted for comparison.

Pion intensities obtained from simulating a carbon projectile impinging on a beryllium target of 10 cm length are plotted in Fig. 4.13. We present on one hand simulations obtained by considering the ^{12}C as a hot Fermi gas and

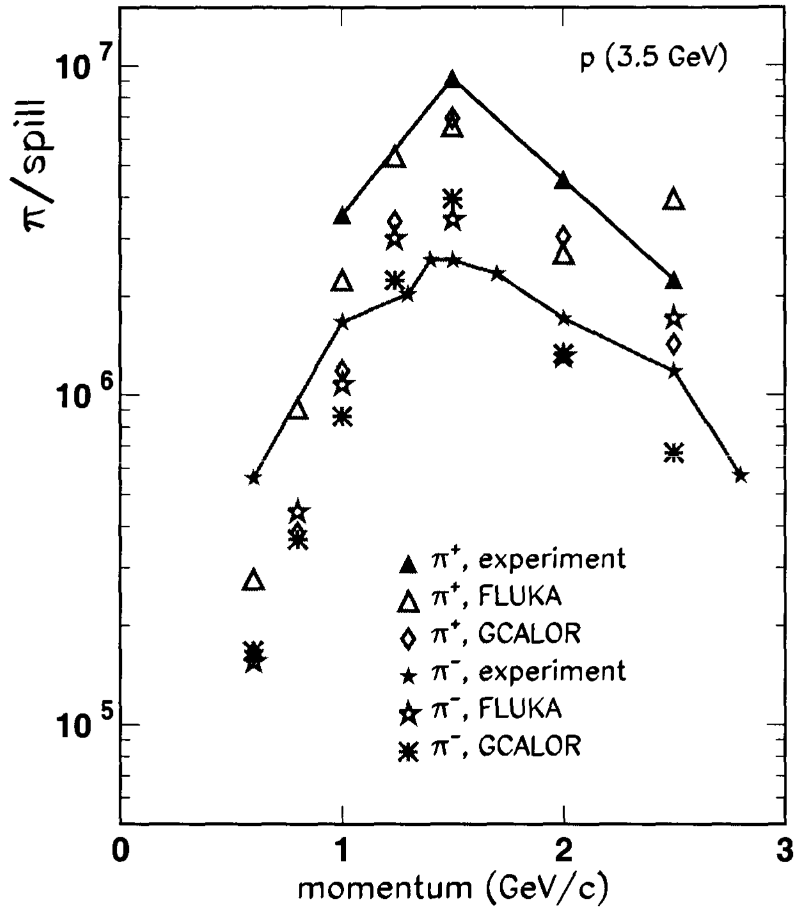

Figure 4.12: Number of π per spill in the HADES target as a function of the nominal momentum obtained from simulations of the whole system for 3.5 GeV proton primary beams. Results for hadronic interactions simulated with FLUKA and GCALOR are presented. Experimental data are plotted for comparison. The lines through the experimental points are only to guide the eye.

accounting hadronic interactions with the FLUKA and GCALOR packages, as explained in section 4.1.2, and on the other hand a simulation in which the production target has been simulated by a Maxwell-Boltzmann distribution of

T=100 MeV and no primary beam attenuation, as explained in section 4.1.1. We have plotted the number of pions per spill hitting to the KaoS target within a radius of 4 cm as a function of the momentum. The available experimental data are also shown for comparison. We can observe that the simulations have roughly the same shape as the experimental data but overestimate slightly them at high momenta.

The simulated π^- and π^+ intensities for a 4.7 GeV proton primary beam and for both hadronic packages are plotted in Fig. 4.14 and compared to the experimental data. Like in Fig. 4.13, the shape of the intensities as a function of the momentum is rather well reproduced, which is not trivial considering the complexity of the simulations. However, we obtain here a pronounced overestimation of the experimental pion intensities at high momenta.

There are marked differences between the simulations of the HADES and C beam-lines. While in the former the experimental data are underpredicted, in the latter simulations reproduce the shape of pion intensities but overpredict the experimental data at high momenta. The reason for this overestimation is not clear although a plausible explanation could be that the simulated and the real acceptances are different because an element of the beam-line has not been properly simulated. Comparing the figures of this section with those of section 4.1, we can conclude that the most probable reason for these differences is that the acceptance of the C beam-line is slightly overestimated by the simulations.

Electron production and transport along the C beam-line

Simulated electron production intensities versus momentum are compared to our data in Fig. 4.15 for a 2 AGeV ^{12}C primary beam and in Fig. 4.16 for a 4.7 GeV proton primary beam. The points representing the simulations correspond to the arithmetic mean of the number of electrons and positrons crossing the KaoS target within a circle of 4 cm radius. It can be observed that in the carbon case the simulations are below the experimental values, especially at low momenta. This was not expected because the simulations did not underestimate the pion data and electrons are produced mainly in pair conversion of γ rays originating from π^0 decays. The reason of this apparent contradiction is not clear although a possible explanation is that our model for carbon primary beams give a low number of high energy pions, which are supposed to be the source of electrons in the secondary beam. A second possible explanation could be that in the case of a carbon primary beam there exist an additional source of electrons not included in our simulations which produces the missing electrons. However, to our knowledge, all the disregarded

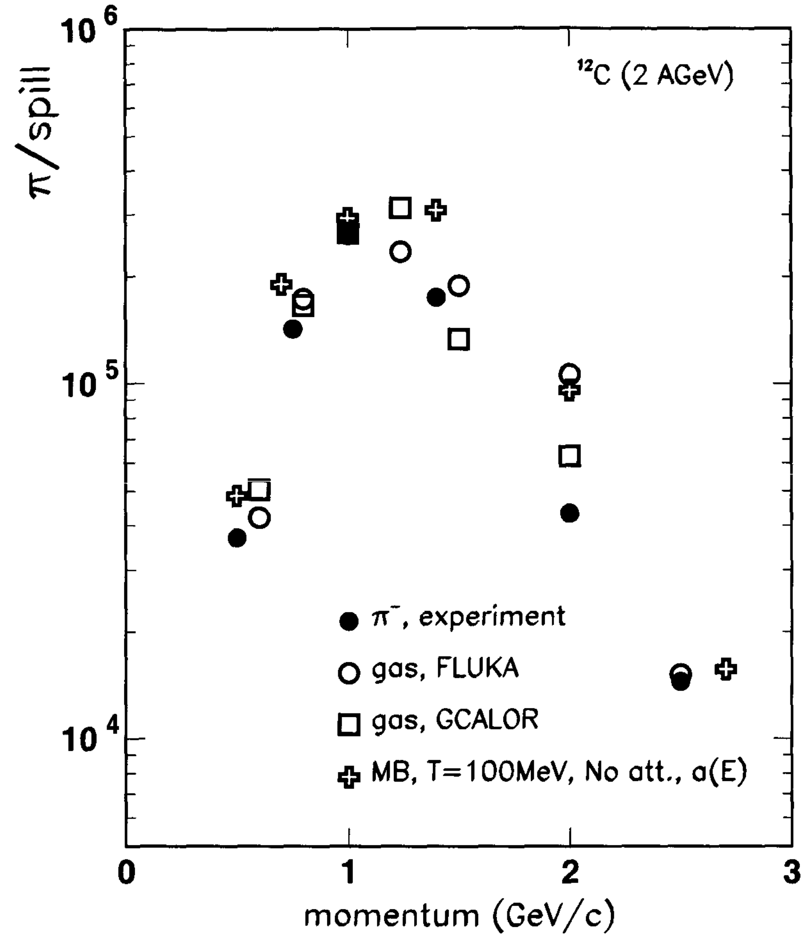

Figure 4.13: Number of π per spill in the KaoS target as a function of the central momentum of the beam-line, obtained from simulations of the whole system for a 2 AGeV ^{12}C primary beam. Results for the hadron gas model of the primary beam and hadronic interactions simulated by both FLUKA and GCALOR are presented. The pion intensities obtained by transporting M-B distributed pions of T=100 MeV and pion multiplicity given by Eq. 4.5 are also plotted. The experimental data are plotted for comparison.

channels seem to be negligible.

For the proton primary beam, we obtained that FLUKA simulations have

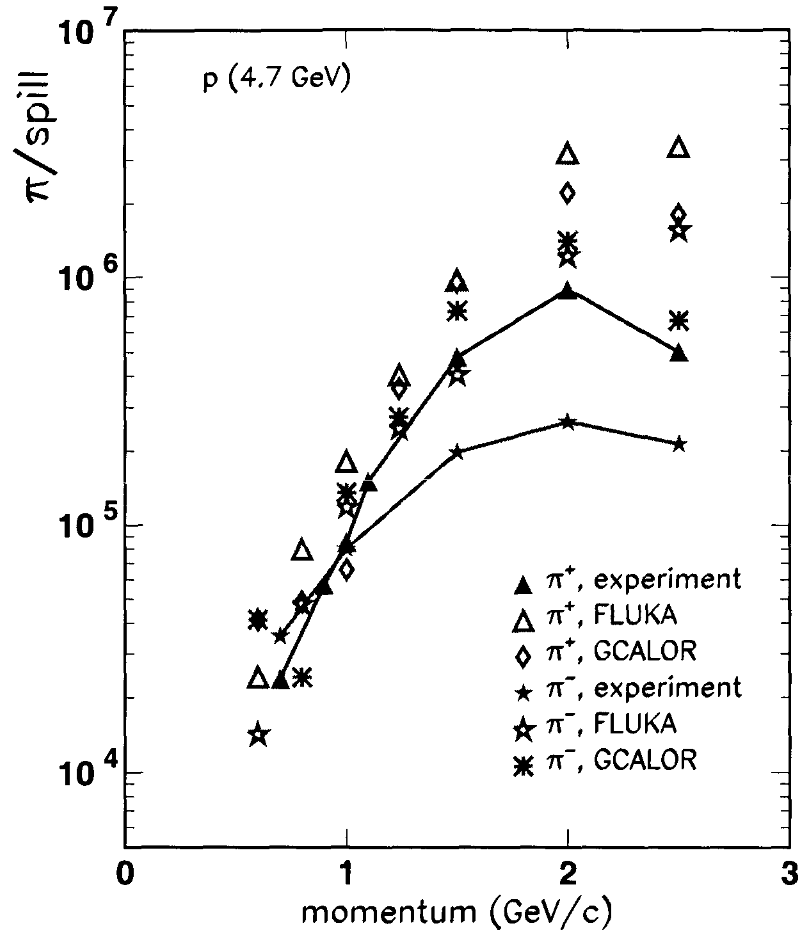

Figure 4.14: Number of positive and negative pions per spill at the KaoS target as a function of the momentum obtained from simulations of the whole system for a 4.7 GeV proton primary beam. Results for hadronic interactions simulated with both FLUKA and GCALOR are presented. The experimental data are also plotted for comparison. Lines are drawn to guide the eye.

the same pattern as the experimental data but overestimate them by a factor somewhat larger than two. The origin of this discrepancy seems to be the fact that FLUKA overestimates the pion production cross-section of high energy pions for 4.7 GeV proton induced reactions. On the other hand, GCALOR simulations overestimate the experimental data at low momenta, but are close to them at intermediate and high momenta.

4.3.3 Proton to pion ratio in the cave targets

We have simulated the proton to pion ratio at the cave targets in the case of a proton primary beam. The results obtained for a 4.7 GeV proton primary beam in cave C and for a 3.5 proton primary beam in HADES cave using the FLUKA hadronic package are compared to our data in Fig. 4.17. Simulations are more reliable for particle ratios than for absolute number of particles because errors in the latter produced by neglected effects or model inaccuracies may cancel in the former. We can observe in Fig. 4.17 that a reasonable prediction for the proton to pion ratio is obtained for a 3.5 GeV proton primary beam. However, a similar agreement of the simulations of a 4.7 GeV proton primary beam with the data does not exist. The reason of this discrepancy could be that FLUKA uses different models at 3.5 and 4.7 GeV. Between 2.5 and 4 GeV, a resonance production and decay model is used and for energies higher than 4 GeV a dual parton model is employed. The proton to pion ratio has also been simulated with GCALOR obtaining similar results as with FLUKA.

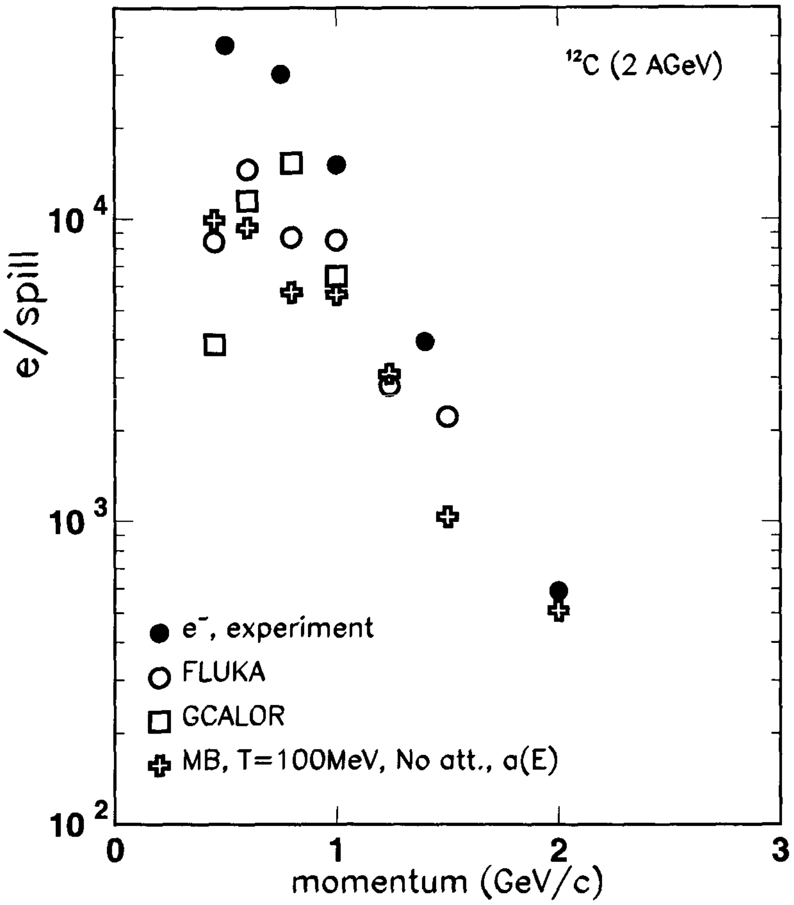

Figure 4.15: Electron intensities at the KaoS target as a function of central momentum for 2 AGeV ^{12}C primary beam. The simulated values are the arithmetic mean of electrons and positrons obtained from simulations of the whole system. Results for hadronic interactions simulated by both FLUKA and GCALOR packages and simulations in which the production target is replaced by a Maxwell-Boltzmann distribution of T=100 MeV are presented. Our experimental values are also shown for comparison.

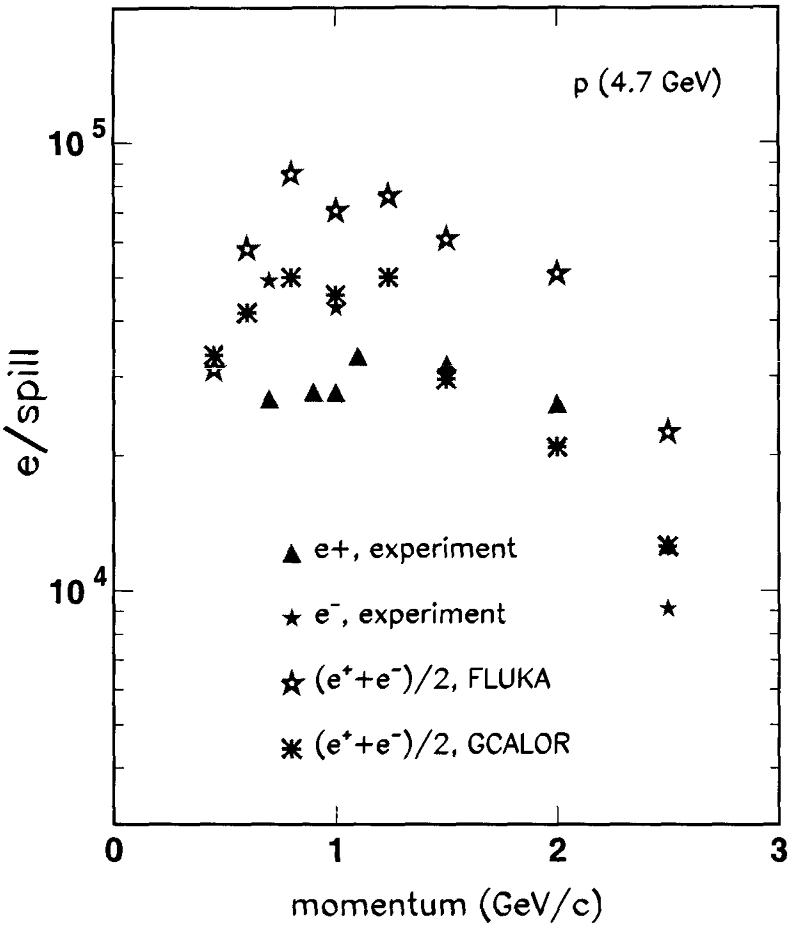

Figure 4.16: Electron intensities at the KaoS target as a function of central momentum for a 4.7 GeV proton primary beam. The simulated values are obtained from simulations of the whole system. Results for hadronic interactions simulated by both FLUKA and GCALOR packages are presented. Our experimental values are also shown for comparison.

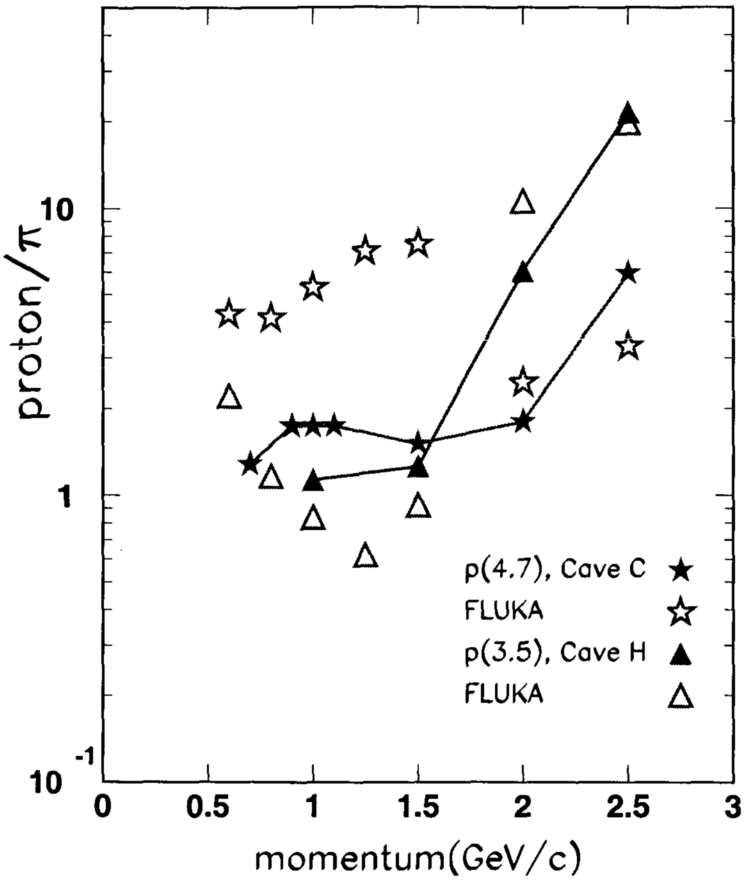

Figure 4.17: Proton to pion ratio as a function of the central momentum of the beam-line. The simulation results with FLUKA for a 3.5 GeV proton primary beam in HADES cave and for a 4.7 GeV proton primary beam in cave C and the corresponding experimental data are shown together. Lines drawn through the experimental data are only to guide the eye.

Chapter 5

Analysis of the data

In this chapter we present quantitative descriptions of the measured intensities of pions and electrons at the cave targets, presented in chapter 3. Our aim is to describe particle intensities by simple models which account for the complex process of particle production and transport by analytical expressions containing only a few phenomenological parameters which can be fitted to the data. If these phenomenological models are able to reproduce the data and the fitted parameters follow systematic trends, this approach can be helpful in determining the optimal conditions for a specific experiment. In addition, the behaviour of fitted parameters can help us to understand the different mechanisms involved in particle production in a thick target and their relative contributions.

5.1 Pion production

5.1.1 Intensity of pions at the beam-line target position

In this section we present a model in which pion intensities at the beam target as a function of central momentum of the beam-line are parameterized in a simple way.

We consider first the production process. In the case of a projectile impinging on a thick target we have to account for both production and absorption of pions. An important aspect which complicates a simple description of the production process is pion production in secondary collisions. In first chance collisions a large number of secondary particles and nuclear fragments are created which are still able to produce pions in subsequent collisions due to their high energies. The starting point to model the production process is based on the experimental observation that produced pions satisfy a Maxwell-Boltzmann distribution in the nucleon-nucleon center of mass [Sto86], as seen in chapter 1, of the form

$$\frac{d^2\sigma^{\pi}_{cm}}{p^2_{cm}dp_{cm}d\Omega_{cm}} = K\exp\left(-\frac{E_{cm}}{T}\right), \tag{5.1}$$

where the inverse slope parameter T is often identified as a temperature. This distribution has to be boosted to the laboratory system and corrected for the pion beam attenuation produced during the transport along the beam-line in order to describe the measured intensities at the cave target. The attenuation due to decay in flight can be accounted for by a factor $exp(-lm/(\tau P_0))$, where l is the length of the beam-line, m is the pion rest mass, τ is the pion mean life and P_0 is the central momentum. The attenuation due to multiple scattering has been taken into account by a cubic polynomial $\epsilon_{MS}(p_{lab})$ fitted to the attenuation obtained from the simulations presented in section 4.2.4.

When we bring all the above ingredients together, we obtain for the pion intensities the expression

$$\begin{aligned}\frac{d^2\sigma^{\pi}_{lab}}{dp_{lab}d\Omega_{lab}} &= Kp^2_{lab}\frac{\gamma_{NN}(E_{lab}-\beta_{NN}p_{lab})}{E_{lab}} \times \epsilon_{MS}(p_{lab}) \times \\ &\quad \exp\left(-\frac{l}{\beta_\pi c\gamma_\pi\tau_\pi}\right)\exp\left(-\frac{\gamma_{NN}\left(E_{lab}-\beta_{NN}p_{lab}\right)}{T}\right), \end{aligned}\tag{5.2}$$

where p_{lab} is the pion momentum in the laboratory system, $E_{lab} = \sqrt{p^2_{lab}+m^2_\pi}$, l is the length of the pion trajectory along the beam-line, $\beta_{NN}c$ is the nucleon-nucleon center of mass velocity, $\gamma_{NN} = 1/\sqrt{(1-\beta^2_{NN})}$, $\beta_\pi c$ is the pion velocity, $\gamma_\pi = 1/\sqrt{(1-\beta^2_\pi)}$, τ_π is the pion life-time at rest and $\epsilon_{MS}(p_{lab})$ is the multiple scattering attenuation.

We have neglected the dependence on momentum of pion absorption because this dependence is not too important at the relevant energies here [Clo74]. An effect that could be important is the asymmetry on the azymutal angle of pion production, as discussed in section 1.1.2. A way to take the asymmetry into account is to introduce a multiplicative factor $\epsilon_a(E)$ in Eq. 5.2 obtained from boosting $\epsilon_a(E) \approx 1 + a(E)$ to the laboratory system with $a(E)$ given by Eq. 4.6. Here, we would like to remark that $a(E)$ is not well determined from available experiments and, therefore, has large uncertainties. However, our purpose here is only to estimate the influence of the asymmetry on the pion intensities. Thus, the comparison of the model to the measured data can be helpful to investigate the importance of asymmetry in the final pion distributions. Therefore, the model of Eq. 5.2 contains only two parameters K and T. In addition we can include the energy dependent asymmetry factor, which has no adjustable parameter. Best fits of the parameters of Eq. 5.2 with and without asymmetry factor to the measured pion intensities in the HADES cave as a function of pion momentum are presented in Fig. 5.1. Similar fits for some of the measured data in cave C are shown in Fig. 5.2. We see that the data are fairly well fitted in both cases, which indicates that the model contains the main ingredients. Fitted parameters to Eq. 5.2 with and without the asymmetry term are given in Tables 5.1 and 5.2, respectively. It can be observed that the asymmetry parameter improves the fit to the data in the central range of momentum, although the data in the peripheral range seem to be better fitted without this parameter. This could indicate that the gaussian shape assumed for the asymmetry parameter is inadequate. In any case, our intention here is only to show the importance of the asymmetry without introducing additional adjustable parameters which could correlate with T and K. It can be observed in Fig. 5.1 and Fig. 5.2 that our model fails to obtain a good fit to the data of positive pions produced by a proton primary beam. The reason is not understood. The introduction of the asymmetry term improves somewhat the fits and perhaps a better parameterization of it could solve, at least in part, the problem.

We have also fitted our model to some measured pion production cross-section in forward direction taken from the literature. The results are shown in Table 5.3. The analysis of these data is easier and more direct than our data because they do not contain the complications associated to secondary interactions in a thick target and beam-line attenuation due to interactions along the beam-line. Although these systems are not measured in the same conditions as our data, it is still possible to make a comparison of the fitted inverse slope parameters. It can be remarked that the inverse slopes presented in Table 5.3 are in fair agreement with those obtained from the fits to cave C intensities but slightly higher than those obtained from the fits to HADES cave intensities. Since this difference cannot have a physical origin, it can only be attributed to uncertainties and systematic errors in the measured pion intensities and in the multiple scattering attenuation.

5.1.2 Pion intensity versus production target thickness

In the previous section we have studied the pion distribution only as a function of momentum. In this section we consider its dependence on the production

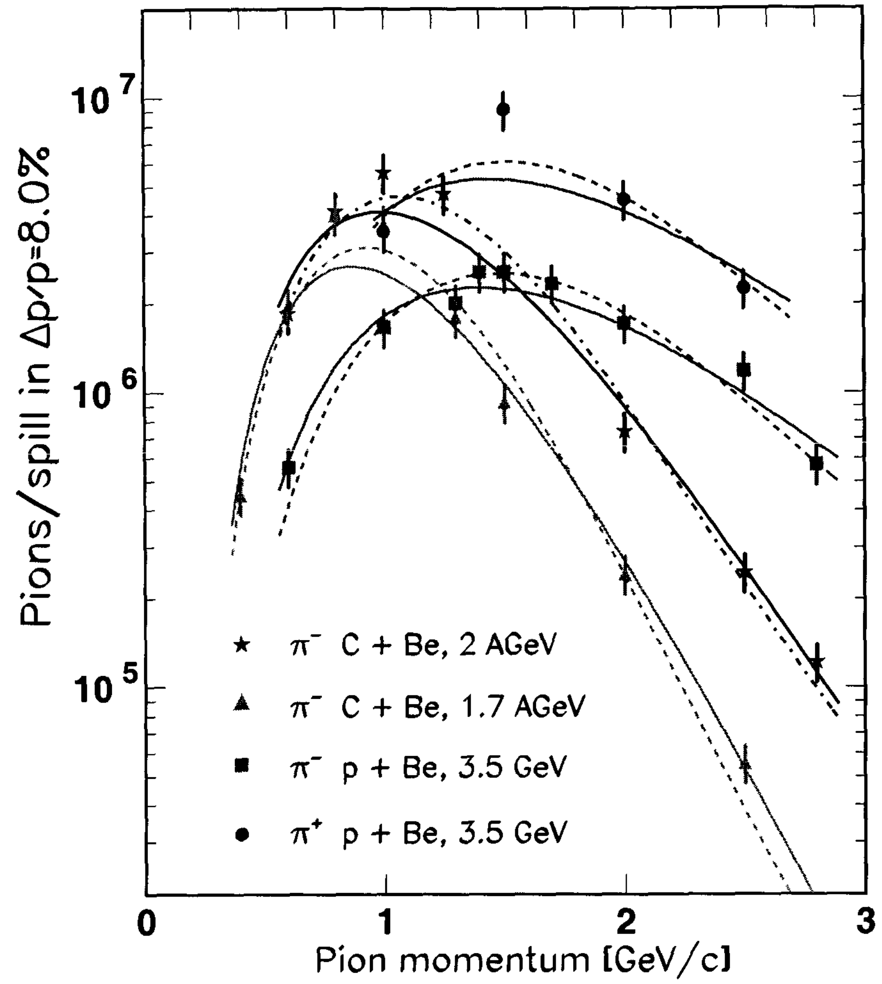

Figure 5.1: Pion intensity in the HADES cave target for p and ^{12}C primary beams at different energies as a function of the pion momentum of the beam-line. The solid and the dashed curves are fits of Eq. 5.2 to the data with and without asymmetry factor, respectively, as explained in the text. The fitted parameters are given in Tables 5.1 and 5.2.

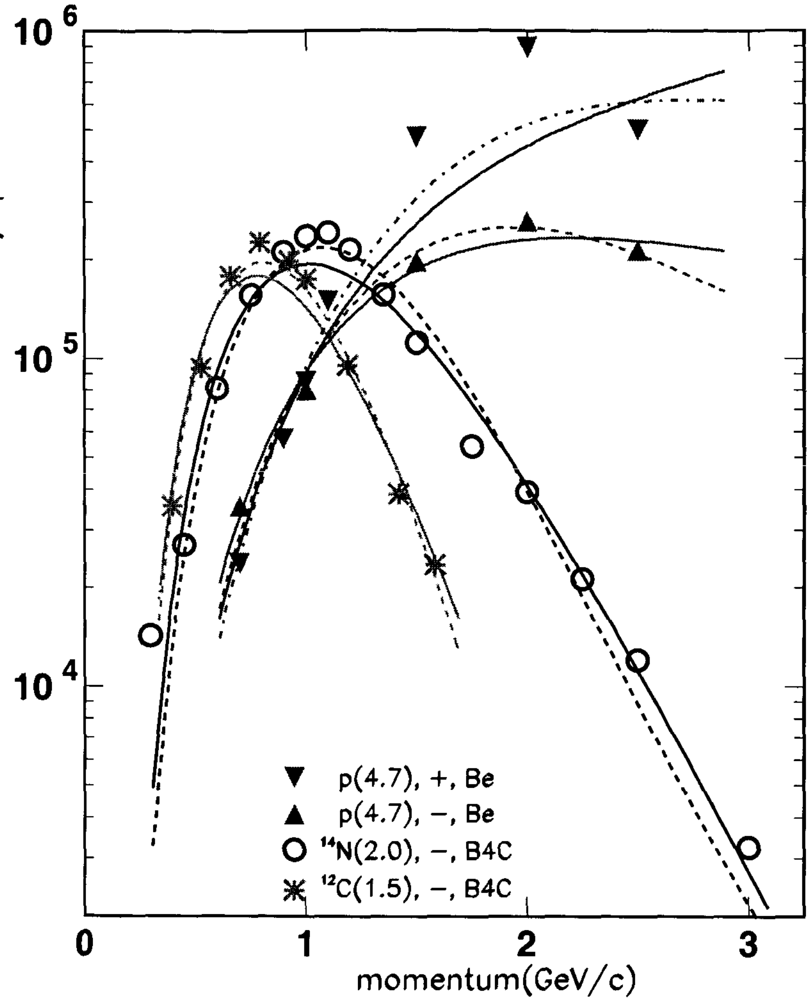

Figure 5.2: Pion intensity transported to cave C for different primary beams, polarity of the beam-line and target as a function of the central momentum of the beam-line. The solid and the dashed curves are fits of Eq. 5.2 to the data with and without asymmetry factor, respectively, as explained in the text. The fitted parameters are given in Tables 5.1 and 5.2, respectively.

target thickness. The C-cave data are the most useful for this purpose because of the large number of targets measured, listed in Table 2.1. It is convenient

Proj.	E_0 (AGeV)	Cave, Target, Polarity	K ($\times 10^7$)	T (MeV)	χ^2/ν	ν
^{12}C	2.0	H, Be, -	106 ± 13	113 ± 2	2.0	6
	1.7	H, Be, -	130 ± 17	100 ± 2	2.4	6
p	3.5	H, Be, -	12.9 ± 1.8	155 ± 6	0.8	7
	3.5	H, Be, +	27 ± 7	161 ± 11	5.0	2
^{14}N	2.0	C, Be, -	22 ± 3	101 ± 3	2.3	10
	2.0	C, B_4C, -	16 ± 2	104 ± 3	2.7	13
^{12}C	2.0	C, Be, -	17 ± 2	106 ± 2	1.8	4
	2.0	C, B_4C, -	21 ± 2	101 ± 2	3.1	3
	1.5	C, B_4C, -	104 ± 14	75 ± 2	1.2	7
	1.5	C, Be, -	84 ± 14	78 ± 2	1.8	2
	1.5	C, Be, +	40 ± 7	81 ± 3	8.0	2
	1.3	C, Be, +	70 ± 17	70 ± 3	5.1	2
p	4.7	C, Be, -	0.67 ± 0.12	215 ± 16	0.7	3
	4.7	C, Be, +	0.32 ± 0.04	440 ± 50	5.4	5

Table 5.1: Parameters obtained by fitting Eq. 5.2 to the pion intensities in the caves as a function of the pion momentum for different primary beams, polarities of the beam-line and production targets (beryllium of 10 cm length and B_4C of 12 cm length). The χ^2 of the fit divided by the number of degrees of freedom ν is also shown.

to consider the dependence of pion production versus the thickness in terms of the variable X defined as

$$X[g/cm^2] = \rho \times (A_p^{1/3} + A_t^{1/3})^2 \times l, \tag{5.3}$$

where l, ρ and A_t are the length, density and mass number of the target, respectively, and A_p is the mass number of the projectile. This variable exploits the known scaling properties of pion production cross sections and allows us to compare on the same plot cross sections corresponding to production targets of different density and to primary beams of different atomic numbers. The pion yield in a thick target depends on several magnitudes although the most important are the primary beam mass and energy and the pion absorption cross section in the production target. The pion absorption cross section has a dependence on pion energy which is important at low energies but can be safely neglected at intermediate energies [Clo74].

The most simple model for the primary beam intensity along the tar-

Proj.	E_0 (AGeV)	Cave, Target, Polarity	K_a ($\times 10^7$)	T_a (MeV)	χ^2/ν
^{12}C	2.0	H, Be, -	25 ± 4	129 ± 3	1.5
	1.7	H, Be, -	38 ± 6	107 ± 3	2.6
p	3.5	H, Be, -	3.0 ± 0.5	184 ± 10	1.0
	3.5	H, Be, +	6.5 ± 1.7	190 ± 16	2.9
^{14}N	2.0	C, Be, -	5.4 ± 1.0	111 ± 4	2.7
	2.0	C, B_4C, -	5.4 ± 0.8	111 ± 3	4.2
^{12}C	2.0	C, Be, -	4.6 ± 0.7	117 ± 3	0.8
	2.0	C, B_4C, -	5.1 ± 0.8	111 ± 4	0.7
	1.5	C, B_4C, -	37 ± 5	76 ± 2	0.5
	1.5	C, Be, -	33 ± 6	77 ± 3	0.5
	1.5	C, Be, +	16 ± 3	80 ± 2	5.3
	1.3	C, Be, +	27 ± 6	69 ± 3	3.8
p	4.7	C, Be, -	0.21 ± 0.04	230 ± 20	0.9
	4.7	C, Be, +	0.105 ± 0.015	540 ± 90	3.5

Table 5.2: Same as Table 5.1, but fitting to Eq. 5.2 multiplied by the asymmetry factor.

Proj.	E_0 (A GeV)	Target, Polarity	T (MeV)	χ^2/ν	T_a (MeV)	χ^2/ν	Ref.
^{12}C	2.1	C , -	99 ± 2	3.4	108 ± 3	5.0	[Moe83]
^4He	2.1	Be, -	99.5 ± 1.3	2.6	110 ± 2	0.5	[Pap75]
	2.1	Be, +	101 ± 4	0.5	110 ± 5	0.2	[Pap75]
p	4.2	Be, -	141 ± 6	0.4	147 ± 8	2.1	[Pap75]
	4.2	Be, +	161 ± 4	3.5	187 ± 6	1.1	[Pap75]

Table 5.3: Fitted parameters and χ^2 divided by the number of degrees of freedom obtained by fitting Eq. 5.2 to the pion production cross section data from the references.

get, $I_P(X)$, which can be assumed is an exponential attenuation of the form $I_P(X) = I_P(0)\exp(-\Sigma_R X)$, where Σ_R is the macroscopic reaction cross-section of the primary beam in the production target normalized to the factor $(A_p^{1/3} + A_t^{1/3})^2$ and to ρ, i. e., $\Sigma_R = \sigma_R \rho N_A/[A_t\rho(A_p^{1/3} + A_t^{1/3})^2]$, where

A_t and ρ are the atomic weight and density of the production target, σ_R is the reaction cross section of the primary beam on the production target, and N_A is the Avogadro's number. The cross-section can be estimated by $\sigma_R = \pi[r_0(A_p^{1/3} + A_t^{1/3})]^2$, where $r_0 = 1.2$ fm. Thus, the factor containing the mass numbers cancels and we have $\Sigma_R = \pi r_0^2 N_A/A_t$, which should compare to the fitted Σ_R values.

The pion intensity I_π is determined from the balance of pion production by the primary beam intensity I_P and pion absorption in the production target. Therefore

$$\frac{dI_\pi}{dX} = \Sigma_p I_P(X) - \Sigma_a I_\pi(X), \tag{5.4}$$

which has the solution

$$I_\pi(X) = I_0(\exp(-\Sigma_R X) - \exp(-\Sigma_a X)), \tag{5.5}$$

where Σ_R and Σ_a are the macroscopic cross sections for primary beam projectile on the production target and for pion absorption, respectively. Notice that Σ_p, the macroscopic cross section for pion production in first chance collisions, does not appear explicitly in the solution but it is included in the integration constant I_0. This equation accounts neither for energy loss of the primary beam nor for pion production by secondary fragment and pion scattering in the production target and should therefore be considered only as a crude approximation. The pion absorption cross-section is quite well known from experimental data [Clo74, Gac85] and we have used this information to fit our model to Eq. 5.5 with Σ_R and I_0 as free parameters. One of the main assumptions of this model is that pions are produced only in first chance interactions. It is clear that secondary particles will also produce pions. In fact, most of the secondary particles that have been produced in the first interaction have still enough energy to produce pions, specially nuclear fragments from the projectile. The neglect of this pion source produces an underestimation on the measured pion production rate. The error made can be estimated by calculating an upper limit of the pion intensity derived from the assumption that the primary beam is not attenuated at all, i. e., $I_P = I_P(0)$. In this case the solution for the pion intensity is

$$I_\pi(X) = I_0(1 - \exp(-\Sigma_a X)). \tag{5.6}$$

The last equation leads certainly to an overestimation of pion production. In order to have a realistic model, we multiply Eq. 5.6 by a phenomenological factor $exp(-\Sigma_{ef} X)$ where Σ_{ef} is an effective macroscopic cross section which takes into account the attenuation of pion production rather than that of the primary beam. Thus, we have

$$I_\pi(X) = I_0 \exp(-\Sigma_{ef} X)(1 - \exp(-\Sigma_a X)). \tag{5.7}$$

Although this expression is still a sum of two exponentials, the signification of Σ_a here and in Eq. 5.5 are considerably different. We can check both models by fitting the experimental pion intensities in cave C target to both Eq. 5.5 and Eq. 5.7. Fig. 5.3 shows the fitted curves (solid lines for Eq. 5.5 and dashed ones for Eq. 5.7) for carbon primary beams at different energies, momenta and polarities of the beam-line. In general, the fitted curves follow closely the experimental data, specially for the model of Eq. 5.5. However, the data present a broader shape and a flatter maximum, placed at lower X values, than the fits. Although Eq. 5.5 follows better the data than Eq. 5.7, both results deserve to be presented because of the different interpretation of the fitted parameters. Σ_R represents the macroscopic reaction cross section between projectile and target, and thus, if the fitted value differs strongly from $\pi r_0^2 N_A/A_t$, it could mean that pion production by secondary particles and nuclear fragments produced in primary beam collisions is important. For the second model, Σ_{ef} should be zero in the case of constant production along the target, that is, production by nuclear fragments and protons compensates the primary beam attenuation. As this is unrealistic, a positive value of Σ_{ef} is expected, which is a measure of the effective attenuation of the pion production rate along the production target. Therefore, both models are helpful for understanding pion production by a nucleus impinging on a thick target. The fitted parameters for the data in the C beam-line and the models of Eq. 5.5 and Eq. 5.7 are given in Tables 5.4 and 5.5, respectively. The value for $\Sigma_R = \pi r_0^2 N_A/A_t$ is 3.0, 1.10 and 0.6 $\times 10^{-3}$ cm^2/g for the Be, B_4C and Ti targets, respectively. We observe that the fitted parameters are close to the beryllium Σ_R for 2 AGeV primary beams. However, for 1.5 and 1.3 AGeV primary beam energies there is a strong deviation from the Be value, which could indicate that secondary collisions play an important role in these cases. The lower Σ_R is, the lesser the primary beam attenuation and the larger the production target thickness needed to reach the maximum pion intensity. We have also studied the dependence of the fitted Σ_R on momentum, primary beam energy and polarity. In Fig. 5.4, the momentum and primary beam energy dependence of the fitted Σ_R is plotted. We can observe that there is a slight increase of Σ_R with momentum, which is more pronounced for a nitrogen than for a carbon primary beam. A measure of this increase is given by the fitted slope, m. In the case of nitrogen primary beam m = $(0.7 \pm 0.3) \times 10^{-3}$ cm ^{2} c/[g GeV], whereas

$m = (0.3 \pm 0.3) \times 10^{-3}$ cm ^{2} c/[g GeV] for a carbon primary beam. The dependence of Σ_R on primary beam energy is stronger than the dependence on momentum. We have obtained a slope $m' = (4.6 \pm 1.1) \times 10^{-3}$ cm^2/[g AGeV] by fitting Σ_R versus the primary beam energy. The lack of data with positive polarity makes it very difficult to determine if there is any dependence of Σ_R on polarity. We have observed that the pion intensities of both polarities are different in the case of a carbon primary beam at 1.5 AGeV, but we cannot extract any conclusion due to poor statistics.

Proj.	E_0 (AGeV)	p_0 (GeV/c)	I_0 ($10^4\pi$/spill)	Σ_R ($10^{-3}cm^2/g$)	χ^2/ν	ν
^{14}N	2.0	-0.6	20 ± 2	2.8 ± 0.3	0.6	7
		-0.9	49 ± 5	2.9 ± 0.3	0.8	7
		-1.5	22.6 ± 1.9	3.7 ± 0.4	1.2	7
		-2.25	4.5 ± 0.5	3.7 ± 0.5	2.8	7
^{12}C	2.0	-1.0	61 ± 6	2.6 ± 0.3	0.4	7
		-1.4	43 ± 5	2.9 ± 0.3	0.5	7
		-2.0	9.6 ± 0.9	3.0 ± 0.4	1.2	7
		-2.5	3.3 ± 0.3	3.1 ± 0.3	0.9	7
	1.5	-1.0	27 ± 2	5.9 ± 0.7	3.2	7
		+1.0	26 ± 2	4.5 ± 0.5	1.2	7
	1.3	+1.0	7.9 ± 0.6	6.0 ± 0.7	0.3	6

Table 5.4: Parameters obtained from fitting pion production intensities in cave C versus the production target thickness to Eq. 5.5.

The dependence of Σ_{ef} on momentum and primary beam is less pronounced than that of Σ_R. Only in the case of a 1.3 A GeV ^{12}C primary beam Σ_{ef} has a significant increase. We expected for this parameter a value close to 0 in the case of no attenuation of the primary beam and close to Σ_R for attenuation of the primary beam and no pion production in secondary collisions. The fitted value falls between these two limits, which indicates that neither pion production by secondary particles nor carbon primary attenuation in the target can be disregarded.

Finally, we would like to mention that we did also a target study in the HADES beam-line [Día02], but in that case only four different beryllium targets were employed. The results of this study are plotted in Fig. 3.12. We have fitted the data from these measurements to Eq. 5.5, but fixing Σ_R to the values

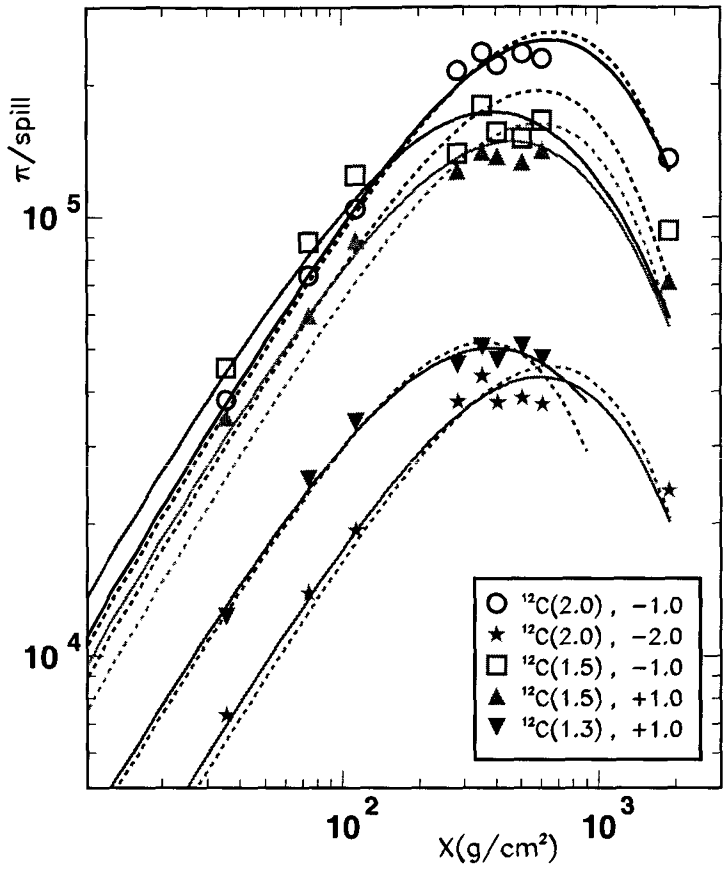

Figure 5.3: Pion intensity in cave C versus $X = \rho \times (A_p^{1/3} + A_t^{1/3})^2 \times l$ using carbon primary beams of different primary beam energy, polarity and momentum. The curves obtained by fitting Eq. 5.5 and Eq. 5.7 are plotted with solid and dashed lines, respectively.

obtained from the C beam-line data. The fits are sufficiently good to conclude that the HADES data are compatible with the results of Σ_R obtained in the C beam-line.

Proj.	E_0 (AGeV)	p_0 (GeV/c)	I_0 ($10^4\pi$/spill)	Σ_{ef} ($10^{-3}cm^2/g$)	χ^2/ν
^{14}N	2.0	-0.6	47 ± 2	1.12 ± 0.07	1.2
		-0.9	118 ± 6	1.13 ± 0.07	1.2
		-1.5	70 ± 4	1.28 ± 0.08	2.8
		-2.25	13.0 ± 0.7	1.18 ± 0.08	4.7
^{12}C	2.0	-1.0	132 ± 6	1.11 ± 0.07	0.7
		-1.4	102 ± 5	1.15 ± 0.07	1.1
		-2.0	23.6 ± 1.1	1.16 ± 0.07	2.0
		-2.5	8.2 ± 0.4	1.18 ± 0.07	1.6
	1.5	-1.0	111 ± 6	1.33 ± 0.09	7.6
		+1.0	94 ± 5	1.34 ± 0.08	3.7
	1.3	+1.0	48 ± 3	2.38 ± 0.19	0.5

Table 5.5: Parameters obtained from fitting pion production intensities in cave C versus the production target thickness to Eq. 5.7.

5.2 Electron production

Electron production by a nucleus impinging on a thick target is more difficult to study than pion production because more processes are involved. However, we have analysed electron intensities by models similar to those presented for pion production.

5.2.1 Intensity of electrons at the target position

In this section we elaborate a model to describe the measured electron intensities at the cave targets as a function of the momentum. As in the pion case, the model includes production in the target and transport along the beam-line. Concerning the transport, we have the same interactions as in the pion case with exception of decay in flight. Concerning the production, we investigated the possible sources of electrons in nuclear reactions with thick targets in section 1.1.6. The electrons coming from e^+e^- conversion of γ-rays produced in π^0 decay via $\pi^0 \rightarrow \gamma\gamma$ seems to be the most important channel. Therefore, there is a direct relation between electron and pion production and, thus, the final electron distribution has to be correlated to the pion distribution.

As in the pion case and for the same reasons we suppose that the electron

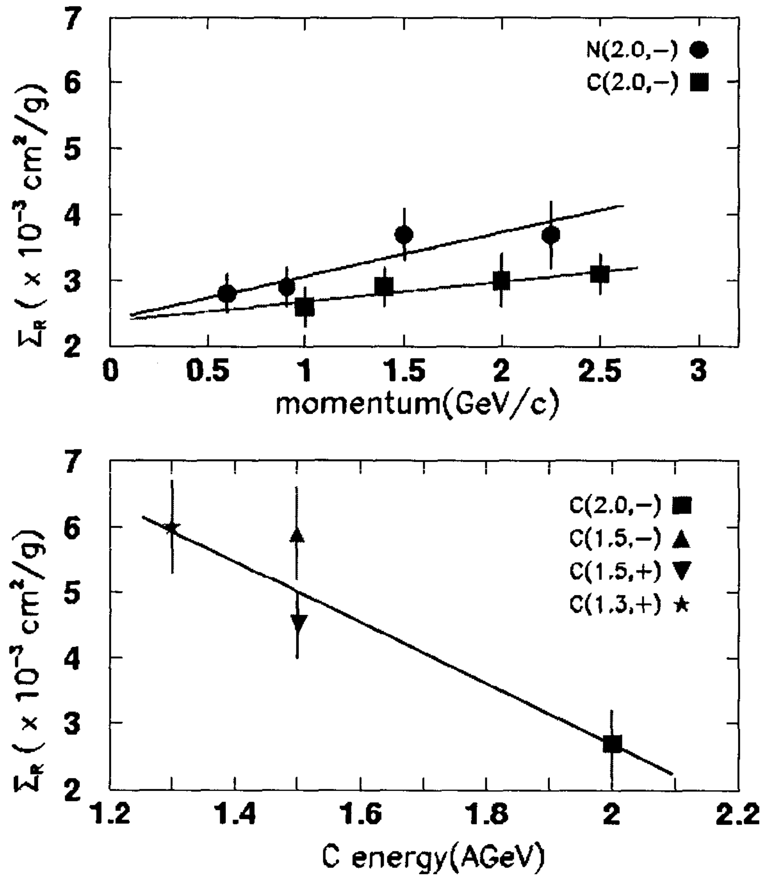

Figure 5.4: Σ_R values obtained from the fits of Eq. 5.5. In the upper figure, Σ_R is plotted as a function of momentum for 2 AGeV ^{14}N and 2 AGeV ^{12}C primary beams. In the lower figure, fitted Σ_R values as a function of the ^{12}C primary beam energy for central momentum selected to 1 GeV/c are shown. The straight lines in both figures are least square fits.

source has a Maxwell-Boltzmann distribution in the nucleon-nucleon center of mass frame. Boosting this distribution to the laboratory system and accounting for multiple scattering attenuation along the beam-line through a multiplicative factor ϵ_{MS} we obtain the following expression,

$$\begin{aligned}\frac{d^3\sigma^e_{lab}}{dp_{lab}d\Omega_{lab}} &= Kp^2_{lab}\frac{\gamma_{NN}(E_{lab}-\beta_{NN}p_{lab})}{E_{lab}} \times \epsilon_{MS}(p_{lab}) \times \\ & \exp\left(-\frac{\gamma_{NN}\left(E_{lab}-\beta_{NN}p_{lab}\right)}{T}\right), \end{aligned} \tag{5.8}$$

where E_{lab} and p_{lab} are the electron energy and momentum.

In the electron case, we expect lower temperatures than in the pion case because final electrons have lower energy than the pions from which they originate. In fact, the maximum energy that a final electron could have is roughly half the energy of the parent pion. For the electron case we have not considered any asymmetry because the intermediate steps involved in electron production should smooth any angle dependence. In Fig. 5.5 some of our data in cave C and the best fits of Eq. 5.8 to them are plotted. Again, we observe that this simple model fits the data quite well except at the lowest energies. Low energy electrons are not explained by Eq. 5.8 because the model does not contain electromagnetic cascades in the thick target which are responsible of most of the electron yield in the low momentum region. In Table 5.6, the parameters obtained by fitting Eq. 5.8 to our data are shown. The T parameters are smaller than in the pion case. The ratio $T_e/T_\pi \approx 0.6 - 0.75$ decreases slightly with primary beam energy.

To have a better understanding of the electron production process we have fitted Eq. 5.8 to the simulated electron data presented in Fig. 4.15, which are originated only from π^0 generated in the production target following a Maxwell-Boltzmann distribution with a temperature of 100 MeV. Fitting Eq. 5.8 to the intensity of electrons arriving to the cave target we obtain a temperature of 82 ± 4 MeV, i. e., $T_e/T_\pi = 0.82 \pm 0.4$. This ratio is close to the ratio of temperatures fitted to our experimental data, in particular in the case of the data obtained with a 2 AGeV primary beam. As a conclusion, the comparison of fits to experimental data and to simulations supports the assumption that electrons are mainly produced by pair conversion of gamma rays originated in π^0 decay.

5.2.2 Electron intensity versus production target thickness

Electron production as a function of the target thickness is more difficult to study than pion production ought to the more complex mechanisms involved. We assume that electrons are mainly produced in the decay of neutral pions through pair conversion of γ rays as stated in the previous section. Therefore, any model for electron production has to include information about the neutral

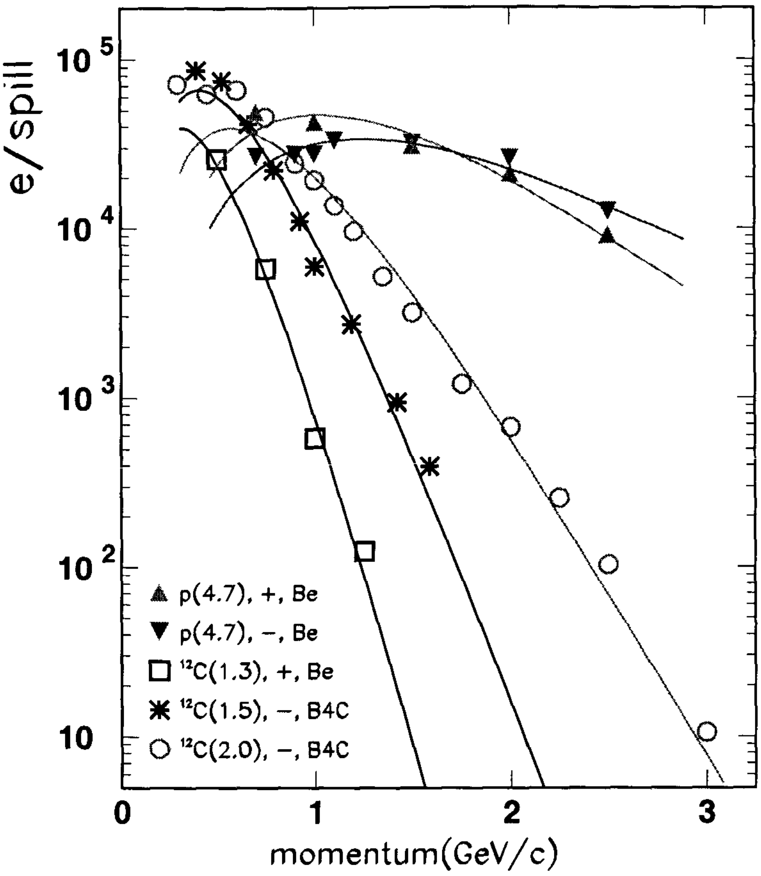

Figure 5.5: Electron intensity in cave C for different primary beams, polarities of the beam-line and targets as a function of the central momentum of the beam-line. The lines are fits of Eq. 5.8 to the data. The fitted parameters are given in Table 5.6.

pion yield. In addition, it is also necessary to calculate the pair conversion rate of the electromagnetic cascade of gamma rays originated in π^0 decay and the acceptance of the beam-line for these pairs.

To obtain an equation for the electron intensities as a function of the target thickness we first consider their variation in a small region of the production target taking into account the relevant processes. The variation of intensity of

Proj.	E_0 (AGeV)	Target, Polarity	K ($\times 10^7$)	T (MeV)	χ^2/ν
^{14}N	2.0	Be, -	1.1 ± 0.4	78 ± 3	2.6
	2.0	B_4C, -	2.2 ± 0.4	75.4 ± 1.6	3.0
^{12}C	2.0	Be, -	1.5 ± 0.4	78 ± 2	1.3
	2.0	B_4C, -	3.1 ± 0.8	74 ± 3	0.5
	1.5	B_4C, -	12 ± 3	55.4 ± 1.6	1.7
	1.5	Be, -	18 ± 6	49 ± 2	5.5
	1.5	Be, +	15 ± 5	49 ± 2	3.4
	1.3	Be, +	21 ± 8	42.4 ± 1.6	2.4
p	4.7	Be, -	0.51 ± 0.14	107 ± 7	0.8
	4.7	Be, +	0.20 ± 0.04	134 ± 8	0.4

Table 5.6: Parameters obtained by fitting Eq. 5.8 to the electron intensities in cave C versus pion momentum for different conditions of primary beam, polarity of the beam-line and target (10 cm long beryllium or 12 cm long B_4C). The χ^2 divided by the number of degrees of freedom is also shown to indicate the goodness of the fit. The ν values are those given in table 5.1.

electrons of a certain energy E_e in a small region of length dl at the position l inside of the production target, $dI_e(E_e,l)/dl$, is given by

$$\frac{dI_e(E_e,l)}{dl} = \Sigma_{pair} I_\gamma(2E_e,l) - \Sigma_{br} I_e(E_e,l) + \int_{E_e}^{\infty} \Sigma_{br}(E'_e \to E_e) I_e(E'_e,l) dE'_e, \tag{5.9}$$

where $I_\gamma(2E_e,l)$ represents the intensity of photons of energy $2E_e$ at the position l and Σ_{pair} and Σ_{br} are the macroscopic cross section for electron-positron pair creation and for electron bremsstrahlung, respectively. The first term accounts for electrons originated in pair conversion of photons with energy twice the electron energy. The second term is due to the loss of electrons of energy E_e by bremsstrahlung in the target. In this case, the electron does not disappear but its energy changes. The last term accounts for electrons of higher energies that due to a bremsstrahlung interaction have a final energy E_e. To solve the previous equation, we need to know $I_\gamma(E_\gamma,l)$ also. A similar reasoning gives for the γ intensities the equation

$$\frac{dI_\gamma(E_\gamma, l)}{dl} = \Sigma_{P\to\gamma} I_P(l) - \Sigma_{pair} I_\gamma(E_\gamma, l) + \int_{E_\gamma}^{\infty} \Sigma_{br}(E'_e \to E'_e - E_\gamma) I_e(E'_e, l) dE'_e, \tag{5.10}$$

where $I_P(l)$ is the primary beam intensity at l and $\Sigma_{P\to\gamma}$ is the macroscopic cross-section for γ production in projectile-target interactions. The first term on the right hand is a direct contribution from the projectile-target collision (although multistep process because there are intermediate steps like π^0 production). The second term accounts for pair conversion of photons and the third term accounts for the production of gamma rays by electron bremsstrahlung. To solve Eq. 5.10, the primary beam distribution in the target $I_P(l)$ is needed. Here, as in the pion case, we have assumed a distribution $I_P(l) = I_P(0)\exp(-\Sigma_P l)$. The simoultaneous solution of Eq. 5.9 and Eq. 5.10 gives the electron intensities as a function of the target thickness. However Eq. 5.9 and Eq. 5.10 are an involved system of integro-differential equations. In order to simplify the calculations and be able to solve the system we leave out the integral terms. These terms are supposed to be smaller than the leading terms because they are due to second order effects. Moreover, these terms produce mostly final electrons at low energy, so they contribute mainly to the low energy electron region, which is not our subject here. In any case, only the agreement of the solution with the data would justify a posteriori the neglect of the integral terms.

The electromagnetic processes play a dominant role in electron production and in order to be able to make a comparison between the different targets, it is convenient to normalize the thickness of the production target to the radiation length. With this aim, we define a dimensionless variable $L = l_{tar}/L_{rad}$, where l_{tar} is the length of the target and L_{rad} is the radiation length of the production target considered. Moreover, the relations $\Sigma_{br} = 1/L_{rad}$ and $\Sigma_{pair} = \frac{7}{9}L_{rad}$ [Leo94] make the variable L still more useful.

If the integral term is neglected in Eq. 5.10, it can be solved as in the pion case,

$$I_\gamma(E_\gamma, L) = K^\gamma(E_\gamma)\left(\exp(-[\Sigma_P L_{rad}]L) - \exp\left(-\frac{7}{9}L\right)\right), \tag{5.11}$$

in terms of the new variable L. K^γ is an integration constant. Introducing Eq. 5.11 in Eq. 5.9 without the integral term, we obtain for I_e the following expression,

$$I_e(E_e, L) = K^e \Big[\exp\Big(- [\Sigma_P L_{rad}] L \Big) + \kappa \exp(-\frac{7}{9}L) - (1+\kappa)\exp(-L) \Big], \qquad (5.12)$$

with

$$\kappa = -\frac{7}{2}\Big(1 - (\Sigma_P L_{rad})\Big) \qquad (5.13)$$

where K^e is an integration constant which has to account for the acceptance of the beam-line. The macroscopic reaction cross section Σ_P is given by

$$\Sigma_P = \sigma_R \rho N_A / A_t = \pi r_0^2 (A_p^{1/3} + A_t^{1/3})^2 \rho N_A / A_t \qquad (5.14)$$

where we have used the geometric prescription for the microscopic cross section σ_R. We have used Eq. 5.12 to fit our data considering K^e and r_0 as free parameters. We have found that the fits obtained are not quite satisfactory which can be attributed to the neglect of the integral terms and to other effects left out like secondary interactions. In order to get a better fit to the data we introduce a phenomenological factor $\exp(-\phi L)$ to account for the neglected terms, where ϕ is a free parameter. Thus, the final model to which electron intensities as a function of the target thickness have been fitted is

$$I_e(L) = K^e \exp(-\phi L) \Big[\exp\Big(- (\Sigma_P L_{rad}) L \Big) + \kappa \exp(-\frac{7}{9}L) - (1+\kappa)\exp(-L) \Big]. \qquad (5.15)$$

The fitted parameters obtained for different projectiles, primary beam energies, momenta and polarities of the beam-line are given in Table 5.7. The χ^2/ν value is also shown. In Fig. 5.6 the fitted curves are compared to the experimental data for a 2 AGeV nitrogen primary beam. In spite of the complexity of the problem and of the different effects involved, the data are quite well reproduced with this simplified model. The values of the fitted parameters seem to be reasonable. We expected a value of about 1.2 fm for r_0 following the geometric prescription. Our values are of the same order but clearly below. The reasons for this discrepancy is not well understood. One plausible explanation could be that our model does not include pion production by secondary nuclear fragments. As most of these nuclear fragments have enough energy to produce pions, the effective beam is not attenuated by Σ_P, the macroscopic cross section between projectile and target, but by a lower value which leads to a lower value of r_0. A second explanation of the deviation of the fitted r_0 from the expected value could be the existence of a correlation between this parameter and ϕ. We have obtained for ϕ values very close to 1 for 2 AGeV primary beams. This could indicate that this phenomenological factor is related to electromagnetic effects because it scales fairly well with L_{rad}. This interpretation is plausible if we realize that the phenomenological factor has been introduced in order to account for the deficiencies of the model and that the main shortcoming of it is, probably, the neglect of the integral terms in Eq. 5.9 and Eq. 5.10, which are related to electromagnetic effects.

Proj.	E_0 (AGeV)	p_0 (GeV/c)	K^e (10^3 e/spill)	r_0 (fm)	ϕ	χ^2/ν
^{14}N	2.0	-0.6	870 ± 100	0.74 ± 0.03	0.87 ± 0.06	2.6
		-0.9	330 ± 30	0.74 ± 0.02	0.90 ± 0.06	3.1
		-1.5	42 ± 4	0.69 ± 0.03	0.99 ± 0.06	3.7
		-2.25	3.1 ± 0.4	0.51 ± 0.08	0.94 ± 0.06	2.1
^{12}C	2.0	-1.0	290 ± 30	0.756 ± 0.018	0.88 ± 0.06	3.4
	1.5	-1.0	59 ± 10	0.43 ± 0.11	0.76 ± 0.07	1.2
		+1.0	58 ± 7	0.73 ± 0.03	1.14 ± 0.07	5.9
	1.3	+1.0	59 ± 10	0.861 ± 0.006	3.8 ± 0.5	5.0

Table 5.7: Parameters obtained from the fit of Eq. 5.15 to the electron intensities in cave C versus the production target thickness for ^{14}N and ^{12}C primary beams. Third column gives the polariy and central momentum of the beam-line. The ν values are given in Table 5.4.

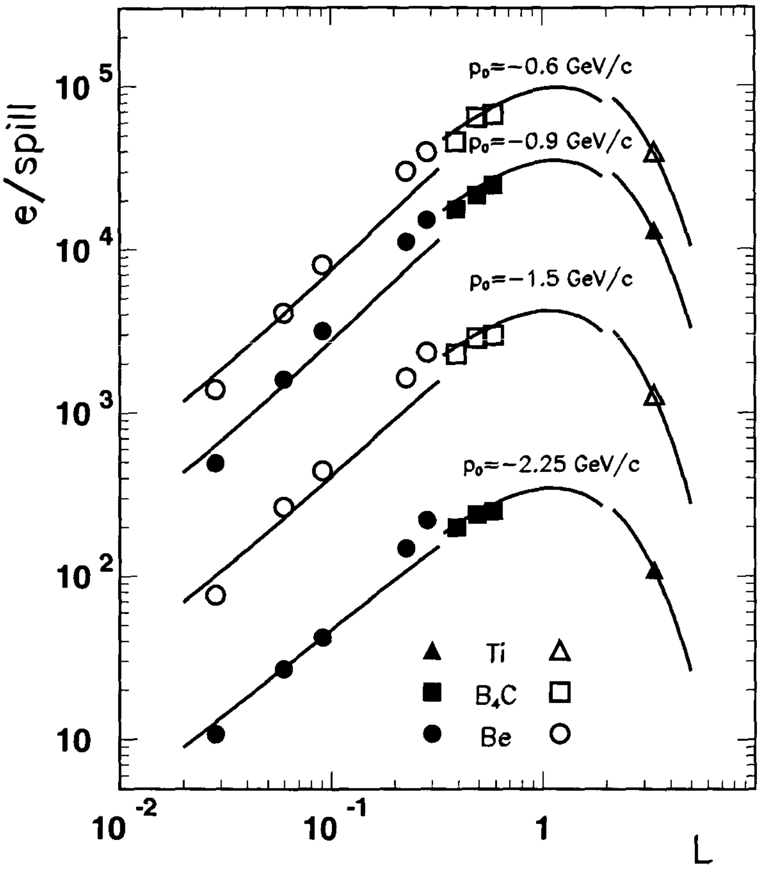

Figure 5.6: Fits of Eq. 5.15 to the electron intensities in cave C versus the target thickness normalized to the radiation length for a 2 AGeV nitrogen primary beam and different central momenta. The discontinuities of the fitted functions are due to the change of the chemical composition of the target, i. e., from beryllium to carbon boride and from this to titanium.

Conclusions

In this work we have described the recently installed secondary pion beam at SIS/GSI. The aim of this facility is to complement the physics program at GSI by means of providing a new beam of particles, specially pions, with momenta up to 3 GeV/c. In order to have the best quality secondary beam, a huge work has been developed by the collaboration: design, construction, simulations, tests, calibrations and commissionings of the pion beam-lines and their related detectors. This thesis compiles part of this task, from the study of the previous knowledge on the reactions which are important for our secondary beam, to the investigations of our production targets, beam-lines and detectors. The purpose of all this job was to understand the secondary beam as well as possible in order to optimize it.

The final conclusion is a better knowledge of the secondary beam that is nowadays available at GSI. We have investigated the main properties of this facility, sometimes these properties have been experimentally measured, other times they have been known with the help of simulations, but mostly by combining both aspects. We have presented the intensities and particle ratios at the caves depending on the momentum, primary beam and target. We have observed that the proton primary beam is the best suited for high energy pions because of the high incident energy; whereas for low momentum pions, and specially π^-, a carbon primary beam is more advisable. The maximum pion intensities that could be reached at HADES cave with the present status is approximately 10^7 π^+/spill at 1.5 GeV/c using proton primary beams and 6×10^6 π^-/spill at 1 GeV/c using carbon primary beams. The intensities at cave C are roughly a factor 10-20 below due to a higher decay in flight and a lower acceptance. In this aspect, our simulations show that the acceptance window is 8% for the HADES beam-line, but only around 1% for the C beam-line. We have also seen that the electron intensities are enough for test and calibrations of detectors. On the other hand, the behaviour of the beam-line detectors and the consequent ability to discriminate the different kind of particles have also been shown. For example, the hodoscopes provide a time of flight resolution better than 120 ps and will serve us to discriminate pions from heavier particles. At the same time, these detectors give us a momentum resolution better than 0.5%, as it was required. Besides, the electron discrimination is possible with the help of a Cherenkov detector. Another aspect that we have also seen is the effect of the beam-line detectors in terms of intensity losses.

All these parameters are very important because they will play a role in the future proposed experiments using this beam and will indicate their feasibility. Furthermore, we were not satisfied having only the value of the parameters of the secondary beam and we have looked for models which help to understand all the relevant processes involved. To be concrete, we have studied the production in proton or light nucleus impinging on thick targets and the transport of the produced particles along the beam-line. The knowledge of these aspects has allowed us to think and to work in subsequent optimizations.

After all this job, we consider that the important aspects related to this secondary beam are well understood. Consequently we have reached a big portion of the objective with the investigation of the different properties of the beam-line: the particle intensities at the HADES and C cave targets as a function of the primary beam and momentum; the target studies; the acceptance of the beam-lines and the behaviour of the beam-line detectors and their effects on the beam.

However, there is still work to be done by the pion collaboration. For instance, design and construction of monitor detectors with a smaller effect on the intensities and a higher rate capability will be needed. In this sense, fiber scintillators arrays are being considered. Another possible improvement is to increase the yield of the electron secondary beam by optimizing the target for proton primary beams. As we have proposed, this target should be made of two blocks. In first place, a long rod of a light material like beryllium, and in second place, a short rod of approximately one radiation length of a heavier material like tungsten.

Bibliography

[Aar87] T. Aarnio et al., Fluka user's guide, TIS-RP-190 CERN, 1987.

[Ago02] S.Agostinelli et.al., Preprint **CERN-IT-20020003**, **KEK 2002-85**, **SLAC-PUB-9350**, submitted to Nucl. Instrum. and Meth. A, 2002.

[Álv98] M. Álvarez, Tesina de Licenciatura, Universitat de València, 1998.

[And01] A. Andronic et al., IEEE Trans. Nucl. Sci. **48** (2001) 1259.

[Ard99] M. Ardid, N. Yahlali, J. Díaz, M. Álvarez, in *Experimental Nuclear Physics in Europe*, B. Rubio, M. Lozano, W. Gelletly Editors. American Institute of Physics, New York, 1999.
R.S. Simon, Prog. Part. Nucl. Phys. **42** (1999) 247.
N. Yahlali, M. Ardid, J. Díaz, M. Álvarez, Czech. J. Phys. **50/S2** (2000) 140.

[Ave97] R. Averbeck et al., Z. Phys. **A359** (1997) 65.

[Bao91] Bao-An Li et al., Phys. Rev. **C 44** (1991) 250.

[Bar97] R. Barth et al., MBS, GSI Multi-Branch System User Manual, GSI Report, 1997.

[Bla92] T. Blaich et al., Nucl. Instrum. and Meth. **A 314** (1992) 136.

[Bra84] P. Braun-Munzinger et al. Phys. Rev. Lett. **52** (1984) 255.

[Bro84] R. Brockmann et al., Phys. Rev. Lett. **53** (1984) 2012.

[Brü75] W. Brückner et al., Phys. Lett. **B 55** (1975) 107.

[Bru94] R. Brun et al., CERN Program Library Long Writeup **W5013** (1994).

[Cas90] W. Cassing et al., Phys. Rep. **188** (1990) 363.

[Clo74] A.S. Clough et al., Nucl. Phys. **B 76** (1974) 15.

[Cug81] J. Cugnon et al., Nucl. Phys. **A 352** (1981) 505.

[Día02] J. Díaz et al., Nucl. Instrum. and Meth. **A 472** (2002) 511.

[Dov80] C.B. Dover, L. Ludeking and G. E. Walker, Phys. Rev. **C 22** (1980) 2073.

[Dub00] S. Dubnicka, A.Z. Dubnickova and P. Weisenpacher, Preprint **hep-ph/0001240**, 2000.

[Fer94] P. Fernández de Córdoba, E. Oset and M.J. Vicente-Vacas, Nucl. Phys. **A 592** (1995) 472.

[Fes85] H. Fesefeldt, Simulation of hadronic showers, physics and applications, Technical Report PITHA 85-02, 1985.

[Foe98] A.Foerster, diploma thesis, TU Darmstadt, 1998.

[Gac85] V.V. Gachurin et al., Preprint **ITEP-85-59**, 1985.

[Gaz95] M. Gazdzicki and D. Röhrich, Z. Phys. **C 65** (1995) 215.

[Ger99] J. Gerl et al., GSI Proposal: High-Resolution Hypernuclear γ-Spectroscopy at GSI, 1999.

[Gob93] A. Gobbi et al., Nucl. Instrum. and Meth. **A 324** (1993) 156.

[Gro00] D.E. Groom et al., Review of Particle Physics, Eur. Phys. J. **C 15** (2000) 1.
P.V.R. Murthy, C.A. Ayre, H.R. Gustafson, L.W. Jones, M.J. Longo, Nucl. Phys. **B 92** (1975) 269.

[Gud92] K.K. Gudima et al., Phys. Lett. **B 287** (1992) 302.

[Had00] Hadronic Physics with HADES,
http://www-hades.gsi.de/proceedings/hadrons/index.html.

[Had01] X HADES Collaboration Meeting,
http://www-hades.gsi.de/proceedings/collmeetX.

[Har85] J.W. Harris et al., Phys.Lett. **B 153** (1985) 377.

[Har87] J.W. Harris et al., Phys.Rev.Lett. **58** (1987) 463.

[Har99] O.N. Hartmann, diploma thesis, University of Giessen, 1999.

[Hub94] S. Huber, J. Aichelin, Nucl. Phys. **A 573** (1994) 587.

[Kim96] Y.D. Kim et al., Nucl. Instrum. and Meth. **A 372** (1996) 431.

[Kli90] S. Klimt et al., Phys. Lett. **B 249** (1990) 386.

[Lan85] G. Landsberg, Phys. Rep. **128** (1985) 301.

[Lau00] F. Laue et al., Eur. Phys. J. **A 9** (2000) 397.

[Leo94] W.R. Leo, Techniques for Nuclear and Particle Physics Experiments, Springer-Verlag, 1994.

[Lom97] B. Lommel, Annual Progress Report of "A Pion Beam Facility for Experiments at SIS" project, Annex 5: Status report on the pion production target, GSI Darmstadt, 1997.

[Mar98] A. Marin et al., Nucl. Instrum. and Meth. **A 417** (1998) 137.
A. Marin et al., Phys. Lett. **B 409** (1997) 77.

[Mar99] G. Martínez et al., Phys. Rev. Lett. **83** (1999) 1538.

[Mar91] J.A. Maruhn, International Review of Nuclear Physics, Vol. 5, World Scientific (1991).

[Met93] V. Metag, Prog. Part. Nucl. Phys. **30** (1993) 75.

[Met95] V. Metag, GSI Internal Report: A Pion-Beam Facility for Experiments at SIS, 1995.

[Met99] V. Metag, Prog. Part. Nucl. Phys. **42** (1999) 75.

[Met00] V. Metag, Remarks on the composition of the secondary beam, Presented topic at the "Hadronic Physics with HADES meeting", http://www-hades.gsi.de/proceedings/hadrons/vm/vm.html, 2000.

[Min93] CN/ASD Group. *MINUIT-Users Guide*, Program Library **D506**. CERN, 1993.

[Mis91] I.N. Mishustin et al., International Review of Nuclear Physics, Vol. 5, World Scientific, 1991.

[Moe83] E. Moeller et al., Phys. Rev. **C 28** (1983) 1246.

[Mün95] C. Müntz et al., Z. Phys. **A 352** (1995) 175.

[Mün97] C. Müntz et al., Z. Phys. **A 357** (1997) 399.

[Mur02] Y. Murin et al., LUND Preprint, **LUIP 0001** (2002), to be submitted to NIM.

[Nag81] S. Nagamiya et al., Phys. Rev. **C 24** (1981) 971.

[Nov91] R. Novotny et al., IEEE Trans. Nucl. Sci. **38** (1991) 379.

[Pap75] J. Papp et al., Phys. Rev. Lett. **34** (1975) 601.

[Paw95] PAW-Physics Analysis Workstation, R. Brun, O. Couet, C. Vandoni, P. Zanarini, CERN Program Library entry **Q121**, 1995.

[Pel97] D. Pelte et al., Z. Phys. **A 357** (1997) 215.

[Pel97b] D. Pelte et al., Z. Phys. **A 359** (1997) 55.

[Rap00] R. Rapp and J. Wambach, Adv. Nucl. Phys. **25** (2000) 1.

[Rit00] J. Ritman, HADES internal report: measurement of the ω meson transition form factor by measuring the reaction $\pi^+p \to \pi^+p\omega$ with the HADES spectrometer, 2000.

[Sam92] M. Samek, APE-Analysis in PAW Environment, CERN Computer Newsletter **208** (1992) 14.
M. Samek, M. Dahlinger, Version 2.2, GSI Report, 1995.

[Sch96] R. Schicker, et al., Nucl. Ins. Meth. **A380** (1996) 586.

[Sch94] A.Schröter et al., Z.Phys. **A 350** (1994) 101.

[Sch97] Y. Schutz et al. Nucl. Phys. **A 622** (1997) 404.

[Sch94b] O. Schwalb et al., Phys. Lett. **B 321** (1994) 20 and V. Metag, private communication: the pion cross sections from Au+Au at 1 AGeV have been renormalized by 0.6 due to a recent analysis.

[Sen93] P. Senger et al., Nucl. Instrum. and Meth. **A 327** (1993) 393.

[Sen99] P. Senger and H. Strobele, J. Phys. **G 25** (1999) R59 and references therein.

[Sor89] H. Sorge et al., Ann. Phys. **192** (1989) 266.

[Sto86] R. Stock, Phys. Rep. **135** (1986) 259 and references therein.

[Sug98] Y. Sugaya et al., Nucl. Phys. **A 634** (1998) 115.

[Sul82] J.P. Sullivan et al., Phys. Rev. **C 25** (1982) 1499.

[Tam00] H. Tamura et al., Phys. Rev. Lett. **84** (2000) 5963.
T. Hasegawa et al., Phys. Rev. **C 53** (1996) 1210.

[Tan85] I. Tanihata et al., Phys. Rev. Lett. **55** (1985) 2676.

[Tei97] S. Teis et al., Z. Phys. **A 356** (1997) 421.

[Ven94] L.B. Venema, Ph. D. Thesis, Rijksuniversiteit Groningen, 1994.

[Ver82] B. J. VerWest, R. A. Arndt, Phys.Rev. **C 25** (1982) 1979.

[Wag96] A. Wagner, Ph. D. Thesis, TU Darmstadt 1996.

[Wag98] A. Wagner et al., Phys. Lett. **B 420** (1998) 20.

[Wol98] A.R. Wolf, Phys. Rev. Lett. **80** (1998) 5281.

[Yah02] N. Yahlali and J. Díaz, Acta Phys. Polon. **B33** (2002) 909

[Zei94] C. Zeitnitz et al., Nucl. Instrum. Meth. **A349** (1994) 106.